QUANTIFICATION IN DYNAMIC AND SMALL-ANIMAL POSITRON EMISSION TOMOGRAPHY

JA DISSELHORST

QUANTIFICATION IN DYNAMIC AND SMALL-ANIMAL POSITRON EMISSION TOMOGRAPHY

© J.A. Disselhorst, 2011
ISBN: 978-90-365-3270-9
Print: Gildeprint Drukkerijen - The Netherlands

QUANTIFICATION IN DYNAMIC AND SMALL-ANIMAL POSITRON EMISSION TOMOGRAPHY

PROEFSCHRIFT

ter verkrijging van
de graad van doctor aan de Universiteit Twente,
op gezag van de rector magnificus,
prof. dr. H. Brinksma,
volgens besluit van het College voor Promoties
in het openbaar te verdedigen
op woensdag 14 december 2011 om 14:45 uur

door

Johannes Antonius Disselhorst
geboren op 18 mei 1985
te Castricum

Dit proefschrift is goedgekeurd door:
promotoren: prof. dr. ir. C.H. Slump en prof. dr. W.J.G. Oyen
assistent-promotoren: dr. E.P. Visser en dr. L.F. de Geus-Oei

© J.A. Disselhorst, 2011
ISBN: 978-90-365-3270-9

Table of contents

1. Introduction

1.1. Introduction

Positron emission tomography (PET) is a quantitative imaging technique. The technique has a high sensitivity: femtomolar concentrations of a tracer can be detected. Usually, the images are visually inspected and the standardized uptake value (SUV) is used as quantitative measure. The SUV is a method to normalize the activity concentration measured by PET with injected activity and for instance the body weight or surface area of the patient. Sometimes, not only the distribution of the tracer is of interest, but quantification of underlying physiological processes is important. This requires a dynamic PET acquisition followed by pharmacokinetic analysis. Dynamic PET has been used for numerous purposes such as therapy response monitoring [1-3], drug development [4,5] or to study a disease [6-8]. The use of dynamic PET, however, is not straightforward. Many variables affect the final results and need to be considered. Various notable aspects of dynamic PET studies are discussed, divided in four distinct parts: data acquisition, image reconstruction, the input function and pharmacokinetic analysis.

Pharmacokinetic analysis of dynamic PET scans is typically performed using compartment models or graphical analyses. An input function is required in most cases, which describes the activity concentration in the arterial plasma during the scan. It can be obtained through blood sampling or be derived from the PET images. In compartment modeling, the uptake of a radiotracer is described by a number of compartments, each describing a physical location of the tracer (e.g., in the blood plasma or intracellular) and/or a chemical state (e.g., metabolized, bound to a receptor). Rate constants (K_1-k_n) describe transfer between the compartments. To solve these models, and estimate the rate constants in a tissue, nonlinear least squares (NLLS) methods are often employed. Nonlinear regression is sensitive to noise and is computationally intensive. Graphical methods simplify the analysis by linearization. After a certain mathematical transformation, the measured data approaches a straight line. The slope of this line corresponds to a parameter of interest. For dynamic ^{18}F-fluorodeoxyglucose (FDG) PET scans, for instance, the metabolic rate of glucose (MR_{glc}) can be calculated using the slope of the line. More details about these analysis methods, and other alternatives are discussed in section 1.5.

1.2. Data acquisition

Important aspects of a dynamic PET acquisition concern preparation of the scanner (including characterization and quality control), preparation of the patient, administration of the tracer and the PET measurement itself. Many of these aspects are not specific for dynamic PET acquisitions and also apply to static scans. In dynamic acquisitions, however, some points require particular attention. For instance, patient movement during acquisition is detrimental in both types of acquisition, but the generally long acquisition times increase the likelihood of motion in dynamic PET. In the sections below these issues are discussed.

1.2.1. Scanner preparation

PET is in essence a quantitative technique, but to be able to analyze PET scans quantitatively some preparation is required. An important step is normalization of the scanner. Differences in detection efficiency between all the detector pairs (lines of response, LORs) are compensated in the normalization procedure. Also a cross-calibration is required between the scanner and the dose calibrator or well counter. If blood samples are obtained from the patient, the gamma counter or automatic blood sampler should be included in the cross-calibration as well. In addition, all clocks used during the experiment should be synchronized, for proper decay correction.

Full characterization of the PET scanner can be helpful in the design of dynamic PET pro-

tocols. This comprises in the first place the measurement of sensitivity, spatial resolution, scatter fraction and count rate performance. Moreover, image quality aspects are important, such as noise and recovery of small objects. The feasibility of an image-derived input function (IDIF) for instance, can be assessed. For these performance characteristics, guidelines from the industry exist [9,10]. The use of different PET radionuclides with different properties involves characterization for each nuclide individually.

In order to retain accurate PET image quantification, a strict quality control (QC) program should be followed. This includes regular normalization, but also daily uniformity evaluations of the PET and computed tomograph (CT). An overview of recommended QC operations is given by Zanzonico [11] and in the guidelines for PET imaging of the Society of Nuclear Medicine (SNM) [12] and European Association of Nuclear Medicine (EANM) [13].

1.2.2. Patient preparation

An important prerequisite for a good dynamic PET scan is as little interference on homeostasis as possible of unlabeled tracer. For substances that are normally absent from the blood this requires a high specific activity. For others, such as ^{18}F-FDG, this is not sufficient. High blood glucose levels can interfere with the uptake of ^{18}F-FDG, and should be avoided. The distribution of ^{18}F-FDG in the hyperglycemic state differs from the normoglycemic state [14,15]. Guidelines for ^{18}F-FDG PET imaging [12,13] recommend fasting for 4–6 h to prevent hyperglycemia. It is recommended to determine the blood glucose level prior to administration of ^{18}F-FDG, and postpone the scan when glucose levels are too high. This applies to both static and dynamic acquisitions. To estimate the MR_{glc}, the concentration in the blood is required. In general, this is only measured prior to scanning, but the concentration may vary over time, even during the scan [16]. This causes errors in the measured MR_{glc} [17]. Also the so-called lumped constant (LC), describing the difference between uptake rates of glucose and ^{18}F-FDG, should be taken into account when the MR_{glc} is calculated using dynamic ^{18}F-FDG PET scans. Not only can LC vary between subjects [18] and between tissues [18-20], it also varies within organs [21] and can change in pathological situations [22,23]. Therefore it may be more useful to report the metabolic rate of ^{18}F-FDG than the metabolic rate of glucose.

For static acquisitions, patient preparation often includes forced diuresis which is achieved by oral prehydration and administration of diuretics. This improves the quality of the images and reduces radiation exposure. However, in dynamic scans, it may be undesirable as the scan may have to be interrupted due to urinary urgency.

1.2.3. Tracer administration

An essential aspect of a dynamic PET study is the administration of the radiopharmaceutical. In most cases, administration is started simultaneously with the PET acquisition. Still, there are many possible variations: the amount (both in volume as in total activity), the duration and means of the administration can be varied. Radiopharmaceuticals are commonly administered through intravenous infusions, but dynamic studies can be performed using inhaled substances (e.g., [^{15}O]-CO_2) as well. In case of venous infusions, the activity can be administered by hand, or by using an automated pump. In addition, the injection can be followed by a saline flush of variable flow rate and duration. The use of a pump for administration of activity will provide a more consistent and reproducible flow rate, as compared to manual infusion [24]. The flush with saline after injection will clear the canula and other tubing that was used for intravenous injection of the radiotracer. The exact influence of this flush on the quality of dynamic images, or the most optimal procedure has not been studied yet.

To determine the optimal dose, image quality, costs, and radiation exposure to patient and

personnel have to be taken into account. There are recommendations for optimal dosing in static whole-body PET, such as the SNM and EANM guidelines for ^{18}F-FDG PET [12,13]. In many cases, dynamic PET studies are performed with similar activities, although there are no specific guidelines. Dynamic PET acquisitions may benefit from an optimization of the injected activity. There are studies on the effect of the administered dose on dynamic [^{15}O]-H_2O [25,26], but further literature on this subject is limited.

Duration of the infusion affects the dynamic acquisition. In many studies, the tracer is administered as a short bolus, but longer durations are also used. Very short infusions are in theory optimal for parameter estimation [27], but they can disturb accurate dynamic imaging in two ways: the high activity concentration of the bolus can increase dead time losses and induce image artifacts. Secondly, for most analyses of dynamic PET scans, the blood time activity curve (or input function) is required, either obtained from blood sampling or from PET images. The fast occurring peak activity concentration in the blood after a bolus injection can be missed when the sampling frequency is too low.

When the infusion is performed over a long period, the acquired signal may contain insufficient information to enable accurate analysis. The infusion protocol should be optimized for dynamic imaging. Eriksson *et al.* [28] have used an computerized infusion pump in animals to control the concentration of a tracer in the tissue and obtain a specific, desired, curve. Raylman *et al.* [27] studied the infusion duration and sampling of dynamic cardiac PET scans, concluding that an infusion of 30 s is optimal when the input function is derived from the images. Cardiac blood flow measurements performed with a bolus injection and with slow infusion over 2 minutes of [^{15}O]-H_2O were compared by Iida *et al.* [29]. Most accurate results were obtained with a bolus infusion, but only when combined with arterial blood sampling. For routine clinical use, the longer infusion with an IDIF sufficed. Beason-Held *et al.* [30] suggested that a bolus infusion may be too short in dynamic [^{15}O]-H_2O brain activation studies where a subject performs longer, more complex activation tasks. They compared bolus to longer infusions in a short activation task, concluding both techniques yielded similar results. For dynamic acquisitions with ^{18}F-FDG, the lowest fitting errors were found with an 1 min infusion [31]. Mazoyer *et al.* [32] showed that differences in outcome parameters of less than 15% are introduced by varying the infusion between 2 seconds to 2 minutes. For myocardial blood flow measurements with ^{82}Rb, prolongation of the infusion in order to improve quantification was studied by deKemp *et al.* [33]. Slower infusions decreased dead time losses and improved the signal-to-noise ratio. Activity is not homogeneously distributed in cardiac studies which can lead to variations in singles rates around the PET detector ring. Because traditional dead time correction algorithms assume uniform singles rates, this may lead to distortions in the images. This is especially in protocols that use bolus infusions [34].

1.2.4. PET measurement

For an adequate dynamic PET acquisition, the kinetics of a tracer should be monitored in the tissue of interest for a longer period of time, starting at the time of injection. Therefore only one bed position can be scanned, which leads to a small scan range since the axial field of view (FOV) of a PET scanner is limited (*table 1.1*). In some institutions the dynamic PET acquisition is followed by a whole-body static PET scan [38], but this does not provide full dynamic

Model	Axial FOV (mm)
GE Discovery 690 PET/CT [35]	157
Philips Gemini TF PET/CT [36] Philips Ingenuity TF PET/CT	180
Siemens Biograph mCT [37]	218

Table 1.1:
Properties of commercially available PET/CT scanners.

information for the rest of the body. Ho-Shon *et al.* [39] attempted multi-bed position dynamic PET acquisitions, but this cannot be used for full pharmacokinetic analyses.

Scan settings such as the energy window, coincidence timing window or the use of time-of-flight will affect the number of coincidence detections and the quality of the reconstructed images. Each type of scanner has its optimal settings, and usually the settings as recommended by the manufacturer are used. These settings, however, are not specifically optimized for dynamic acquisitions.

The total duration of the scan depends mainly on the radiopharmaceutical that is being used. For tracers with short-lived positron emitters such as ^{15}O (half-life 122 s) or ^{82}Rb (half-life 76 s), the scan requirements are obviously different than those for radionuclides with a longer half-life such as ^{18}F (half-life 110 min). For ^{18}F-FDG in particular, the required scan duration has been studied. For the most accurate results, long (120 min) scans are generally better than shorter (60 min) scans [40]. Especially k_4 cannot be reliably obtained in a 60-min dynamic ^{18}F-FDG PET scan. Other parameters, K_1 in particular, do not require a long acquisition time [32]. For accurate determination of MR_{glc}, the total scan duration should not be too short [41]. On the other hand, long acquisitions are uncomfortable for the patient and hence increase the chances of movement, which reduces accuracy as well. Moreover, long scans increase demand on camera time and are more difficult to schedule. Therefore, some efforts to reduce the scan duration have been made [42-45]. However, besides a loss of accuracy as a result of the shorter acquisition time, analysis may be more complicated as well. At earlier time points, contrast between tissues is lower which can result in incorrect regions of interest (ROI) definition, which may lead to a further decrease in accuracy.

Since the introduction of combined PET/CT scanners, correction for photon attenuation in the body is usually performed with the CT scan. CT-based attenuation correction can introduce several errors which should be taken into account. It is recommended to acquire whole-body PET/CT scans while the patients has the arms up, in order to prevent truncation artifacts [46,47], and to reduce beam hardening and scatter artifacts [48,49]. It is, however, not suitable for dynamic acquisitions, because patients cannot maintain this position for a long period of time.

Metal objects can cause streak artifacts on the CT, which will propagate into the PET image after attenuation correction. Also the use of high density CT contrast can induce artifacts due to overcorrection. A significant increase of 15% in mean SUV was observed in the aorta as a result injection of iodine-based CT contrast [50], which can influence the analysis of dynamic PET scans if the blood input function is obtained from the images. The effect on tumors is much smaller, due to the lower concentration of contrast agent.

1.2.5. Movement

Patient movement in the FOV has a detrimental effect on image quality, and several attempts have been made to either prevent, or correct for motion. Movement not only has an effect on the lesion that is being studied directly, but any IDIF is affected as well, with potentially adverse effects on the accuracy of the analysis [51].

A distinction should be made between periodic movements such as breathing, and incidental movements. Respiratory motion during acquisition causes smearing of activity within a region of motion. In the reconstructed images, a volume includes contributions of different tissues. Respiratory gating can be used to decrease this effect, with detection of the respiratory cycle using optical tracking systems [52], pressure sensors [53], airflow measurements [54] or a point source attached to the patient [55]. These methods are generally applied in static PET acquisitions, but may potentially be used in dynamic acquisitions as well. To reduce respiratory motion artifacts a small part of the breathing cycle (e.g., one “gate”) can be reconstructed, discarding counts ac-

quired during the remaining gates. However, this greatly reduces the number of counts available for reconstruction making it an undesirable method for dynamic PET. Other techniques use information about the breathing cycle to correct for respiratory motion. Menke *et al.* [56], and El Naqa *et al.* [57] showed a method to reduce motion artifacts using deconvolution, but this is a noise-sensitive method. 4D-CT images are used by Li *et al.* [58] to determine organ motion. This information is incorporated in the reconstruction using a deformable model, which combines data acquired during the entire breathing cycle, to one part of it. Wang *et al.* [59] use a similar method, but breathing information is obtained from optical tracking.

Movement of the head in brain PET studies can be prevented to some extent by masks and other head restraints, but translation up to 20 mm and rotations of up to 4° can still be observed [60]. Motion correction strategies can be performed in the image, sinogram or list mode (LM) space. When PET scans are acquired in LM, every coincidence is recorded along with the location of the two detectors and the time of the event. One strategy for image corrections is given by Picard *et al.* [61], where a new time frame is recorded as soon as motion has occurred. Each frame is reconstructed independently and rotated and translated to compensate the motion. This method was originally designed for static acquisition, where the individual time frames are averaged, but it can be used in a dynamic study as well, when the frames are considered separately. Costes *et al.* [62] used a similar technique for dynamic acquisitions, without the need for a motion tracking device. First, the dynamic PET scan was divided in time frames. Since a mismatch between the PET scan and transmission or CT scan can severely affect quantification, each time frame was then reconstructed without corrections. All frames were realigned to compensate for motion, and were finally reconstructed with all corrections enabled. One limitation of this method is that in-frame movement cannot be compensated for. Realigning images after reconstruction has been used as well, because it is relatively easy to implement, but the mismatch between transmission and emission scan can lead to incorrect results [63].

Some motion correction methods in sinogram space are proposed (e.g., [64]), but the most promising method seems to be LM (or event-driven) motion correction. The locations of the two detectors that detected an event are transformed to compensate the movement. In the original work by Menke *et al.* [56], transformations were performed on-the-fly and normalization was thus performed for the transformed detector pair, instead the pair that actually measured the photons. To circumvent this, LM acquisition enables motion correction to be performed post-acquisition. Other issues that should be handled correctly for accurate image reconstruction include the occurrence of events outside the FOV, that would have been recorded when no motion had occurred, and vice versa. Neglecting these issues can produce image artifacts, and reduce the signal-to-noise ratio. Rahmim *et al.* [60] provide an overview of possible methods to resolve aforementioned issues and describe a technique to consider scatter and random events in the motion correction as well. Jin *et al.* [65] compared a LM motion correction strategy with image realignment (both with, and without compensation for the transmission-emission mismatch). They found that, especially for large displacements, the LM correction strategy worked best. A more extensive review of motion correction strategies is given by Rahmim *et al.* [66] and Nehmeh *et al.* [67].

1.3. Image reconstruction

1.3.1. Framing

The usual approach for dynamic PET acquisitions is division of the scan in individual time frames ("framing"). After reconstruction, the resulting series of images can be analyzed.

Many PET scanners have the ability to acquire in LM, which enables the user to repeat the reconstruction with a different framing schedule. In scanners without LM acquisition the framing schedule must be selected before scanning. The framing schedule can have a large influence on the accuracy of the analysis and for this reason the framing schedule was optimized in several studies. Mazoyer *et al.* [32] and Jovkar *et al.* [68] conclude that an optimal frame duration in the early portion of an ^{18}F-FDG PET scan is 30 seconds. However, both studies use an input function obtained with arterial sampling. An accurate image derived input function requires a higher frame rate [27]. Yet Li *et al.* [69] showed an optimized framing schedule with only 6 time frames.

An optimal framing schedule depends on the characteristics of the scanner (mainly sensitivity), the type of radiopharmaceutical and its infusion schedule, and type of analysis. Since there is no consensus, many groups use their own schedule. In *table 1.2*, an overview of framing schedules for ^{18}F-FDG PET scans in oncology is shown.

With reconstruction of individual time frames, images often have a low contrast-to-noise ratio because only a small portion of the total scan time (and therefore limited number of counts) is used for reconstruction of the frame. Rahmim *et al.* [86] review 4D reconstruction techniques, which avoid this disadvantage of individual frame reconstruction. The techniques that can be employed include temporal smoothing, principal component analysis, temporal basis functions and wavelets. With direct reconstruction of parametric images (images showing the value of the parameters that can be obtained from a dynamic scan, such as MR_{glc}), the individual time frame reconstruction is left out. Instead, parametric images are directly reconstructed from the dynamic sinograms [86,87]. Because 4D reconstruction has yet to be implemented in commercial PET software, we will only consider PET scans that have been reconstructed into individual time frames for the remainder of this chapter.

1.3.2. Reconstruction algorithm

Because of the requirements for a high temporal resolution, the number of coincidence detections in one time frame is often small. This has implication for the choice of reconstruction algorithm. The use of filtered back projection (FBP) produces streak artifacts, which can be prevented with iterative reconstruction algorithms such as ordered subsets expectation maximiza-

Table 1.2: Different framing schedules for dynamic ^{18}F-FDG PET in oncology.

Author (Year)	Framing schedule
Hunter *et al*. [70] (1996)	7x15, 4x30, 2x60, 2x120, 4x300, 4x600, 1x900 s
Torizuka *et al*. [71] (1999)	6x10, 3x20, 2x90, 1x300, 5x600 s
Torizuka *et al*. [39] (2000)	8x15, 6x30, 3x300, 4x600 s 8x15, 6x30, 7x300, 2x600 s
Krak *et al*. [72] (2003)	6x5, 6x10, 3x20, 5x30, 5x60, 8x150, 6x300 s
Strauss *et al*. [73] (2004)	10x60, 5x120, 8x300 s
Spence *et al*. [74] (2004)	4x20, 4x40, 4x60, 4x180, 14x300 s
Nishiyama *et al*. [75] (2007), also in [41,76]	4x20, 4x40, 4x60, 4x180, 8x300 s
Parker *et al*. [77] (2005)	6x10, 4x30, 1x120, 11x300 s
Su *et al*. [78] (2005)	10x12, 2x30, 2x60, 1x90, 1x210, 2x300, 1x600, 3x1800 s
Strauss *et al*. [79] (2007)	10x30, 5x60, 5x120, 8x300 s
de Geus-Oei *et al*. [3] (2008)	10x30, 3x300, 3x600 s
Zanotti-Fregonara *et al*. [80] (2009)	12x10, 2x20, 2x150, 3x300, 1x420, 1x600, 1x300, 1x600, 1x300 s
Zanotti-Fregonara *et al*. [81] (2009)	12x10, 2x20, 2x150, 5x300, 1x420, 1x600, 1x1200 s
O'Sullivan *et al*. [82] (2009)	4x15, 4x30, 4x60, 4x180, 14x300 s
Ogden *et al*. [83] (2010)	8x15, 6x30, 5x60, 4x300, 3x600 s
Croteau *et al*. [84] (2010)	12x15, 8x30, 3x60, 10x300 s
Hapdey *et al*. [85] (2011)	12x5, 4x15, 10x30, 6x180, 6x300 s

tion (OSEM). The differences between the two methods, specifically for dynamic PET or at low-count rates, have been studied extensively, [88-94]. Standard iterative reconstruction algorithms suffer from the so-called non-negativity constraint, restricting voxels from attaining negative values. Images can be positively biased in a situation of low count-statistics.

Other reconstruction algorithms have been developed that may better handle short frames with small numbers of coincidence detections. Lower bias can be obtained with ordinary Poisson (OP) OSEM reconstructions, by handling prompt coincidences (true, random and scattered coincidences) and delayed coincidences separately [95]. However, this algorithm does not eliminate the non-negativity constraint. AB-OSEM introduced by Byme [96], which was further improved by Verhaeghe and Reader [97], lowers bias in both static and dynamic images by allowing negative values in the reconstructions.

Time frames with a small number of counts "require" negative values because of the large variance, in order to prevent bias. Decreasing the variance reduces the effect of the non-negativity constraint. Obviously, this can be done by increasing the number of counts (injecting a higher dose or using longer frames), but a reduction in variance and thus bias in the images can also be achieved using a resolution model in the reconstruction. This model describes the response function of the scanner throughout the FOV and improves quantification in dynamic PET [98]. A reconstruction algorithm described by Christian *et al.* [99] decreases variance by using information from the full scan for reconstruction of individual time frames.

As mentioned previously, there are guidelines for the evaluation of image quality, such as those from the National Electrical Manufacturers Association (NEMA) [9,10]. By using the phantom described, various reconstruction algorithms can be evaluated, and settings can be optimized.

1.3.3. Corrections

Besides normalization (and cross calibration) and scatter correction, which have been discussed previously, there are more corrections available that may improve the accuracy of PET quantification. These include dead time, scatter, and random correction [100]. Random coincidences occur when two photons that did not originate from the same decay event are detected by a pair of detectors and are interpreted as a true coincidence detection. Because the two photons are unrelated, they do not contain spatial information. Without correction, these random coincidences can introduce artifacts in the images.

Many photons will scatter along their path through the patient, and could then be detected by a different detector due to their change in direction. This results in an incorrect LOR. These scattered events will have a detrimental effect on the image quality, and should be corrected for. Without correction, errors in parameter estimates in dynamic studies can be introduced [101].

At high count rates, the scanner will experience dead time, where not all coincidences can be recorded because of the time required to recover after an event detection. Dead time has a considerable impact on dynamic PET studies, especially during the initial passage of the tracer through the blood, when the activity is still highly concentrated. Dead time correction should always be applied to limit the disadvantageous effect of dead time on the quantification of PET.

1.3.4. Storage and data management

Since LM-acquisition records all individual coincidence detections, the files tend to be very large. Also the reconstruction can generate a large amount of data, especially with a large number of time frames. For this reason, different compression techniques have been proposed (e.g., [102-104]). In general, events are stored in LM in chronological order. Sorting them spatially can contribute to compression and leads to improvements in reconstruction efficiency as additional advantage [103,104].

1.4. Blood input function

Usually a blood input function, describing the activity concentration in the blood over time, is required in order to analyze dynamic PET scans. As mentioned before, this input function can be obtained by blood sampling or can be derived from the PET images (IDIF). The use of a reference region [105] is another method, where an ROI is compared to a region without specific uptake, often to determine the binding potential of the tracer in the brain. A region without specific uptake may not always be present, and selection of an imperfect region can lead to large errors [106,107]. In this chapter we will focus on the blood input function.

1.4.1. Blood sampling

Obtaining the blood input function with blood samples is usually performed via arterial cannulation. It is an invasive procedure, the processing of blood samples is laborious and it exposes personnel to additional radiation. Although the risks to the patient are only small [108], it remains a procedure one would preferably avoid, as it may also discourage patients to participate in clinical studies. Nevertheless, arterial blood sampling is the gold standard for dynamic PET analysis. As with framing of the PET signal, the sampling rate should be sufficiently high to capture the peak activity concentration in the blood accurately. Besides manual blood sampling, there are automated samplers on the market that take samples at precise moments and measure the activity concentration.

One way to avoid arterial blood sampling, is the use of venous samples. The concentration of the radiotracer in the venous blood, however, is different from the concentration in the arterial blood. Only after arteriovenous equilibrium has been reached, venous samples can substitute arterial blood. This equilibrium is reached at different times after injection, depending on the tracer used. For example, about 10–15 minutes after injection, the equilibrium is reached in ^{18}F-FDG studies [109]. Therefore, the use of venous samples cannot substitute arterial sampling, but in some cases it may be used to correct an image derived input function. Arterialization of venous blood can be achieved through heating, which shunts arterial blood to the venous system [110].

1.4.2. Image derived input function

To obviate the need for arterial blood sampling, the input function could be obtained from the PET images. Especially when a large blood pool (such as the heart) is in the FOV, an IDIF can be used without problems. An IDIF has been validated, obtained in the heart [111], aorta [112] and femoral arteries [113]. In smaller structures, partial volume effects are involved and these may decrease accuracy of the input function. In the early portions of the scan, when the activity concentration in the blood is much higher than in the surrounding tissues, the IDIF will be lower than the real activity concentration in the blood, because of a recovery coefficient lower than one. In the late portions of the scan, uptake of the tracer in the surrounding tissue may spill into the blood region, and artificially increase the IDIF. The combination of the two effects changes the shape of the IDIF, making it more difficult to correct. It is suggested that partial volume effects correction for small blood vessels can only be achieved, if at all, by scaling with one or more blood samples. Zanotti-Fregonara *et al.* [109] reviewed recent literature about IDIFs for dynamic PET studies in the brain and conclude that IDIFs can only be implemented for a small number of tracers. In addition, blood sampling can rarely be avoided completely, especialy for accurate analysis of brain dynamic PET scans.

To obtain an IDIF, a region of interest must be selected. This can be done by manual selection of the blood pool, either on co-registered CT or magnetic resonance imaging (MRI) scans [114], or on the PET images [115]. Other techniques include factor analysis [116] or cluster analysis [117]. Patient motion during the scan not only affects the tissue of interest, but can also alter

the image derived input function, as mentioned previously. This applies to any of the methods used to obtain an IDIF.

Another approach, that could be used for dynamic brain imaging, estimates the input function simultaneously with the kinetic parameters using several brain regions [118,119]. Again, at least one blood sample is recommended [83].

1.4.3. Other methods

Image derived input functions are not always derivable, while blood sampling is not always desirable. In such cases, a population-based input function could be considered. It is an average of a large number of input functions obtained in multiple patients or volunteers. The accuracy can be greatly improved by adjusting the population based input function to the individual patient, for instance by using one blood sample [120]. The use of a population-based input curve, however, has only been successful when used in graphical analyses such as Patlak analysis [121]. Because the exact shape of the input function is also important in full kinetic analyses – instead of only the area under the curve for Patlak – the usefulness of a population based input curve to determine tumor microparameters is limited. Furthermore, when a patient has aberrant blood clearance, the results could be very unreliable.

For some dynamic PET studies, obtaining the blood input function can be very complicated. In studies of the liver, for instance, more than just an arterial input function is required. The liver is not only supplied by blood from the hepatic artery, but a major part of its blood is delivered via the portal vein. This dual blood supply increases the complexity of the input function in dynamic PET scans of the liver. Blood sampling from the portal vein is not feasible due to its location, requiring the blood concentration to be either obtained from the images or modeled. The former is affected by partial volume effects, since the cross sectional area of the portal vein is only about 1 cm^2 [122]. Ignoring the dual-input to the liver by using an arterial input function alone, introduces errors in the pharmacokinetic parameters and estimated blood fraction in the liver [123]. The activity concentration over time in the portal vein can be modeled using the arterial input function, and a model for the transit through the splanchnic circulation [124,125]. In this way, a dual-input function can be used for pharmacokinetic modeling, leading to more accurate results.

1.4.4. Input function adjustments

It is usually impossible to measure the input function in the artery directly supplying the tissue of interest, and so a different location must be chosen. As a result of transit through the arteries, the administered activity is delayed and dispersed. In case of blood sampling, the sampling catheters add to the effect [126]. Hence, a difference may exist between the shape of the measured and real input function. In addition, the arrival of the radioactivity can differ. A discrepancy between the two can cause errors, depending on the type of analysis. Both effects can be corrected to a certain extent. The time delay for instance, by visually determining the arrival time of activity in the tissue of interest and the input function and setting a time delay in the analysis accordingly. Other methods include least squares estimation [127], and spectral analysis [128]. Correction for dispersion is less straightforward, but correction strategies have been described [129,130].

For some radiotracers, correction for metabolites is required. These metabolites may be radioactive and their presence in the blood plasma will alter the input function. They may be taken up from the blood and in turn disturb the time activity curve of the tissue of interest. By measuring the fraction of the radioactive metabolites and radioactive parent substance in blood samples, for instance by high performance liquid chromatography (HPLC) analysis on an individual basis or by using a population based metabolite fraction curve, the presence of metabolites can be corrected to some extent.

1.5. Analysis

For the analysis of dynamic PET scans, a large number of methods exist. The most common approaches are NLLS fitting and graphical analyses (linearized methods). Both can be performed voxel-based, i.e., for every voxel in the image individually. This, however, may be complicated by the low statistical quality of an individual voxel's time activity curve. Instead, regions of interest can be analyzed, improving the reliability of the outcome. However, tissue heterogeneity remains obscure, as the outcome is an average of all voxels in the ROI.

1.5.1. Region of interest definition

Definition of the ROIs can be performed using automatic methods, or by manual delineation on the PET images, or any co-registered scan (e.g., CT or MRI). Manual delineation of ROIs can be biased and suffers from relatively large inter- and intraobserver variability [131,132]. Automatic delineation is usually based on a single time frame, but approaches that use the dynamic information exist [133]. Single-frame methods are often threshold based, e.g., all voxels with a value of at least 50% of the maximum voxel in a lesion. The most appropriate threshold to recover the true volume of a lesion depends on many factors, such as the volume of the lesion, background activity and the scanner resolution. To obtain the volume, small lesions will require a lower threshold than large lesions, as a result of the partial volume effect [134]. A method described by Van Dalen *et al.* [135] can be used to determine this threshold, although several assumptions may not be valid in all cases. For instance, the lesion is assumed to be spherical and homogeneous, two attributes rarely observed in practice. Other methods use, for instance, clustering [136] or textural features of the images [137,138]. In some dynamic studies, especially in the brain, predefined ROIs are used [139]. The scan is co-registered to a brain atlas where functional regions have been predefined. This atlas can be obtained from other patients or healthy volunteers, or could be defined on images of another modality, such as MRI.

1.5.2. Compartment modeling

Compartment modeling is one of the most commonly applied method for the analysis of dynamic PET acquisitions. NLLS methods are used to fit the measured PET signal and any sampled input function. Details about the mathematics involved in compartment modeling are described elsewhere [140]. A compartment model can become very complex when more compartments are added. These additional parameters in the fitting procedure generally lead to a better fit of the data, but can be influenced by noise in the measurement alone, rather than any real parameter [141]. The choice of the model (i.e., the number of compartments and the number of rate constants) that is best suitable to describe the kinetics of the tracer can be evaluated by the Akaike information criterion [142] or Schwartz criterion [143]. The addition of parameters is weighed against improvement in goodness of fit.

In the case of ^{18}F-FDG, the 2-tissue compartment model is typically chosen, either with 3 or 4 rate constants, shown in *figure 1.1*. The rate constant k_3 represents phosphorylation of ^{18}F-FDG to ^{18}F-FDG-6-phosphate. The rate of dephosphorylation, indicated with k_4, is only low in mammalian tissues and sometimes even assumed to be negligible. The uptake of ^{18}F-FDG is regarded irreversible in case of a k_4 of zero, and reversible in case of non-zero k_4. The rate constant K_1 relates to the delivery of ^{18}F-FDG from the arterial plasma to the tissue, and k_2 to the reverse process.

A number of assumptions should be made when a complex biological system is described by a relatively simple compartment model. One important assumption is that the system is in steady state, i.e., the rate constants do not change during the experiment. Moreover, the tissue under investigation, whether being a single voxel or a ROI, is assumed to be homogeneous. Both assumptions are unlikely completely true, but are required to model the dynamic PET scan. Errors can be

introduced by these assumptions. Tissue heterogeneity, for instance, can reduce the accuracy of the parameter estimation [144-146], or in some cases lead to an apparent value of a rate constant which is in reality negligible [147,148].

1.5.3. Graphical analyses

Nonlinear fitting of compartment models is computationally expensive and sensitive to noise. Linearization can then be a solution, for instance using graphical approaches. The most frequently used graphical analyses are the Patlak plot [121] and the Logan plot [149]. The Patlak plot can be used for any type of compartment model, as long as there is one irreversible compartment. The plot becomes linear when the various reversible compartments are in equilibrium. A disadvantage of this approach is that only one parameters (the influx constant or K_i) can be estimated, instead of the individual rate constants. Moreover, steady-state must occur during the scan, and one compartment is assumed to be fully irreversible. Nevertheless the Patlak plot has become a frequently used method, especially in metabolism studies with ^{18}F-FDG. Principally because the influx constant calculated with the Patlak plot has been shown to be consistent with the constant calculated after full compartment modeling [150].

The Logan plot is a commonly used method to analyze receptor-ligand studies. It can be used for tracers with reversible uptake. Noise with a mean of zero in the images can introduce bias in this graphical analysis, more than in full compartment modeling [151].

1.5.4. Other methods

The compartment modeling using NLLS and graphical analyses methods are the most commonly applied methods for the analysis of dynamic PET scans, but there are others. These include the autoradiographic method, which is described by Sokoloff *et al.* [152]. Using a number of population based parameters, an input function and a single scan, the MR_{glc} can be estimated in a simplified and fast manner. However, the many assumption can reduce accuracy of the results. A second alternative to NLLS and graphical approaches is the use of basis functions [106]. With this method, the compartment model can be transformed to a linear problem. A range of possible pharmacokinetic parameters is used to precalculate solutions.

1.5.5. Weighting

Not every time frame in a dynamic PET acquisition has the same statistical quality. For instance, short frames are reconstructed with a smaller number of coincidences than long frames. Also the total activity in the FOV varies over time and influences statistics. In pharmacokinetic analyses, a weighting factor can be applied to each measurement or time frame. Frames with higher statistical quality can be regarded to be more important than frames with a lower quality. Various methods are available to determine the weights, and the choice of weighting has influence on the accuracy of the analysis. The weights are often determined from the measured (noisy) signal in combination with the frame duration, or uniform (or unit) weighting is used. Dai *et al.* [40] have evaluated different weighting methods and conclude that nonlinear least squares regression can better be performed with uniform weighting than weighting based on the noisy signal. This was concluded by Thiele and Buchert [153] and Yaqub *et al.* [154] in earlier studies as well. Weighting based on the estimated time activity curve can slightly improve accuracy, but at a higher compu-

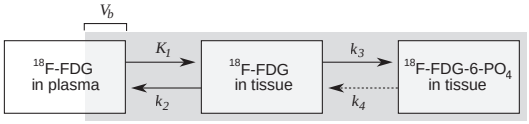

Figure 1.1: The 2-tissue compartment ^{18}F-FDG model with pharmacokinetic rate constants K_1, k_2, k_3, and k_4. The measured PET signal (shown as a gray box) is a combination of ^{18}F-FDG in tissue and a fraction of blood plasma, V_b.

tational cost [40]. Yaqub *et al.* [154] have evaluated five different weighting methods, showing a difference between the 1- and 2-tissue compartment model. In the 1-tissue compartment model, the difference in accuracy of different weighting methods is much smaller than in the 2-tissue compartment model.

1.6. Outline of the thesis

One of the most frequently used radionuclides in PET is ^{18}F (with the most commonly used radiopharmaceutical in PET being ^{18}F-FDG to study glucose metabolism). Other research objectives can require other radionuclides. These generally have different properties, which should be taken into account in the study design. Aspects such as positron energy and branching fraction, and presence of additional gamma emissions influence the final PET images. This is assessed in *chapter 2*, in which four commonly used PET radionuclides are compared. The effect of the radionuclide on the image quality was studied. *Chapter 3* describes characterization of the Inveon small-animal PET scanner, regarding sensitivity and resolution. The effect of reconstruction settings on the image quality is discussed in *chapter 4*. Many different algorithms are available for the reconstruction of PET data, each with many possible settings. For a selection of widely used reconstruction algorithms the effect of different settings on the image quality is determined. Parameters such as the number of iterations and type of filtering are varied, and optimal reconstruction settings are obtained.

All foregoing quantification and image quality aspects are not specific for dynamic PET, i.e., they should be considered for both static and dynamic PET studies. The division of a dynamic acquisition in time frames, however, is. Determination of an accurate framing schedule is often disregarded in the design of dynamic PET studies, even though its influence should not be underestimated. The error that can be introduced by an incorrect schedule is pointed out in *chapter 5*. Moreover, an optimal framing schedules is generated and tested using computer simulations and by using the dynamic PET scans of 15 patients. The objective is to determine a framing schedule that minimizes the estimation error of the pharmacokinetic parameters. To this purpose, the noise characteristics of a PET scanner were determined for a realistic simulation of a dynamic PET signal.

An application of dynamic PET is shown in *chapter 6*. Heterogeneity in tumors is evaluated with dynamic ^{18}F-FDG PET. Heterogeneous uptake of ^{18}F-FDG within tumors can be observed to a certain degree in static PET images as well, but underlying physiological differences remain unclear. In this study, tumors are divided in segments with decreasing metabolic activity. Differences in tumor microparameters between these segments are explored.

In general, the acquistion time of a dynamic ^{18}F-FDG PET scan is about one hour. This is a long time for patients to lie still and it can be logistically inconvenient. For this reason, several studies have been performed to reduce the required acquisition time without affecting the parameters that can be obtained from the data. In a shortened dynamic PET scan, there are two aspects that should be taken into account. First of all, there is a reduced number of data points available for determining the microparameters. In addition, because dynamic PET analyses are usually performed in ROIs, the shorter acquisition can alter the results of the analysis. As a result of continuing tracer uptake, especially in tumors, the contrast at earlier time points is lower than after 60 min. This impedes accurate tumor delineation. The effect of ROI definition alone on tumor microparameters is described in *chapter 7*. This aspect is usually ignored when shortened dynamic PET acquisitions are evaluated.

Finally, in *chapter 8*, overall findings in this thesis are discussed, followed by an outlook for future work.

2. Image-Quality Assessment for Several Positron Emitters Using the NEMA NU 4-2008 Standards in the Siemens Inveon Small-Animal PET Scanner

Jonathan A. Disselhorst[1], Maarten Brom[1], Peter Laverman[1], Cornelius H. Slump[2], Otto C. Boerman[1], Wim J.G. Oyen[1], Martin Gotthardt[1] and Eric P. Visser[1]

[1] Department of Nuclear Medicine, Radboud University Nijmegen Medical Centre, Nijmegen, The Netherlands

[2] Institute of Technical Medicine, University of Twente, Enschede, The Netherlands

Reprinted by permission of the Society of Nuclear Medicine from: J Nucl Med. 2010;51:610-617

Abstract

The positron emitters ^{18}F, ^{68}Ga, ^{124}I, and ^{89}Zr are all relevant in small-animal PET. Each of these radionuclides has different positron energies and ranges and a different fraction of single photons emitted. Average positron ranges larger than the intrinsic spatial resolution of the scanner (for ^{124}I and ^{68}Ga) will deteriorate the effective spatial resolution and activity recovery coefficient (RC) for small lesions or phantom structures. The presence of single photons (for ^{124}I and ^{89}Zr) could increase image noise and spillover ratios (SORs).

Methods: Image noise, expressed as percentage SD in a uniform region (%SD), RC, and SOR (in air and water) were determined using the NEMA NU 4 small-animal image-quality phantom filled with 3.7 MBq of total activity of ^{18}F, ^{68}Ga, ^{124}I, or ^{89}Zr. Filtered backprojection (FBP), ordered-subset expectation maximization in 2 dimensions, and maximum a posteriori (MAP) reconstructions were compared. In addition to the NEMA NU 4 image-quality parameters, spatial resolutions were determined using small glass capillaries filled with these radionuclides in a water environment.

Results: The %SD for ^{18}F, ^{68}Ga, ^{124}I, and ^{89}Zr using FBP was 6.27, 6.40, 6.74, and 5.83, respectively. The respective RCs were 0.21, 0.11, 0.12, and 0.19 for the 1-mm-diameter rod and 0.97, 0.65, 0.64, and 0.88 for the 5-mm-diameter rod. SORs in air were 0.01, 0.03, 0.04, and 0.01, respectively, and in water 0.02, 0.10, 0.13, and 0.02. Other reconstruction algorithms gave similar differences between the radionuclides. MAP produced the highest RCs. For the glass capillaries using FBP, the full widths at half maximum for ^{18}F, ^{68}Ga, ^{124}I, and ^{89}Zr were 1.81, 2.46, 2.38, and 1.99 mm, respectively. The corresponding full widths at tenth maximum were 3.57, 6.52, 5.87, and 4.01 mm.

Conclusion: With the intrinsic spatial resolution (±1.5 mm) of this latest-generation small-animal PET scanner, the finite positron range has become the limiting factor for the overall spatial resolution and activity recovery in small structures imaged with ^{124}I and ^{68}Ga. The presence of single photons had only a limited effect on the image noise. MAP, as compared with the other reconstruction algorithms, increased RC and decreased %SD and SOR.

2.1. Introduction

PET with ^{18}F is widely used in a range of applications, using tracers such as ^{18}F-FDG, ^{18}F-fluoromisonidazole (FMISO), ^{18}F-fluoroazomycin arabinoside (FAZA), and ^{18}F-fluoro-3'-deoxy-3'-L-fluorothymidine (FLT) [155]. In some applications, other positron-emitting radionuclides are being used in the preclinical setting and have also found their way to clinical PET. The use of positron emitter–labeled monoclonal antibodies that combine the specificity of an antibody with the resolution of PET requires radionuclides with half-lives that match the half-life of antibodies in the circulation (>48 h). With half-lives of 100 and 78 h, respectively, ^{124}I and ^{89}Zr are potentially suitable for this purpose.

In many situations, a generator-produced radionuclide such as ^{68}Ga is preferable over a cyclotron-produced radionuclide (such as ^{18}F, ^{124}I, and ^{89}Zr), because it can be eluted from a generator on-site and does not require a cyclotron in the vicinity of the PET facility. Peptides conjugated to appropriate chelators such as 1,4,7,10-tetraazacyclododecane-1,4,7,10-tetraacetic acid or 1,4,7-triazacyclononane-1,4-7-triacetic acid can be labeled with ^{68}Ga [156].

Some of these radionuclides have disadvantageous properties for PET: for instance, their high positron energy and corresponding large positron range in tissue (e.g., ^{68}Ga and ^{124}I) may reduce the spatial resolution of the image. Also, the presence of single γ-photons (e.g., ^{124}I and ^{89}Zr) can have detrimental effects. Single γ-photons with energy above the lower discriminator value of the energy window can lead to coincidence detections without spatial correlation with the location of the positron emission, leading to an additional, more or less uniform background concentration. Also, higher noise levels can be expected as a result of a higher rate of multiple detections, which effectively decreases the rate of detected true positron annihilation events. Finally, the single γ-photons may influence the dead-time and associated corrections of the scanner.

The effects of large positron range and additional singles emissions can be corrected to some extent. For a small object centered in the field of view (FOV), the emitted single γ-photons produce a uniform distribution of counts [157,158], allowing a simple uniform subtraction to correct for single photons. This is, however, not functional in the present scanner software (Inveon Acquisition Workplace 1.2.2.2 [IAW]; Siemens Medical Solutions). The effects of dead time are corrected for to some degree by the dead-time correction algorithm. The reconstruction software can use scatter correction to reduce the adverse effects of scatter of the annihilation photons on the reconstructed images. Correction for positron range has been described by Bai *et al*. [159] but is still experimental and not yet available in standard reconstruction software for commercial small-animal PET scanners.

It is relevant to establish the performance of a PET scanner for different radionuclides, not only in terms of spatial resolution and sensitivity but especially with regard to overall image quality. Performance evaluation guidelines for clinical PET scanners have been available for a long time (NEMA NU 2 [9,160,161]), but guidelines for small-animal PET have been introduced only recently (NEMA NU 4 [10]). For the Siemens Inveon small-animal PET scanner, performance characterizations have been established earlier using ^{18}F or ^{22}Na sources [162-165]. The purpose of this study was to compare image-quality parameters of ^{18}F, ^{68}Ga, ^{124}I, and ^{89}Zr using the NEMA NU 4 image-quality phantom.

2.2. Materials and methods

2.2.1. PET Scanner

The Siemens Inveon is a high-resolution small-animal PET scanner consisting of 4 rings of 16 lutetium oxyorthosilicate detector blocks. The blocks are composed of 20 × 20 crystals,

each 1.5 × 1.5 × 10 mm^3. The detector ring diameter of 16.1 cm and axial length of 12.7 cm provide a relatively large maximum acceptance angle of 38.3° (aspect ratio, 0.79), contributing to the high-peak sensitivity exceeding 10% [162,163]. Light guides couple the detector blocks to photomultiplier tubes. Emission data are acquired in list mode and can be sorted into 2-dimensional (2D) or 3-dimensional (3D) sinograms. To correct for photon attenuation, transmission measurements with a rotating ^{57}Co point source can be performed.

The reconstruction algorithms available in IAW are filtered backprojection (FBP), 3D reprojection, 2D and 3D ordered-subset expectation maximization (OSEM2D and OSEM3D, respectively), and maximum a posteriori (MAP) reconstruction [166].

2.2.2. Radionuclides

The radionuclides selected for this study are ^{18}F—as it is the most widely used and required for standard image-quality measurements by NEMA NU 4—and the following 3 others (with different properties), which are increasingly used in PET: ^{124}I as a radionuclide with a high positron energy and a high abundance of singles, with an energy within the default 350–650 keV window; ^{68}Ga, which also emits high-energy positrons but only an insignificant amount of singles; and ^{89}Zr, which does not have high-energy positron emission and for which the specific challenge lies in the abundance of singles. With an energy of 909 keV, these photons fall outside the default energy window, apart from a portion of the down-scattered photons with lower energy. Their high yield (0.99 γ-photons vs. 0.23 positrons) could contribute to the detector dead time. An overview of the physical properties of the radionuclides is presented in *table 1* [167,168].

^{18}F, ^{124}I, and ^{89}Zr were obtained from BV Cyclotron VU. The respective agents were ^{18}F-FDG, a $Na^{124}I$ solution in 0.1 M NaOH, and a desferrioxamine-conjugated antibody labeled with ^{89}Zr in NaCl–gentisic acid with 0.5% bovine serum albumin. $^{68}GaCl_3$ was eluted with 0.1 M HCl from a (TiO-based) $^{68}Ge/^{68}Ga$ generator (Cyclotron Co.).

2.2.3. NEMA NU 4 Image-Quality Phantom

The NEMA NU 4-2008 image-quality phantom is a 50-mm-long, 30-mm-diameter cylinder made of polymethylmethacrylate and consists of different regions to analyze 3 distinct aspects of image quality. A schematic view of the phantom is shown in *figure 1*. The first 20 mm of the phantom body are solid, with 5 fillable rods with diameters of 1, 2, 3, 4, and 5 mm. These are used to determine the recovery coefficient (RC), defined as the ratio between the measured activity concentration in the rods and the activity concentration measured in the uniform area. The RC is theoretically limited between 1 and 0 ($0 < RC \leq 1$).

A fillable cylindric chamber with 2 hollow cylinders (length, 14 mm; inner diameter, 8 mm) makes up the remaining 30 mm of the phantom. One of these cylinders is filled with air, the other

Table 2.1: Physical properties of ^{18}F, ^{68}Ga, ^{124}I, and ^{89}Zr.

Property	^{18}F	^{68}Ga	^{124}I	^{89}Zr
Half-life	109.8 min	67.6 min	4.18 d	3.27 d
β+ yield	0.97	0.89	0.23	0.23
Mean β+ energy (MeV)	0.25	0.83	0.83	0.40
Mean β+ range in water (mm)	0.62	3.48	3.48	1.23
Single γ-yield in range of 350–650 keV	0	0	0.64	0
Single γ-yield outside range of 350–650 keV	0	0.03 (1.08 MeV)	0.10 (722.8 keV) 0.19 (>1.5 MeV)	0.99 (909.2 keV)

The physical properties of radiotracers are based on data from Health Physics Society [167] and International Commission on Radiation Units and Measurements [168].

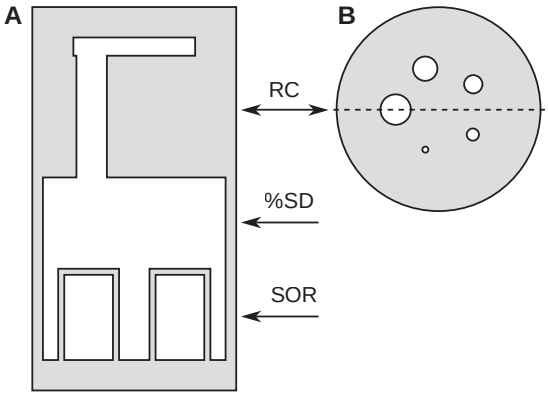

Figure 2.1:
Cross-sectional diagram of NEMA NU 4 image-quality phantom. Gray represents solid polymethylmethacrylate, and white represents hollow, fillable compartments. Views are coronal (A) and transverse through rod (B).

with nonradioactive water. These 2 cylinders are used to determine the spillover ratio (SOR) in water and air, defined as the mean value in each cold cylinder divided by the mean in the uniform area. Both cylinders are nonradioactive, but as a result of scattered photons, nonzero positron range, randoms, or other effects, the reconstructed images may still display activity in these compartments. The SOR is theoretically limited between 1 and 0 ($0 \leq RC < 1$).

The central, uniform region of the phantom is used to determine the percentage SD (%SD, the SD divided by the mean multiplied by 100%) as a measure of noise. The phantom was constructed according to the NEMA NU 4 specifications by Agile Engineering.

Before each measurement, the phantom was checked for and cleaned of any activity remaining from previous use. The total volume of the phantom regions filled with activity equaled 20.7 mL. The 5 rods and the large chamber, excluding the cold cylinders, were filled with radioactive solutions with an activity (at the start of the scan) of 3.7 MBq as defined by NEMA.

2.2.4. Glass Capillaries

In addition to the NEMA NU 4 image-quality assessment, the transaxial spatial resolutions of the 4 radionuclides were determined. According to NEMA specifications, resolution should be measured using ^{22}Na point sources of less than 0.3 mm in diameter. However, the 4 radionuclides used in this study cannot be easily converted into point sources with these dimensions. Therefore, more practical line sources were used. Glass capillaries of 1.15-mm inner diameter (1.55-mm outer diameter) were filled with radioactive solutions. Activity concentrations of greater than 30 MBq/mL were used in a volume of about 70 μL. The glass capillaries were placed in a 2-cm-diameter plastic tube filled with water.

2.2.5. Data Acquisition and Image Reconstruction

Settings for NEMA NU 4 Image-Quality Phantom

The standard NEMA NU 4 protocol advises a 20-min emission scan with an initial ^{18}F activity of 3.7 MBq. However, these numbers have been specifically tailored for ^{18}F, and because of the differences in positron yield (or branching fraction) and half-life, the numbers may not be directly applicable for scanning other radionuclides. For a proper comparison of different radionuclides, equal numbers of positrons need to be emitted from the phantom during the scan. This can be achieved by adjusting either the total scan duration or the start activity. In *table 2*, the total number of positron emissions that would occur under exact NEMA NU 4 specifications—that is, during a 20-min acquisition with an initial activity of 3.7 MBq—is given in column 1. The values in column 2 represent the length of acquisition required to obtain 4.03×10^9 positron emissions given a start activity of 3.7 MBq. In column 3, the required start activity is given to

Table 2.2:
Required scan durations or start activities to obtain equal numbers of emitted positrons for each radionuclide.

Radionuclide	Number of positron emissions ($\times 10^9$) using NEMA specifications	Corrected scan duration (s)	Corrected start activity (MBq)
^{18}F	4.03	1,200	3.70
^{68}Ga	3.58	1,373	4.17
^{124}I	1.03	4,707	14.47
^{89}Zr	1.01	4,824	14.81

obtain 4.03×10^9 positron emissions during a 20-min scan. In this study, the scan duration was adjusted.

The phantom was positioned on the scanner bed and manually centered in the FOV, using the built-in lasers of the scanner for guidance. The phantom always contained 178.7 Bq/μL (corresponding to a total activity of 3.7 MBq) at the start of the scan. Default energy and timing window settings of 350–650 keV and 3.432 ns, respectively, were used. Other window settings have not been considered in this study, to allow for comparison with results in the literature and because NEMA NU 4 requires these acquisition parameters to be constant throughout all tests.

For all radionuclides, a transmission scan of the phantom was made for about 3,600 s with a ^{57}Co point source of 82 MBq. Because the scans were not obtained on the same day, the transmission scan durations were adjusted to account for transmission source decay to ensure an identical statistical quality of the attenuation correction.

All default settings were used for histogramming; that is, the emission data were histogrammed into 3D sinograms with a span of 3 and a maximum ring difference of 79, delays were subtracted, and global dead-time correction was applied. The transmission data were rebinned into single slices, with a span of 17 and a ring difference of 42, and global dead-time correction was applied.

The PET data were reconstructed with various algorithms to compare their performance for different radionuclides. The image matrix size was $256 \times 256 \times 159$ with pixel sizes of $0.43 \times 0.43 \times 0.80$ mm^3 for MAP and $0.39 \times 0.39 \times 0.80$ mm^3 for FBP and OSEM2D. FBP was used with a ramp filter (cutoff at Nyquist frequency), and OSEM2D was performed using 4 iterations and 16 subsets. Before these 2D reconstructions, the 3D sinogram data were Fourier rebinned. OSEM3D–MAP reconstructions were performed using 2 OSEM3D iterations and 16 subsets, followed by 18 MAP iterations. The smoothing factor β in MAP reconstructions was set to 0.1, and the uniformity constraint was set to uniform variance. These settings led to the most favorable results using ^{18}F, considering both RC and %SD (unpublished results).

All MAP reconstructions were preceded by 2 OSEM3D iterations, because OSEM3D converges faster than MAP. Here, MAP will refer to this combined OSEM3D and MAP reconstruction.

IAW provides a scatter-correction algorithm based on direct calculation from analytic formulas and source and object geometry [169]. Although NEMA recommends reconstruction with all corrections applied, we opted for reconstruction with and without scatter correction, mainly because of some unexpected deformations induced by the correction algorithm.

Settings for Glass Capillaries

The glass capillaries were positioned in the center of the FOV, aligned with the axis of the scanner, and scanned until at least 3.5 million counts were acquired using the default energy window of 350–650 keV and timing window of 3.432 ns. Images were obtained using FBP with the default settings (ramp filter with a cutoff at Nyquist frequency) and $512 \times 512 \times 159$ matrices with pixel sizes of $0.19 \times 0.19 \times 0.80$ mm^3. This matrix size was selected to obtain a profile with a sufficient number of datapoints to allow for the accurate determination of spatial resolution. Attenuation and scatter corrections were not applied.

2.2.6. Image Analysis

The reconstructed images were processed with a program written in MATLAB (version R2008a; The MathWorks) to determine the various image-quality parameters and full width at half and at tenth maximum (FWHM and FWTM, respectively) for the glass capillaries. The program provided accurate and reproducible placement of volumes of interest (VOIs) in all images.

The %SD were determined in a 22.5-mm-diameter (75% of the inner phantom diameter), 10-mm-long cylindric VOI drawn over the center of the uniform region of the phantom.

To determine the RCs, the image slices containing the central 10 mm of the rods were averaged and circular regions of interest were drawn around each rod with a diameter twice their physical diameter. The positions of the maximum values in these regions of interest were used to create line profiles in the axial direction through the rods. The RCs were determined from the mean values along these 5 profiles, divided by the mean activity concentration in the uniform area.

Two 4-mm-diameter (50% of the physical inner diameter), 7.5-mm-long cylindric VOIs were drawn over the center of the air- and water-filled compartments. The means of these cold regions divided by the mean of the uniform radioactive area provide the SOR.

As mentioned above, the NEMA NU 4 image-quality guidelines have been created for the use of ^{18}F, but with a few adjustments these can also be used for other radionuclides. However, the determination of the SORs is not completely applicable to long-range positron emitters. Because the radius of the scatter compartments is relatively small, the measured activity in these regions not only is due to scattered photons but also contains contributions from positrons emitted in the body part of the phantom and annihilating in the scatter compartments. For a fair comparison, the 2 effects should be separated. Decreasing the diameter of the VOI in the scatter compartments is the only method achievable in the NEMA NU 4 image-quality phantom, but the diameter of the compartments is too small to fully eliminate positron range effects. However, by assessing the difference in SOR between the compartments filled with water and air, the accuracy of corrections can be evaluated. Whereas the SOR in water comprises photon scatter and the effect of positron range, only scattered photons contribute to the SOR in air; because of the large positron range (>1 m), almost no annihilations occur in air.

2.2.7. Capillary Measurements

The slices containing the capillary in the reconstructed images were aligned by placing their maximum in the center before being summed to form a single image. Profiles in tangential and radial directions through the center were averaged to determine the FWHM and FWTM for all radionuclides. These widths were determined according to NEMA NU 4 guidelines: maxima were determined in a parabolic fit through the peak pixel and its 2 nearest neighboring pixels. The FWHM and FWTM were determined by linear interpolation between adjacent pixels at half and one tenth of this maximum, respectively. FWHM and FWTM were not corrected for source geometry.

2.3. Results

In the following sections, the results for each of the NEMA NU 4 image-quality parameters are presented. A complete list of all the obtained parameter values can be found in *supplemental tables1–4* (see pages 32-35).

2.3.1. Spatial Resolution

Results of the spatial resolution measurements using the glass capillaries are summarized in *table 3*. For Gaussian profiles, the FWHM-to-FWTM ratio equals $\sqrt{ln\,2 / ln\,10} \approx 0.55$.

Table 2.3: Spatial resolutions for 4 radionuclides measured with glass capillaries surrounded by water.

Radionuclide	Mean β+ energy (MeV)	Measured profiles			Palmer *et al*. [170], FWHM-to-FWTM ratio
		FWHM (mm)	FWTM (mm)	FWHM-to-FWTM ratio	
^{18}F	0.25	1.81	3.57	0.51	0.54
^{68}Ga	0.83	2.46	6.52	0.38	0.39
^{124}I	0.83	2.38	5.87	0.41	0.39
^{89}Zr	0.40	1.99	4.01	0.50	0.50

FWHM-to-FWTM ratios are indicative of deviation from Gaussian profiles. Values were not corrected for source dimensions.

Nongaussian profiles with extended tails are characterized by smaller FWHM-to-FWTM ratios. Palmer *et al*. [170] have modeled spatial resolutions for a hypothetical imaging system with an intrinsic spatial resolution of 1.5 mm. Corresponding FWHM-to-FWTM ratios have been added for comparison, as well as the mean positron energies. The data in *table 3* indicate that ^{18}F yielded the best approximation (0.51) of the theoretic Gaussian ratio. The measured and modeled ratios for ^{68}Ga (0.38 and 0.39, respectively) and ^{124}I (0.41 and 0.39, respectively) are substantially lower, indicating a larger tail section of the curve. *Figure 2* shows the measured profiles.

2.3.2. Uniformity

The %SD of the NEMA NU 4 image-quality phantom is shown in *figure 3*. The largest differences are not found among different radionuclides but among the various reconstruction algorithms for the same radionuclide. MAP yields more than 2 times smaller %SD values than OSEM2D and FBP. The differences per reconstruction algorithm between the 4 radionuclides are much smaller, with a maximum SD of 0.8 percentage point for MAP. Scatter correction had a limited effect on %SD, with a maximum decrease of 0.8 percentage point for ^{124}I in the OSEM2D images.

2.3.3. RCs

The RCs of the 5 different rods are shown in *figure 4*. Because the result obtained with ^{89}Zr is similar to that obtained with ^{18}F, and ^{124}I is similar to ^{68}Ga, the 4 radionuclides can be clearly separated into 2 groups: the long- and short-range positron emitters. The influence of

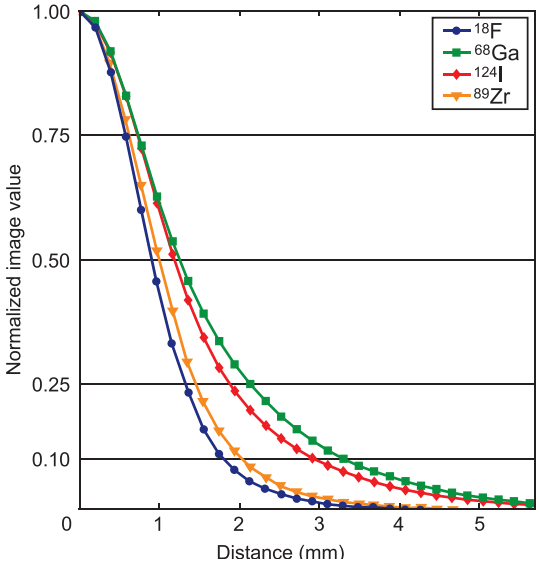

Figure 2.2:
Measured line profiles through glass capillaries filled with positron-emitting aqueous solutions, surrounded by water. Profiles were obtained from 512 × 512 FBP reconstruction by aligning and summing image slices containing capillary and averaging profiles in tangential and radial directions through center. Profiles are shown in 1 direction only. Values were not corrected for source dimensions.

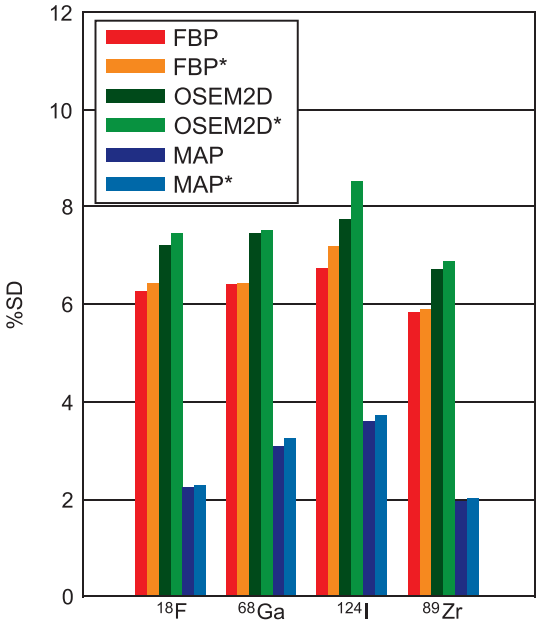

Figure 2.3:
%SD in uniform phantom region. Reconstruction performed with scatter correction are indicated with an asterisk (*).

scatter correction on RC was limited (data not shown). The largest differences in RC were introduced by the choice of reconstruction algorithm. This especially holds for the short-range positron emitters, for which the 2D reconstruction algorithms clearly showed lower RC values than did reconstruction with MAP, with a maximum difference between OSEM2D and MAP of 36%. With MAP, for large-diameter rods, the recovery even rose beyond the ideal limit of 1. This effect could possibly be attributed to an overshoot at the edges, commonly referred to as the Gibbs effect [171].

For the long-range positron emitters, the differences in RC were smaller, but FBP and OSEM2D still showed lower values than did MAP, with a maximum difference between OSEM2D and MAP of 18%.

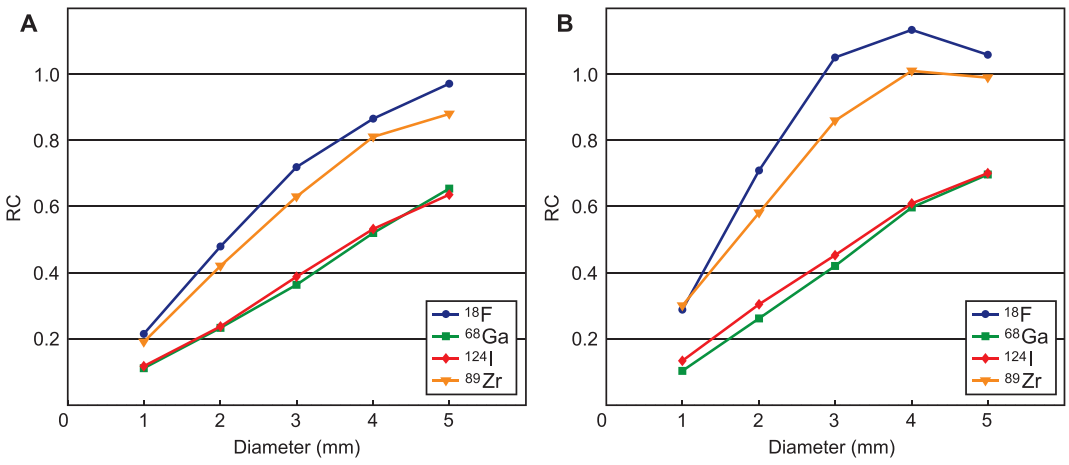

Figure 2.4: RCs of different rods for various radionuclides, reconstructed with FBP (A) and MAP (B). OSEM2D results were similar to those of FBP.

2.3.4. Accuracy of Corrections

In *figure 5*, the SORs in the water and air compartments are shown for the 4 radionuclides for different reconstruction algorithms with and without scatter correction. The differences in SOR were large, especially in water. Again, 2 groups can be distinguished: the short-range positron emitters, with a clearly lower SOR (mean value for all reconstruction algorithms, 0.03 for ^{18}F and 0.04 for ^{89}Zr), and the large-range positron emitters (mean value for all reconstruction algorithms, 0.10 for ^{68}Ga and 0.14 for ^{124}I). A reduction in SOR was achieved by MAP, as compared with OSEM2D and FBP. In the case of air, this reduction is evident for all radionuclides except ^{89}Zr. In the case of water, the reduction is obvious only for ^{18}F. Scatter correction lowered SOR, especially for ^{124}I.

Two unexpected features were also observed in the data. First, MAP performed poorly without scatter correction in the case of ^{124}I. The SOR was lowered substantially (a decrease of 0.09) with scatter correction enabled, possibly related to the abundance of single γ-photons in the 350–650 keV energy window. Second, only for ^{89}Zr, MAP produced a relatively high SOR in air (0.05), which is even higher than the SOR in water (0.04).

The scatter-correction algorithm included in IAW introduced certain deformation artifacts in some parts of the reconstructed images, as shown in *figure 6*. The ^{124}I image, especially, was affected, whereas the effect was not prominent in the images of the other radionuclides. This could again be related to an abundance of single γ-photons for ^{124}I in the 350–650 keV energy window, for which correction was unavailable. No abnormalities, however, arose in the NEMA NU 4 parameters by this artifact.

2.4. Discussion

From the results for the RCs of the small rods and capillary measurements, this study shows that the positron range limits the spatial resolution for modern small-animal PET scanners. This is in line with the observations by Liu and Laforest [172], who analyzed 5 different radio-

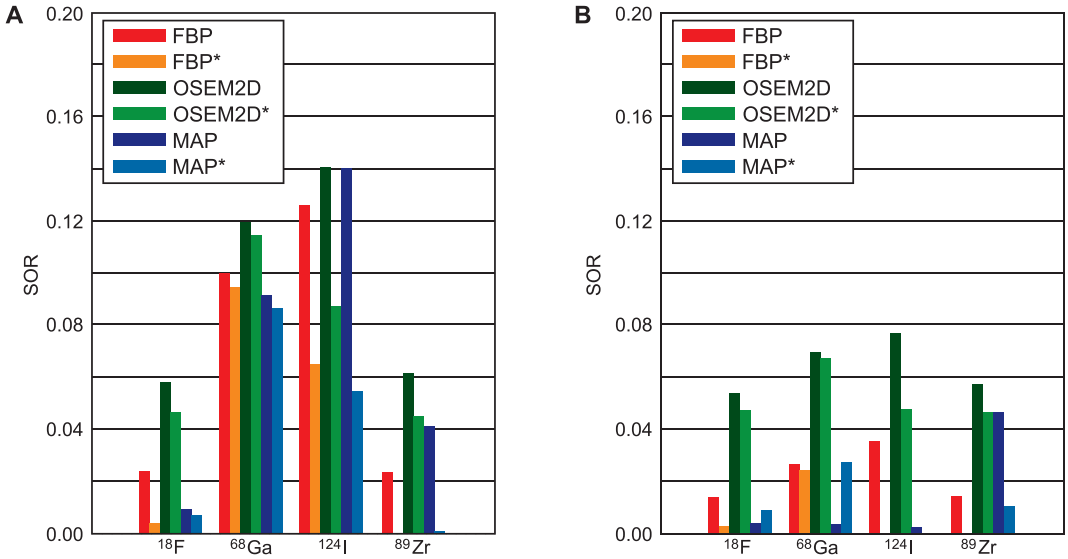

Figure 2.5: SORs in water (A) and air (B) compartments for various radionuclides, reconstructed with 3 different algorithms. Some SOR values are (close to) zero, and not visible in graph. Reconstruction performed with scatter correction are indicated with an asterisk (*).

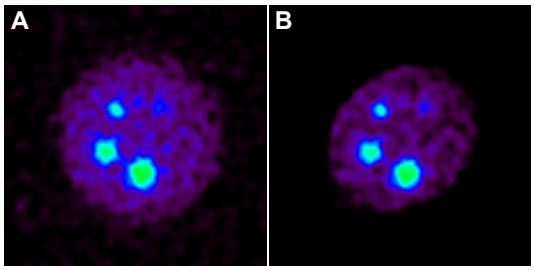

Figure 2.6:
Transverse cross-section through rod area of phantom filled with ^{124}I solution. Images without (A) and with (B) scatter correction are shown. Scatter-corrected image clearly displays ellipsoid deformation.

nuclides (^{18}F, ^{61}Cu, ^{68}Ga, ^{94m}Tc, and ^{86}Y). These were, however, not measured using the standard NEMA NU 4 image-quality phantom and parameter definitions and were for a different type of scanner (microPET Focus 120; Siemens).

The SORs in water were considerably higher for ^{124}I and ^{68}Ga than for ^{18}F and ^{89}Zr. These results should, however, be interpreted carefully. The high SOR values for the long-range positron emitters in water do not imply incorrect scatter- or other correction algorithms for these radionuclides, because they are largely caused by positrons emitted in the body part of the phantom and annihilating in the water-filled scatter compartment. Selecting a smaller VOI within the scatter compartments could partly improve this. However, with a maximum positron range of more than 10 mm and an inner diameter of the compartment of only 8 mm, no valid volume can be drawn. For a real evaluation of the SOR in water, either a different phantom should be used, or correction for positron range should be applied during reconstruction. In air, the average positron range for all radionuclides is greater than 1 m, and scattered and single photons will be the main contributors to the SOR in air, allowing analysis of correction algorithm performance.

As mentioned before, the additional single γ-photons for ^{124}I and ^{89}Zr could have contributed to the image noise, resulting in a higher %SD. However, this was not observed. Activities normally injected in small animals (<10 MBq) remain well below the maximum noise-equivalent counting rate measured by Bao *et al*. [162]and Kemp *et al*. [164] for ^{18}F. System dead time does not play a large role for these activities. As the activity in the FOV increases, increasing numbers of multiple detections will occur. No differences (in count-rate performance) are to be expected for ^{68}Ga, ^{124}I, and ^{89}Zr, because the total number of emitted γ-photons (both annihilation and single γ-photons) is lower for these 3 radionuclides than for ^{18}F.

In addition to image quality, accurate quantification is an important factor in PET. There are 2 issues concerning quantification, one of which depends on a properly performed cross-calibration. During this procedure, a known amount of radioactivity is used in a calibration phantom. With a scaling factor, the measured PET counts per pixel are correlated to the true activity concentration. Another quantification issue concerns the proper scaling of regions with different activity concentrations within the same phantom or animal. In the case of large numbers of single photons (e.g., for ^{124}I), this could be a problem. Without correction, these singles give an additive, nearly uniform contribution to the activity concentrations in all regions. However, a fixed scaling factor obtained from cross-calibration will lead to concentration-dependent quantification errors, because the spurious activity concentration from the single emissions should have been subtracted before applying the scaling. Because the NEMA NU 4 image-quality phantom contains 1 activity concentration (apart, of course, from all cold regions with zero activity), performance measurements with respect to quantification should be the subject of further study.

In earlier studies with PET radionuclides that emitted single γ-photons in the acquisition energy window—such as ^{124}I [173-175], ^{76}Br [157,176-178], and ^{86}Y [176,179-181]—quantification proved to be affected by the single γ-photons. Both under- and overestimation of activity concentration occurred, depending on the activity concentration used for cross-calibration.

Basically, MAP performs better than the other 2 algorithms for all 3 image-quality parameters. Accurate modeling of the system response and the statistical nature of the data and incorporation of these during reconstruction improves the resolution recovery of the MAP algorithm. Another distinctive feature of the MAP algorithm is the smoothing factor β, which regulates the variance and resolution in the image [166]. Both aspects improve the image quality of MAP, as compared with both FBP and OSEM2D.

2.5. Conclusion

In terms of image-quality parameters, the Inveon small-animal PET scanner performs best for ^{18}F. The largest differences in the RC and SOR are found between the group of radionuclides with large positron ranges (^{124}I and ^{68}Ga) and the one with short ranges (^{18}F and ^{89}Zr). Only the %SD is unaffected by the positron range.

The abundance of single γ-photons affects only slightly the image-quality parameters; all 4 radionuclides yield roughly the same values for %SD.

Although scatter correction leads in some cases to deformation artifacts in the images, this technique is beneficial for the SOR and affects only slightly the %SD and RC. Especially with respect to the RC and %SD, the MAP algorithm performs much better than do the other reconstruction techniques.

2.6. Acknowledgments

This work was supported by NIH grant 1R01 AG 030328-01.

Supplemental data

Supplemental Table 2.1: Results for ^{18}F

Matrix size	256×256											128×128					
Algorithm*	FBP			OSEM2D			MAP - Var.			MAP - Res.		FBP		OSEM2D		MAP - Var.	
Attenuation correction‡	-	+	+	-	+	+	-	+	+	+	+	+	+	+	+	+	+
Scatter correction‡	-	-	+	-	-	+	-	-	+	-	+	-	+	-	+	-	+
Unif. %SD	7.577	6.274	6.423	8.306	7.218	7.447	3.716	2.245	2.282	8.191	7.639	6.336	6.487	7.303	7.520	1.259	1.283
Water																	
SOR	-0.010	0.024	0.004	0.042	0.058	0.046	0.000	0.009	0.007	0.002	0.001	0.026	0.006	0.059	0.047	0.003	0.001
%SD	-509.495	204.466	1262.477	20.893	19.195	20.910	96.385	128.506	90.405	435.114	320.501	191.016	854.197	20.192	22.030	166.399	216.786
Air																	
SOR	0.152	0.014	0.003	0.149	0.054	0.047	0.202	0.004	0.009	0.001	0.003	0.016	0.005	0.056	0.049	0.005	0.004
%SD	31.987	302.652	1458.822	17.455	19.337	20.716	12.644	209.348	93.020	643.200	238.922	272.717	861.469	21.096	22.511	115.330	117.590
RC Rod																	
5 mm	0.963	0.972	0.976	1.031	1.041	1.059	1.012	1.058	1.071	1.031	1.047	0.967	0.971	1.043	1.056	0.971	0.977
4 mm	0.858	0.865	0.868	0.895	0.906	0.911	1.086	1.133	1.141	1.077	1.067	0.857	0.860	0.884	0.887	0.861	0.868
3 mm	0.702	0.718	0.716	0.787	0.804	0.816	1.069	1.051	1.074	1.092	1.137	0.694	0.692	0.778	0.781	0.601	0.600
2 mm	0.465	0.479	0.472	0.597	0.611	0.604	0.740	0.709	0.742	0.747	0.796	0.479	0.472	0.578	0.550	0.346	0.330
1 mm	0.209	0.214	0.201	0.331	0.337	0.367	0.317	0.288	0.307	0.291	0.308	0.214	0.201	0.303	0.299	0.131	0.116
%SD Rod																	
5 mm	8.172	6.959	7.098	13.015	12.335	13.126	4.275	3.456	3.266	8.559	8.117	7.339	7.461	10.482	10.942	1.892	1.513
4 mm	8.020	6.810	7.024	12.103	11.389	14.328	4.273	3.746	3.444	8.912	7.930	6.919	7.123	9.826	10.447	1.854	1.940
3 mm	8.117	6.908	7.125	12.663	11.971	13.746	4.851	4.199	3.606	8.734	8.109	6.801	7.029	9.805	11.195	3.102	2.980
2 mm	9.882	8.797	8.883	13.606	12.930	15.074	5.083	4.101	4.219	8.579	8.116	8.842	8.929	11.186	11.878	2.474	2.906
1 mm	13.335	12.527	13.105	19.058	18.552	23.162	12.127	11.366	9.116	11.256	9.896	12.558	13.135	16.127	18.906	3.831	3.602

Radionuclide: ^{18}F, scanning time: 1200 s, start activity: 3.7 MBq. * Algorithms: FBP: Ramp-filter, cutoff at Nyquist frequency. OSEM2D: 4 Iterations, 16 subsets. MAP: 2 OSEM3D iterations, 16 subsets, 18 MAP iterations. Smoothing Factor β = 0.1, Var: Uniform variance, Res: Uniform resolution. ‡ Corrections: +: with corrections, -: without correction.

Supplemental Table 2.2: Results for ^{68}Ga

Matrix size	256×256											128×128					
Algorithm*	FBP			OSEM2D			MAP - Var.			MAP - Res.		FBP		OSEM2D		MAP - Var.	
Attenuation correction‡	-	+	+	-	+	+	-	+	+	+	+	+	+	+	+	+	+
Scatter correction‡	-	-	+	-	-	+	-	-	+	-	+	-	+	-	+	-	+
Unif. %SD	7.334	6.401	6.435	8.247	7.457	7.519	3.983	3.074	3.242	8.672	8.512	6.444	6.479	7.500	7.557	2.374	2.442
Water																	
SOR	0.070	0.100	0.094	0.099	0.119	0.114	0.088	0.091	0.087	0.075	0.069	0.104	0.098	0.123	0.118	0.089	0.077
%SD	88.106	58.800	62.543	26.829	23.498	24.100	30.503	40.260	29.995	82.716	77.028	59.867	63.527	26.095	26.795	46.326	52.940
Air																	
SOR	0.159	0.027	0.024	0.163	0.069	0.067	0.192	0.004	0.028	0.000	0.000	0.025	0.022	0.070	0.067	0.029	0.026
%SD	36.456	202.179	224.461	18.244	26.631	27.050	14.497	271.538	48.309	964.622	752.428	221.147	247.878	28.637	29.091	98.663	100.742
RC Rod																	
5 mm	0.652	0.653	0.653	0.730	0.729	0.735	0.700	0.697	0.667	0.677	0.667	0.630	0.630	0.660	0.665	0.627	0.626
4 mm	0.521	0.520	0.518	0.544	0.545	0.549	0.620	0.597	0.588	0.596	0.604	0.517	0.516	0.536	0.538	0.492	0.490
3 mm	0.365	0.363	0.360	0.397	0.397	0.390	0.429	0.419	0.413	0.437	0.431	0.356	0.353	0.397	0.391	0.332	0.319
2 mm	0.231	0.233	0.230	0.269	0.271	0.271	0.267	0.261	0.268	0.275	0.263	0.227	0.224	0.248	0.246	0.188	0.176
1 mm	0.104	0.110	0.106	0.113	0.119	0.119	0.107	0.103	0.117	0.109	0.103	0.110	0.106	0.113	0.113	0.073	0.073
%SD Rod																	
5 mm	8.624	7.890	7.920	10.908	10.372	10.352	5.336	3.893	3.911	9.579	9.583	7.701	7.734	11.322	11.365	2.546	2.599
4 mm	9.054	8.478	8.506	14.560	12.315	12.429	5.164	4.069	4.289	9.544	9.508	9.369	9.410	14.282	12.337	3.256	3.305
3 mm	9.414	8.984	9.032	12.714	12.351	12.908	8.186	5.594	6.832	10.935	11.071	9.494	9.567	14.572	15.051	3.133	3.150
2 mm	12.464	12.051	12.199	17.543	16.958	17.800	13.459	7.717	8.078	11.339	11.600	11.127	11.257	14.884	15.716	3.398	4.495
1 mm	20.251	19.519	20.092	30.312	29.156	26.510	19.735	14.668	17.820	18.410	19.738	19.538	20.112	26.405	27.165	6.176	6.395

Radionuclide: ^{68}Ga, scanning time: 1373 s, start activity: 3.7 MBq. * Algorithms: FBP: Ramp-filter, cutoff at Nyquist frequency. OSEM2D: 4 Iterations, 16 subsets. MAP: 2 OSEM3D iterations, 16 subsets, 18 MAP iterations. Smoothing Factor β = 0.1, Var: Uniform variance, Res: Uniform resolution. ‡ Corrections: +: with corrections, -: without correction.

Supplemental Table 2.3: Results for ^{124}I

Matrix size	256×256											128×128					
Algorithm*	FBP			OSEM2D			MAP - Var.			MAP - Res.		FBP		OSEM2D		MAP - Var.	
Attenuation correction‡	-	+	+	-	+	+	-	+	+	+	+	+	+	+	+	+	+
Scatter correction‡	-	-	+	-	-	+	-	-	+	-	+	-	+	-	+	-	+
Unif. %SD	7.515	6.737	7.190	8.372	7.745	8.528	4.435	3.593	3.714	8.087	8.033	6.786	7.238	7.819	8.546	2.375	2.443
Water																	
SOR	0.086	0.126	0.065	0.110	0.140	0.087	0.087	0.140	0.054	0.144	0.058	0.124	0.063	0.139	0.086	0.128	0.065
%SD	63.515	42.688	87.330	21.819	20.339	27.027	48.488	18.973	63.414	27.438	67.160	44.180	91.613	20.612	27.345	16.233	30.339
Air																	
SOR	0.160	0.035	-0.005	0.165	0.077	0.048	0.189	0.003	0.000	0.004	0.000	0.039	-0.002	0.079	0.049	0.029	0.015
%SD	35.565	150.404	-1117.180	17.694	25.346	31.332	19.418	385.300	546.933	356.437	572.723	140.046	-3575.863	26.932	33.348	97.526	121.803
RC Rod																	
5 mm	0.629	0.636	0.621	0.660	0.668	0.671	0.688	0.701	0.697	0.700	0.714	0.631	0.615	0.674	0.648	0.659	0.628
4 mm	0.527	0.532	0.509	0.563	0.573	0.568	0.590	0.610	0.584	0.605	0.576	0.532	0.508	0.568	0.556	0.525	0.485
3 mm	0.380	0.387	0.356	0.431	0.437	0.449	0.451	0.453	0.455	0.464	0.468	0.381	0.350	0.430	0.428	0.359	0.312
2 mm	0.226	0.237	0.195	0.253	0.263	0.262	0.309	0.304	0.291	0.311	0.299	0.236	0.190	0.258	0.243	0.209	0.160
1 mm	0.101	0.117	0.063	0.100	0.118	0.065	0.118	0.134	0.027	0.135	0.027	0.115	0.060	0.119	0.052	0.090	0.015
%SD Rod																	
5 mm	8.792	8.430	8.904	11.667	11.080	18.974	6.996	4.940	4.252	10.694	9.275	8.896	9.538	12.839	16.789	2.443	2.775
4 mm	9.383	8.899	9.576	15.720	15.750	24.209	6.955	4.574	5.291	10.406	10.145	8.936	9.527	13.726	18.640	2.481	2.690
3 mm	10.138	9.777	10.553	16.244	15.746	29.846	6.170	4.767	5.490	8.935	9.557	10.085	11.135	14.610	23.172	3.123	3.335
2 mm	12.533	11.781	14.335	21.111	17.296	50.416	9.874	7.450	7.210	10.575	10.291	11.695	14.239	14.480	33.282	3.863	4.933
1 mm	28.988	25.180	49.573	35.631	32.178	126.953	22.269	14.872	62.731	17.848	63.283	21.791	54.486	30.769	95.017	7.144	55.073

Radionuclide: ^{124}I, scanning time: 4707 s, start activity: 3.7 MBq. * Algorithms: FBP: Ramp-filter, cutoff at Nyquist frequency. OSEM2D: 4 Iterations, 16 subsets. MAP: 2 OSEM3D iterations, 16 subsets, 18 MAP iterations. Smoothing Factor β = 0.1, Var: Uniform variance, Res: Uniform resolution. ‡ Corrections: +: with corrections, -: without correction.

Supplemental Table 2.4: Results for ^{89}Zr

Matrix size	256×256											128×128					
Algorithm*	FBP			OSEM2D			MAP - Var.			MAP - Res.		FBP		OSEM2D		MAP - Var.	
Attenuation correction‡	-	+	+	-	+	+	-	+	+	+	+	+	+	+	+	+	+
Scatter correction‡	-	-	+	-	-	+	-	-	+	-	+	-	+	-	+	-	+
Unif. %SD	7.139	5.828	5.902	7.812	6.717	6.878	3.591	1.962	2.013	7.385	6.694	5.862	5.936	6.804	6.950	0.939	1.063
Water																	
SOR	-0.013	0.024	-0.003	0.045	0.061	0.045	0.013	0.041	0.001	0.004	0.003	0.023	-0.004	0.061	0.045	0.009	0.007
%SD	-381.629	201.925	-1470.236	31.007	28.032	31.632	59.224	27.919	341.808	289.860	194.386	202.818	-1033.119	27.588	31.236	125.233	122.492
Air																	
SOR	0.142	0.014	-0.001	0.145	0.057	0.047	0.187	0.046	0.011	0.013	0.018	0.017	0.001	0.058	0.047	0.015	0.016
%SD	35.602	323.396	-3369.079	19.476	27.691	30.122	13.270	33.124	117.446	177.423	95.896	287.180	4759.897	28.725	31.279	105.872	96.048
RC Rod																	
5 mm	0.882	0.877	0.888	0.926	0.918	0.943	0.990	0.988	1.003	0.966	0.984	0.870	0.881	0.906	0.921	0.891	0.889
4 mm	0.813	0.815	0.821	0.867	0.866	0.894	1.053	1.015	1.079	1.016	1.043	0.795	0.803	0.850	0.874	0.737	0.747
3 mm	0.618	0.630	0.632	0.676	0.696	0.706	0.899	0.857	0.914	0.926	0.978	0.620	0.622	0.681	0.689	0.529	0.532
2 mm	0.410	0.420	0.417	0.505	0.517	0.557	0.600	0.579	0.627	0.639	0.680	0.421	0.418	0.506	0.543	0.333	0.340
1 mm	0.186	0.188	0.180	0.250	0.251	0.270	0.316	0.304	0.256	0.272	0.274	0.188	0.180	0.250	0.273	0.116	0.107
%SD Rod																	
5 mm	7.458	6.225	6.305	11.174	10.403	10.909	3.998	2.156	2.290	8.136	7.523	6.518	6.599	8.454	8.889	1.096	1.435
4 mm	8.125	7.012	7.103	12.456	11.814	12.579	4.130	2.675	2.451	7.851	7.329	6.885	6.941	9.635	9.922	1.192	1.422
3 mm	7.858	6.641	6.727	12.269	11.486	12.845	5.548	3.310	3.211	8.181	7.492	7.117	7.160	11.103	12.219	2.731	2.741
2 mm	8.401	7.296	7.416	12.200	11.502	13.945	5.872	3.688	2.915	8.333	7.620	7.322	7.442	12.247	13.429	1.663	1.692
1 mm	12.745	12.460	12.943	19.850	19.786	23.734	9.456	7.780	6.976	10.753	9.853	12.475	12.958	17.628	18.617	4.772	4.304

Radionuclide: ^{89}Zr, scanning time: 4824 s, start activity: 3.7 MBq. * Algorithms: FBP: Ramp-filter, cutoff at Nyquist frequency. OSEM2D: 4 Iterations, 16 subsets. MAP: 2 OSEM3D iterations, 16 subsets, 18 MAP iterations. Smoothing Factor β = 0.1, Var: Uniform variance, Res: Uniform resolution. ‡ Corrections: +: with corrections, -: without correction.

3a. Spatial Resolution and Sensitivity of the Inveon Small-Animal PET Scanner

Eric P. Visser[1], Jonathan A. Disselhorst[1], Maarten Brom[1], Peter Laverman[1], Martin Gotthardt[1], Wim J.G. Oyen[1] and Otto C. Boerman[1]

[1] Department of Nuclear Medicine, Radboud University Nijmegen Medical Centre, Nijmegen, The Netherlands

Reprinted by permission of the Society of Nuclear Medicine from: J Nucl Med. 2009;50:139-147

Abstract

The Inveon small-animal PET scanner is characterized by a large, 127-mm axial length and a 161-mm crystal ring diameter. The associated high sensitivity is obtained by using all lines of response (LORs) up to the maximum ring difference (MRD) of 79, for which the most oblique LORs form acceptance angles of 38.3° with transaxial planes. The result is 2 phenomena that are normally not encountered in PET scanners: a parallax or depth-of-interaction effect in the axial direction and the breakdown of Fourier rebinning (FORE). Both effects cause a deterioration of axial spatial resolution. Limiting the MRD to smaller values reduces this axial blurring at the cost of sensitivity. Alternatively, 3-dimensional (3D) reconstruction techniques can be used in which the rebinning step is absent. The aim of this study was to experimentally determine the spatial resolution and sensitivity of the Inveon for its whole field of view (FOV).

Methods: Spatial resolution and sensitivity were measured using filtered backprojection (FBP) with FORE, FBP with LOR angle-weighted adapted FORE (AFORE), and 3D ordered-subset expectation maximization followed by maximum a posteriori reconstruction (OSEM3D/MAP).

Results: Tangential and radial full width at half maximum (FWHM) showed almost no dependence on the MRD using FORE and FBP. Tangential FWHMs were 1.5 mm in the center of the FOV (CFOV) and 1.8 mm at the edge of the FOV (EFOV). Radial FWHMs were 1.5 and 3.0 mm in the CFOV and EFOV, respectively. In contrast, axial FWHMs increased with the MRD and ranged between 1.1 and 2.0 mm in the CFOV and between 1.5 and 2.7 mm in the EFOV for a MRD between 1 and 79. AFORE improved the axial resolution for a large part of the FOV, but image noise increased. OSEM3D/MAP yielded uniform spatial resolution in all directions, with an average FWHM of 1.65 ± 0.06 mm. Sensitivity in the CFOV for the default energy and coincidence time window was 0.068; peak sensitivity was 0.111.

Conclusion: The Inveon showed high spatial resolution and high sensitivity, both of which can be maintained using OSEM3D/MAP reconstruction instead of rebinning and 2D algorithms.

3a.1. Introduction

The Inveon (Siemens) small-animal PET scanner differs from its predecessor, the microPET Focus 120 (F120; Siemens), by its larger lutetium orthosilicate (LSO) detector blocks, improved processing of high-speed events [182-185], and shorter, tapered light guides coupling the detector blocks to the photomultiplier tubes [186]. The Inveon contains 4 rings of 16 blocks—20 × 20 detectors of 1.5 × 1.5 mm^2 each, resulting in an axial length of 127 mm. The F120 consists of 4 rings of 24 blocks—12 × 12 detectors of the same size, leading to an axial length of 76 mm. *Table 1* compares the geometric properties of the Inveon with several other commercial crystal-based small-animal PET scanners.

The main advantage of the larger axial field of view (FOV) of the Inveon is the higher detection efficiency (or sensitivity), with a peak value as specified by the manufacturer of greater than 0.1 in the center of the FOV (CFOV) for the maximum width of the energy window. However, high sensitivity is obtained only when using all lines of response (LOR), up to the maximum ring difference (MRD) of 79. With its crystal ring diameter of 161 mm and axial length of 127 mm (aspect ratio, 0.79), the most oblique LORs form acceptance angles of 38.3° with the transaxial planes, leading to 2 phenomena that are normally not encountered in PET scanners. First, the parallax or depth-of-interaction (DOI) effect due to crystal penetration of oblique LORs in the axial direction cannot be ignored, and second, conventional Fourier rebinning (FORE) for 2-dimensional (2D) reconstruction techniques [187] breaks down. Both effects lead to a deterioration of the axial spatial resolution. Parallax or DOI effects are well known in PET scanners but have been described and measured mainly for the radial resolution at radial offsets from the CFOV [188] and not for the axial resolution. The performance of FORE for large acceptance angles has been reported by Matej *et al*. [189] for angles up to 26.2°. A considerable deterioration of the axial resolution for large acceptance angles, especially at large radial offsets, was found in that study.

The advantage of using FORE with 2D reconstruction techniques such as filtered backprojection (FBP) or 2D ordered-subset expectation maximization (OSEM2D) is high processing speed. FORE has, therefore, been implemented in most standard software packages for both clinical and preclinical PET scanners. The deterioration of axial resolution by FORE could be avoided by using 3-dimensional (3D) reconstruction techniques in which the rebinning step is not present and all LORs contained in the 3D sinograms are directly used in the image reconstruction. Although algorithms such as 3D OSEM (OSEM3D), maximum a posteriori reconstruction (MAP), and 3D reprojection (3DRP) are available on some (preclinical) scanners, the use of FORE and 2D reconstruction is still widespread. This is mainly due to the higher complexity and long recon-

Table 3a.1: Geometric properties of several commercial, crystal-based small-animal PET scanners.

PET scanner	Crystal element size (mm^3)	No. of crystal rings	Detector material	Axial length (mm)	Crystal ring diameter (mm)	Aspect ratio *	Largest LOR acceptance angle † (degrees)
Inveon	1.5 × 1.5 × 10	80	LSO	127	161	0.79	38.3
F120 [12]	1.5 × 1.5 × 10	48	LSO	76	147	0.52	27.3
Mosaic [13]	2 × 2 × 10	52	GSO	119	197	0.60	28.0 ‡
Vista [14]	1.45 × 1.45 × (8 + 7)	26	LYSO/GSO phoswich	48	118	0.41	22.1
ClearPET [15,16]	2 × 2 × (10 + 10)	32	LYSO/ LuYAP phoswich	110	135	0.81	39.2

* Aspect ratio is crystal ring diameter divided by axial length.
† LOR acceptance angle is angle between LOR and transaxial planes.
‡ This LOR angle is determined by software; LOR angle from aspect ratio would be somewhat larger.
GSO = gadolinium oxyorthosilicate; LYSO = lutetium yttrium orthosilicate; LuYAP = lutetium yttrium aluminum perovskite

struction times of the 3D algorithms, which can take orders of magnitude more time than 2D algorithms, including the time for the rebinning. Especially in routine clinical settings, longer reconstruction times can be a prohibitive factor for using 3D reconstruction algorithms. Moreover, because of requirements about the minimum patient port size in clinical scanners, aspect ratios are generally not large and errors due to parallax or DOI effects and FORE will, in general, be smaller than those in small-animal scanners.

A different, more practical way to improve the axial resolution while still using FORE and 2D reconstruction is to decrease the maximum LOR acceptance angle by reducing the MRD down to a level at which FORE becomes more accurate. This, however, reduces the effective sensitivity of the scanner, because fewer LORs and, thus, fewer measured coincidences are included in the rebinning and reconstruction process. On the other hand, the sensitivity will become more uniform across the axial FOV. This method is also applied in clinical, whole-body PET scanners, in which bed overlap issues may be important. The Biograph TrueV PET/CT scanner (Siemens), for instance, uses as a default MRD of 38, with the number of crystal rings equaling 52. Similar choices have been made for the older Biograph types of scanners and the ECAT EXACT (Siemens).

The aim of this study was to experimentally determine the spatial resolution and sensitivity of the Inveon for its whole FOV. The standard reconstruction and rebinning were FBP and FORE. A comparison was made with a new, adapted FORE (AFORE) algorithm recently incorporated in the standard scanner software. This algorithm uses LOR angle-weighted FORE in such a way that coincidence counts belonging to large LOR acceptance angles are rebinned with reduced weighting factors. Detailed information about this algorithm was not provided by the manufacturer. Further, a combination of OSEM3D and MAP was used for 2 different settings of the MAP prior. The results were compared with those obtained by the 2D reconstruction techniques.

Finally, the quality of images of real animals also depends on parameters such as scatter fraction and counting-rate performance. Assessment of overall image quality with these parameters considered, however, was outside the scope of this study.

3a.2. Materials and methods

Spatial resolution and sensitivity were measured using a ^{22}Na point source with an active diameter of less than 0.25 mm embedded in a Lucite disk (Isotope Products Laboratories [IPL]). The activity of the point source was 0.918 MBq, as measured in a dose calibrator (VDC-404; Veenstra) in our laboratory. This value was corrected for the point source geometry because the device had been calibrated for extended sources (syringes). The accuracy of the activity is ±4%, which results from ±3% as specified by the manufacturer and an additional ±1% to account for uncertainties in the point source geometry correction.

Spatial-resolution measurements were not corrected for source dimension, positron range, or noncolinearity of the 2 photons involved in positron annihilation. The point source was placed in the FOV of the scanner for transaxial positions ranging from 0 to 46 mm from the center and from 0 to 7 mm in the opposite direction. This range was determined by the vertical bed-motion limitations of the scanner. The axial positions covered a total range of 200 mm around the CFOV. This large axial range also was used to record coincidence counts for source positions outside the axial FOV. The transaxial step size was 1 mm for the range of -7 to 12 mm and 2 mm for the range of 12–46 mm. The axial step size was 0.80 mm (approximate thickness of 1 transaxial plane) for the range of -8 to 8 mm and 4.78 mm (6 transaxial planes) elsewhere. All measurements along the transaxial direction were repeated 4 times, with the point source stepped in the axial direction (step size, 0.2 mm) to obtain oversampled axial profiles by interleaving. For each position of the point source, 10 million coincidence counts were collected.

Spatial resolution was determined using FORE and FBP with a ramp filter at the Nyquist frequency. The pixel size in transaxial planes was 0.194 mm, and the plane separation was 0.796 mm. The image matrix size was 512 × 512 × 159. Profiles through count-distribution peaks were drawn in these orthogonal directions for a middle plane to determine transaxial radial and tangential resolutions at each point source position. According to the National Electrical Manufacturers Association (NEMA) requirements (NEMA-NU2–2007 [9]), the full width at half maximum (FWHM) and full width at tenth maximum (FWTM) were determined by linear interpolation between adjacent pixels at half or one tenth of the profile maximum value, which was determined by a parabolic fit using the peak point and its 2 nearest neighbors. Axial resolutions were obtained in the same way using the interleaved profiles.

Before reconstruction, the list-mode data were histogrammed with a span of 3 and MRDs of 79, 46, 25, 13, and 1 into 3D sinograms. The maximum acceptance angles corresponding to these MRDs are 38.3°, 24.9°, 14.4°, 7.9°, and 1.1°, respectively. An MRD of 46 was specifically chosen for a sensitivity comparison with the F120, which is geometrically similar except for the smaller axial length and number of crystals per detector block. In principle, for a direct one-to-one comparison, an MRD of 47 should be chosen in accordance with the 48 detector rings in the F120. However, the closest attainable setting in theInveon is 46, because for complete segments in the 3D sinograms, MRD is restricted by $MRD = (n + 1/2) \times span - 1/2$ [190].

In addition, spatial resolution was determined using AFORE, characterized by its LOR angle-based weighting factors. Spatial resolution was determined for the same point source positions and NEMA procedure as described above, again using FBP with the same pixel and image matrix sizes.

For a limited number of point source positions in the radial direction, data were reconstructed using OSEM3D/MAP (2 OSEM3D iterations and 18 MAP iterations). The MAP reconstructions were performed with $\beta = 0.5$ and 1.5 and were optimized for uniform resolution. The transaxial pixel size was 0.331 mm, and the image matrix size was 256 × 256 × 159. The same settings as for FBP (transaxial pixel size, 0.194 mm; matrix size, 512 × 512 × 159) were not possible because of the limited number of P-matrices and blur kernels available for these 3D reconstruction algorithms. However, the transaxial pixel size of 0.331 mm was still small enough to determine tangential and radial resolutions accurately (NEMA requires the pixel size to be no more than one third of the expected FWHM, which is clearly fulfilled).

The axial resolutions, on the contrary, were determined in the same way as for FBP, using the 0.2-mm interleaved profiles. The reason for limiting the number of point source positions was the long reconstruction time for OSEM3D/MAP. One reconstruction using the above-mentioned matrix size and iterations setting took approximately 4 h on a personal computer (Dell), with 16-GB RAM and a Dual-Core Xeon 5160 processor (Intel) running at 3 GHz under Windows XP (64 bit; Microsoft). Because of the axial interleaving, each reconstruction was performed 4 times, leading to a total reconstruction time of 16 h per point source position.

The coincidence timing window (Δt) and the energy window (ΔE) were used at their default settings of 3.4 ns and 350–650 keV, respectively. For the CFOV only, additional measurements with a ΔE of 250–750 keV and a Δt of 2.8, 4.1, and 4.7 ns were performed. Randoms were subtracted using a delayed-window technique. Dead-time correction was based on a global singles-rate estimate.

The sensitivity of the scanner was calculated as the ratio of the histogrammed trues rate and the rate at which photon pairs are emitted from the point source. The latter was determined using the point source activity, taking into account the positron branching ratio of 0.899 for ^{22}Na [191]. Sensitivity data were generated for all point source positions as specified above. Furthermore, to cover the complete FOV, additional radial sensitivity profiles with radial steps of 5 mm were re-

corded for an MRD of 79 in transaxial planes that were axially separated by 10 mm.

Because of its LOR angle–dependent weighting factors that reduce the contribution of oblique LORs to the reconstructed image, it might be expected that AFORE be associated with lower effective sensitivities than FORE. Because the histogrammed trues rate is the same for both rebinning algorithms, a comparison can only be made on the basis of noise levels in reconstructed images. For this purpose, we compared the noise levels in images of a homogeneous ^{68}Ge cylinder using FORE and AFORE with FBP and a transaxial matrix size of 128 × 128.

Finally, IAW 1.0.2 (Inveon Acquisition Workplace; Siemens) was used for the FORE and FBP results, and IAW 1.0.4 was used for the AFORE/FBP and OSEM3D/MAP results. The return to version 1.0.2 was necessary because the FORE algorithm was not available anymore in version 1.0.4. The FBP algorithms were exactly the same in both versions.

3a.3. Results

3a.3.1. Spatial Resolution

The results for transaxial tangential and radial resolutions using FORE and FBP are shown in *figure 1A* for an MRD of 79. These transaxial resolutions were found to be almost independent of MRD; therefore, the results for the other MRDs have been left out for clarity. The axial resolutions, on the contrary, were highly dependent on the MRD and increased as a function of radial distance from the CFOV, as shown in *figure 1B*.

According to NEMA-NU2-2007 [9], which was designed for the characterization of clinical PET scanners, spatial resolution should be reported for source positions at radial offsets of 1 and 10 cm to obtain numbers that can be considered representative for the CFOV and the edge of the FOV (EFOV), respectively. For small-animal scanners, NEMA prescriptions do not exist. We chose to average the resolution values for radial offsets between 2 and 5 mm, yielding representative numbers for the CFOV (averaged over 8 point source positions), and between 36 and 46 mm, representing the radial EFOV (averaged over 6 point source positions). The resulting FWHMs have been summarized in *table 2*.

Spatial resolutions in all 3 directions were found to be independent of the MRD using AFORE and FBP. A comparison of the AFORE and FORE results for the transaxial resolutions is shown in *figure 2A*. Only the results for an MRD of 79 have been plotted, because both algorithms yielded negligible differences on variation of MRD. A comparison of the axial resolutions is shown in

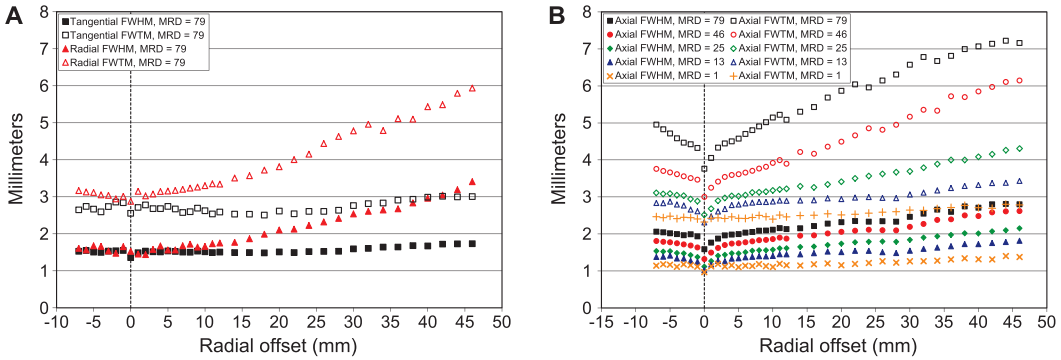

Figure 3a.1: (A) Transaxial spatial resolutions (FWHM and FWTM) obtained with FORE and FBP, using MRD of 79 as function of radial distance from CFOV. Other settings for MRD yielded highly similar results, which have been left out for clarity. (B) Axial spatial resolutions (FWHM and FWTM) obtained with FORE and FBP as function of radial distance from CFOV for different MRD settings.

Table 3a.2: Spatial resolution (FWHM) for CFOV and radial EFOV.

Method of measurement	CFOV*			Radial EFOV†		
	Tangential	Radial	Axial	Tangential	Radial	Axial
FORE, FBP						
MRD = 79	1.52 ± 0.02	1.57 ± 0.09	1.98 ± 0.04	1.70 ± 0.04	3.02 ± 0.26	2.75 ± 0.08
MRD = 46	1.52 ± 0.02	1.56 ± 0.09	1.72 ± 0.05	1.74 ± 0.04	2.99 ± 0.23	2.53 ± 0.09
MRD = 25	1.52 ± 0.02	1.54 ± 0.09	1.47 ± 0.04	1.74 ± 0.04	2.95 ± 0.17	2.06 ± 0.06
MRD = 13	1.51 ± 0.02	1.52 ± 0.08	1.32 ± 0.05	1.78 ± 0.04	2.95 ± 0.21	1.75 ± 0.05
MRD = 1	1.47 ± 0.02	1.51 ± 0.08	1.14 ± 0.03	1.83 ± 0.07	2.94 ± 0.20	1.51 ± 0.07
AFORE, FBP						
MRD = 79	1.50 ± 0.02	1.51 ± 0.08	1.30 ± 0.05	2.12 ± 0.07	2.80 ± 0.23	3.17 ± 0.40
OSEM3D/MAP						
β = 1.5 mm	1.69 ± 0.04	1.68 ± 0.02	1.71 ± 0.03	1.85	1.99	1.68
β = 0.5 mm	1.57 ± 0.04	1.56 ± 0.02	1.66 ± 0.02	1.70	1.82	1.62

* Values for CFOV for 2D reconstructions were obtained by averaging over 8 point source positions (2−5 mm from radial center). For OSEM3D/MAP, averaging was done for 2 positions (2 and 6 mm from radial center).
† Values for radial EFOV for 2D reconstructions were obtained by averaging over 6 point source positions (36–46 mm from radial center). For OSEM3D/MAP, value at 36 mm from radial center was taken.
Errors are SD belonging to averaging as indicated.

figure 2B. For AFORE, only the results for an MRD of 79 have been plotted because differences upon variation of MRD were negligible. However, the FORE results depended strongly on the MRD, as already shown in *figure 1A*. Therefore, as a typical example for smaller MRDs, the graph for FORE with an MRD of 13 is included in *figure 2B*. The averaged FWHMs for CFOV and EFOV obtained with AFORE are presented in *table 2*.

The radial profiles of FWHM and FWTM in all directions for OSEM3D/MAP for both MAP smoothing parameters (β = 0.5 and 1.5) are shown in *figures 3A* and *3B*. The numeric values of FWHM for CFOV and EFOV are given in *table 2*.

3a.3.2. Sensitivity

Figures 4A and *4B* show axial and radial profiles, respectively, of sensitivity using default ΔE and Δt for different MRDs. The axial profiles are for the radial center of the scanner; the radial profiles are for a middle plane. Point source positions were as indicated in the "Materials and Methods" section of this article.

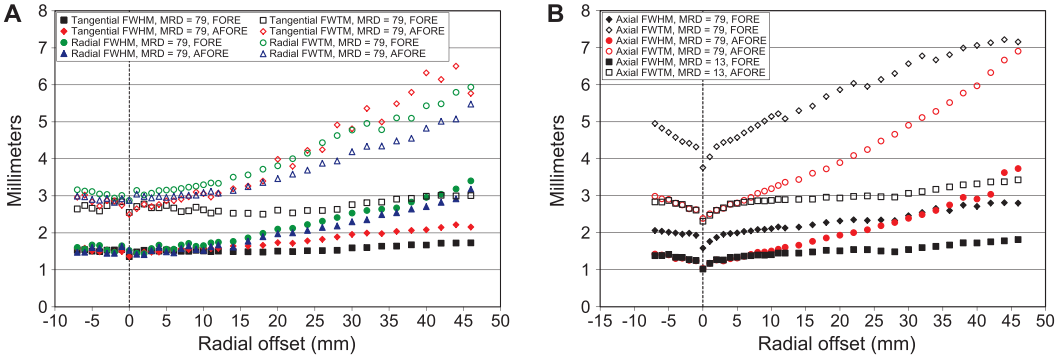

Figure 3a.2: (A) Comparison of transaxial spatial resolutions using FORE and AFORE, with FBP as function of radial distance from CFOV. Only results for MRD of 79 have been plotted, because both algorithms yielded negligible differences upon variation of MRD. (B) Comparison of axial spatial resolutions using FORE and AFORE as function of radial distance from CFOV. For AFORE, only results for MRD of 79 have been plotted, because differences upon variation of MRD were negligible. FORE results depended strongly on MRD. As example for small MRDs, FORE results with MRD of 13 are shown.

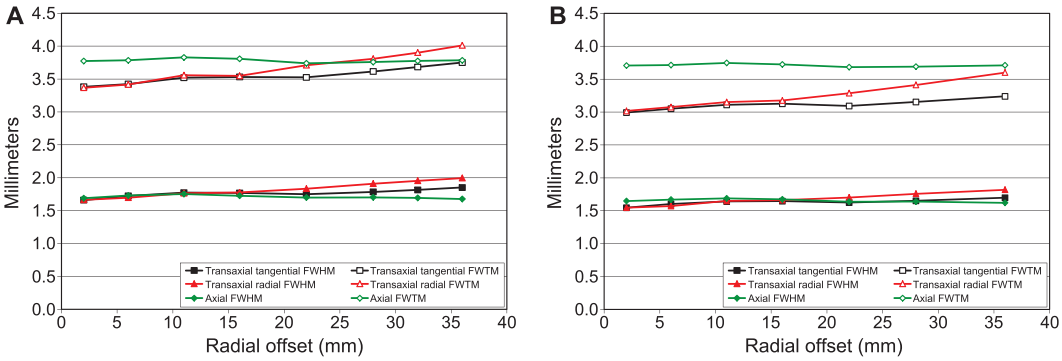

Figure 3a.3: Spatial resolution (FWHM and FWTM) in all directions as function of radial distance from CFOV for OSEM3D/MAP with β of 1.5 (A) and β of 0.5 (B).

Figure 4C shows the sensitivity obtained for the whole FOV for an MRD of 79 using the additional radial profiles separated by 10 mm in the axial direction. On the basis of cylinder symmetry, the original data were mirrored 2-fold to cover the complete FOV.

The effect of different ΔE and Δt settings on the sensitivity in the CFOV is shown in *table 3*. This table also shows the sensitivity as calculated from a total trues rate instead of from a histogrammed trues rate (numbers in parentheses). The corresponding spatial resolutions were found to be essentially independent of ΔE and Δt.

The images of the homogeneous ^{68}Ge cylinder that were used to compare the noise levels associated with FORE and AFORE are shown in *figure 5*. As an indication for image noise, we used the relative SD (SD_{rel} = SD divided by mean pixel value) in a central circular region of interest of 15-mm diameter, asshown in the figure. The resulting values for SD_{rel} were 0.10 and 0.22 for FORE and AFORE, respectively, indicating that FORE resulted in lower noise levels.

3a.4. Discussion

3a.4.1. Spatial Resolution

To compare spatial resolutions of different PET scanners, an agreement on rebinning and reconstruction algorithms has to be made. According to NEMA-NU2-2007 [9], the reconstruction method should be FBP. Although no prescription exists for the rebinning method, in most cases FORE is used, as was done in the present study.

In *figure 1A*, the deterioration of the transaxial radial resolution at the EFOV is clearly noticed. The transaxial tangential resolution, on the contrary, is more or less constant over the complete radial range of point source positions. We observed only a negligible dependency of both transaxial resolutions on MRD. These observations are in line with results for other (clinical and preclinical) PET scanners, for which the deterioration of the radial resolution has been attributed to the transaxial parallax or DOI effect [188].

As can be seen in *figure 1B* and *table 2*, axial resolution is markedly deteriorated for large MRDs. Both the axial parallax or DOI effect and the breakdown of FORE contribute to this deterioration. These effects are caused by large LOR acceptance angles, but whereas the breakdown of FORE is a mathematic phenomenon, the axial parallax or DOI effect is related to the way in which coincidence photons are being detected in the crystal elements. In general, these effects cannot be disentangled. However, for the radial CFOV, FORE is exact, and the larger FWHM should be attributed entirely to the axial parallax or DOI effect. In the CFOV for an MRD of 79,

axial FWHM is 1.98 mm, and by comparison with an MRD of 1, for which axial FWHM is 1.14 mm, it can be concluded that approximately 0.8 mm of increase of axial FWHM is caused by the parallax or DOI effect. For example, for the crystal size of 1.5 × 1.5 × 10 mm and a pitch of 1.59 mm, the absorption length will be distributed axially over 5 neighboring crystals when using a 10-mm crystal length as the typical length over which detected photons are absorbed, for photons with the maximum LOR acceptance angle of 38.3°. At the EFOV, also the breakdown of FORE adds to the deterioration of axial resolution, as shown by an axial FWHM of 2.75 mm for an MRD of 79.

For the smallest MRDs, the axial resolution is significantly better than the transaxial ones, both for the radial CFOV and for the EFOV. For an MRD of 1 (corresponding to a 2D mode operation of the scanner), we even found a submillimeter axial FWHM of 0.97 mm (*figure 1B*, value at exact CFOV). This FWHM value could be explained as follows. For LORs passing through the center of the FOV striking both detector elements perpendicularly, the theoretic FWHM—determined on the basis of only geometric arguments—equals d/2 (d = crystal size) if the point source is located midway between both detectors and approaches d when the source is close to 1 of the detectors [188]. However, because the crystal elements are arranged in blocks with flat faces, they are not located on an exact circle. LORs passing through the CFOV strike the outermost crystals of a detector block under an angle of approximately 5° with the normal in the transaxial direction. Therefore, a certain parallax or DOI effect will be present in transaxial directions, even if the point source is located at the exact CFOV. The axial resolution, on the contrary, is not influenced, because cylinder symmetry implies that axially, the photons strike all crystal elements perpendicularly provided MRD is small. Finally, the fact that we do not observe an axial FWHM of exactly d/2 = 0.75 mm may be attributed to a combination of many confounding effects: noncolinearity of the photon pairs, finite source dimension, finite positron range, geometric imperfections in the detector block array, or intracrystal scattering.

To fully exploit the high sensitivity of the Inveon, it is clear from *figure 4A* that an MRD of 79

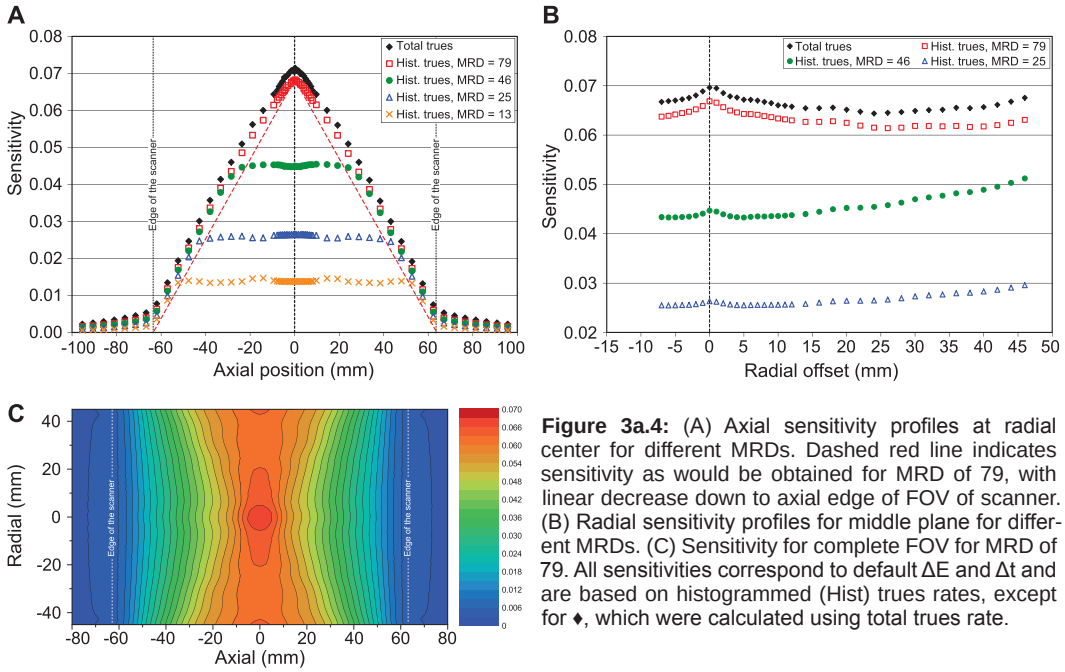

Figure 3a.4: (A) Axial sensitivity profiles at radial center for different MRDs. Dashed red line indicates sensitivity as would be obtained for MRD of 79, with linear decrease down to axial edge of FOV of scanner. (B) Radial sensitivity profiles for middle plane for different MRDs. (C) Sensitivity for complete FOV for MRD of 79. All sensitivities correspond to default ΔE and Δt and are based on histogrammed (Hist) trues rates, except for ♦, which were calculated using total trues rate.

Table 3a.3: Peak sensitivity for different energy and coincidence time windows for MRD of 79.

	Δt (ns)			
ΔE (keV)	2.8	3.4	4.1	4.7
350–650	0.068 (0.071)	0.068 (0.072)	0.068 (0.072)	0.068 (0.072)
250–750	0.099 (0.107)	0.100 (0.109)	0.101 (0.110)	0.101 (0.111)

Values belong to CFOV and are based on histogrammed trues rate. Numbers in parentheses are based on total trues rate.

should be used. However, it was demonstrated that for 2D reconstruction and FORE, a serious deterioration of axial resolution occurs. The AFORE algorithm overcomes this problem of deterioration to a certain extent. As can be seen in *figure 2B*, the axial resolution is indeed considerably improved for an MRD of 79 when using AFORE instead of FORE. However, for small MRDs there is no improvement, and in the EFOV axial resolution is even seriously deteriorated using AFORE, as can be seen in *figure 2B* in the comparison with FORE at an MRD of 13. Furthermore, although we expected that AFORE would not influence transaxial resolutions, *figure 2A* demonstrates that already for radial offsets greater than 15 mm, the tangential FWHM is larger for AFORE than it is for FORE. This effect is even stronger for FWTM, which is associated with highly nongaussian tangential profiles with extending tails for AFORE. Because no information is available on the mathematics used in AFORE, we presently cannot explain these phenomena. Finally, because AFORE results in lower effective sensitivity, as demonstrated by *figure 5* and the corresponding SD_{rel} values, we believe that AFORE is not the reconstruction method of choice for the Inveon.

For users who are not prohibited by the long reconstruction times of OSEM3D/MAP (4 h for 256 × 256 and 1 h for 128 × 128 image planes on the personal computer configuration, as mentioned in "Materials and Methods"), this reconstruction method is preferable in terms of uniform, high resolution and high sensitivity. As can be seen in *figures 3A* and *3B*, the spatial resolution is uniform across the FOV of the scanner and almost direction-independent, especially for FWMH. This result is explained by noting that OSEM3D/MAP is a fully 3D reconstruction technique without rebinning errors and that parallax or DOI effects in both the transaxial and the axial directions are suppressed because they have already been modeled in the P-matrices and blur kernels that are used in each iteration step of this reconstruction algorithm. Further, all LORs belonging to an MRD of 79 are being used, so maximum sensitivity is maintained. However, OSEM3D/MAP parameters still require optimization in terms of overall image quality (uniformity, recovery coefficients for small lesions, quantitative imaging, etc.). This optimization was outside the scope of the present study.

The spatial resolution of the Inveon based on FORE and FBP can be compared with that of the commercial crystal-based small-animal scanners given in *table 1*. For the F120, figures 1A and 1B of Kim *et al*. [192] demonstrate transaxial spatial resolutions similar to those for the Inveon. The same holds for the axial resolutions of an MRD of 46 (which is closest to the maximum MRD of 47 of the F120). The Mosaic (Philips) [193] is characterized by FWHMs ranging between 2.7 (radial, CFOV) and 5.8 mm (axial, EFOV; 46 mm from radial center), which are larger than the corresponding values for the Inveon. The Vista (GE Healthcare) has an FWHM of 1.4 mm for all directions in the CFOV. The tangential resolution is more or less independent of the radial offset, whereas both the axial and the radial FWHMs increase to approximately 2.4 mm for the radial EFOV at 29 mm (data estimated from figure 1A in Wang *et al*. [194]). The radial and tangential resolutions of the Vista are approximately equal to those of the Inveon. Axial resolution is better for the Vista than for the Inveon at an MRD of 79; however, for an MRD of 46 (which gives a better comparison with the smaller maximum LOR acceptance angle of 22.1° of the Vista), axial FWHMs are similar. For the ClearPET (Raytest) in the small–crystal ring configuration (diameter, 135 mm), FWHMs in all directions were reported as less than or equal to 1.3 mm in the

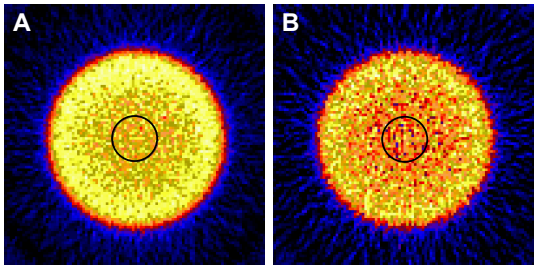

Figure 3a.5:
Comparison of reconstructed images of uniform ^{68}Ge cylinder with 6-cm diameter using FORE (A) and AFORE (B) for central transaxial plane. Reconstruction algorithm for both images was FBP with matrix size of 128 × 128. Color was scaled to maximum pixel value in both images. SD_{rel} was calculated for circular regions of interest. ROI = region of interest.

CFOV and less than or equal to 2.0 at a radial offset of 30 mm from the center [195]. These values are clearly better than those of the Inveon. However, unlike for the other scanners, the values have not been obtained using the NEMA prescriptions [9]. Instead of using rebinning and FBP, an iterative 3D reconstruction method (OSMAPOSL) was used, and resolutions were determined in Gaussian fits of the profiles instead of by using the NEMA interpolation method. On the other hand, when comparing the ClearPET OSMAPOSL results with the Inveon OSEM3D/MAP results, we found the ClearPET performance to be still better. It is not clear yet, though, to what extent this should be attributed to differences in the MAP-based reconstruction algorithms or to real differences in intrinsic spatial resolution between the scanners.

3a.4.2. Sensitivity

The peak sensitivity as specified by the manufacturer (>0.1) is confirmed by our value of 0.111. This value holds for the CFOV, large ΔE and Δt, and total trues rate instead of histogrammed trues rate. Sensitivity values for default ΔE are lower, as shown in *table 3*. The measured sensitivities are almost independentof Δt, indicating that the timing resolution is good for the counting rates observed with the present point source activity (prompt rates, 86.0 and 56.5 kcps for ΔE = 250–750 and 350–650 keV, respectively).

Because sensitivities were calculated using the rate at which photon pairs are emitted from the ^{22}Na point source, their accuracy is determined by the accuracy of the source activity (the influence of count statistics on the observed trues rate is negligible in view of the large number of coincidence counts in each measurement). This accuracy is ±4%, which leads to ±4% accuracy of all sensitivity values presented in this article. Our dose calibrators are regularly checked by the manufacturer using sources (provided by North American Scientific Inc.) that have been calibrated against the standards at The Netherlands Metrology Institute (Nederlands Meetinstituut) and the German Federal Metrology Institute (Physikalisch-Technische Bundesanstalt). However, the activity, as specified on the ^{22}Na point source calibration data sheet of the IPL, is 7% smaller than the value measured by us. Accordingly, when using this value, we would have increased all sensitivity data by 7%. However, we preferred to use the value measured by us because the accuracy specified by IPL is as large as ±15%.

The axial sensitivity profiles in *figure 4A* are in accordance with straightforward geometric considerations based on the total number of LORs contained in the FOV of the scanner when the point source is stepped in the axial direction. This explains the central plateaus for an MRD of less than 79 and the more or less linear drop to zero when moving the point source toward the axial EFOVs. It is not immediately clear why the observed drop in sensitivity is less than predicted by mere geometry, but the following could be speculated. For a point source in the CFOV, the maximum angle at which coincidences are detected is 38.3°, whereas for positions closer to the axial edges, this angle decreases. Oblique photons may be less effectively detected by crystals at the edge of detector blocks because of the gaps between blocks, which could explain the observed less-than-linear drop of sensitivity. Coincidences are detected even when the point source is lo-

cated beyond the EFOVs. This effect should be attributed mostly to scatter effects in the detector crystals or in the lead ring that shields the detectors at the axial EFOVs and to a lesser extent to the natural radioactivity of LSO crystals because of the presence of ^{176}Lu. The background contribution just outside the FOV at 71 mm from the center was 6%.

Sensitivity across the whole FOV as shown in *figure 4C* may be illustrative for researchers who wish to optimize their experiments by scanning more than 1 animal at the same time. On the basis of only sensitivity, it would be preferable to place 2 animals (e.g., mice) on top of or next to each other instead of behind each other. However, it should be verified whether attenuation and scatter correction is still effective, because more attenuating and scattering mass will then be present in the transaxial FOV.

It is interesting to compare the sensitivity of the Inveon with its predecessor, the F120, which has the same crystal size and similar geometry but fewer crystal rings. A sensitivity of 0.040 was found for an ΔE of 350–650 keV (table 2 in Kim *et al*. [192]) for the maximum MRD of 47. The closest attainable MRD in the Inveon is 46, for which we found a sensitivity of 0.0451 (average plateau value in *figure 4A*). It is therefore concluded that the higher sensitivity of the Inveon is due not only to its larger axial FOV but also, for approximately 13%, to its better detection efficiency for each crystal ring separately. In fact, the difference is still somewhat larger, because the data of Kim *et al*. [192] were based on total trues rate (written communication with J.S. Lee, second author of reference [192], 2008), whereas we used histogrammed trues rate in our study.

The Inveon showed higher sensitivity than did the other commercial small-animal scanners presented in *table 1*. The values reported in the literature for these scanners cannot directly be compared with those of the Inveon, mainly because of the use of different energy windows, but they are summarized here. The peak sensitivity of the Mosaic for an ΔE of 410–665 keV is 0.0114 [193]. The Vista is characterized by peak sensitivities of 0.065, 0.040, and 0.021 for energy windows of 100–700, 250–700, and 400–700 keV, respectively [194]. Finally, the reported peak sensitivity for the ClearPET is 0.045 [195,196] for the small-diameter, full-ring configuration with an ΔE of 250–750 keV.

3a.5. Conclusion

The Inveon small-animal PET scanner is characterized by high spatial resolution and high sensitivity. However, when using rebinning and 2D reconstruction, a trade-off occurs between these 2 parameters. Axial spatial resolution is deteriorated by both the axial parallax or DOI effect and the breakdown of FORE for large LOR acceptance angles. The way to retain both high sensitivity and high spatial resolution in all directions is by using fully 3D image reconstruction algorithms such as OSEM3D/MAP, which form part of the standard scanner software.

Although the spatial resolution performance of the Inveon is similar to that of scanners such as the F120 or the Vista (results for the ClearPET cannot properly be compared because of different methodology), the peak sensitivity of 0.111, obtained with an ΔE of 250–750 keV, is presently unrivaled.

3b. Spatial Resolution of the Inveon Small-Animal PET Scanner for the Entire Field of View

Jonathan A. Disselhorst[1], Otto C. Boerman[1], Wim J.G. Oyen[1], Cornelius H. Slump[2] and Eric P. Visser[1]

[1] Department of Nuclear Medicine, Radboud University Nijmegen Medical Centre, Nijmegen, The Netherlands

[2] Institute of Technical Medicine, University of Twente, Enschede, The Netherlands

Reprinted from Nucl Instrum Meth A. 2010;615:245-248, with permission from Elsevier.

Abstract

In high throughput small-animal positron emission tomography (PET) studies, it can be advantageous to scan more than one animal at the same time. To optimally position these animals in the scanner, both sensitivity and spatial resolution have to be known across the entire field of view (FOV). The Siemens Inveon small-animal PET scanner has been characterized according to NEMA NU 4-2008 standards, but the spatial resolution has only been determined in a small portion of the FOV and only for filtered backprojection (FBP). In this study, the spatial resolution in the entire FOV was determined for the Inveon using FBP, ordered subset expectation maximization in 2 dimensions (OSEM2D) and maximum a posteriori (MAP) reconstructions. OSEM2D produced the best spatial resolution in the axial center of the FOV, but MAP outperformed the two other reconstruction algorithms in terms of uniformity of the resolution.

3b.1. Introduction

The Inveon (Siemens Medical Solutions, Knoxville TN, USA) small-animal positron emission tomograph (PET) has been characterized in several studies [162-165]. In some of these studies the NEMA (NEMA NU-4 2008, [10]) characterization standards were used. Visser et al. [163] and Constantinescu *et al.* [165] determined transaxial spatial resolution for the axial center of the scanner. Bao *et al.* [162] and Kemp *et al.* [164] extended these measurements to profiles taken at an offset one quarter of the axial length from the center. Visser *et al.* used maximum a posteriori (MAP) reconstructions next to the NEMA-specified filtered backprojection (FBP).

In high throughput small-animal PET studies where several mice are scanned simultaneously, information about the spatial resolution and sensitivity across the entire field of view (FOV) is helpful to optimally position the animals in the scanner. With its relatively large axial length, the Inveon is especially well equipped for multi-animal studies. Typically, up to four mice can be scanned simultaneously in different configurations.

For FBP and other 2 dimensional (2D) reconstruction algorithms, dept-of-interaction (DOI) effects for photons with oblique incidence angles relative to the detector face, seriously deteriorate the spatial resolution in off-axis positions. It is therefore desirable to use 3 dimensional (3D) statistical reconstruction algorithms that should provide a more uniform spatial resolution. Both axial and transaxial blurring are suppressed during reconstruction because the point spread functions (PSFs) throughout the FOV are being used in the projection matrix during reconstruction by the ordered subset expectation maximization in 3 dimensions (OSEM3D) and MAP algorithms.

In this study we extended the standard NEMA protocol and determined spatial resolution in tangential and radial directions for the full FOV, for three different reconstruction algorithms.

3b.2. Materials and methods

3b.2.1. Data acquisition and image reconstruction

Spatial resolution of the Inveon was measured using a ^{22}Na point source with an active diameter of less than 0.25 mm embedded in a Lucite disk (Isotope Products Laboratories, Berlin, Germany). The activity of the point source was 0.92 MBq, as measured in a dose calibrator (VDC-404; Veenstra, Joure, The Netherlands).

Spatial resolution measurements were not corrected for source dimension, positron range, or non-colinearity of the 2 photons involved in positron annihilation. The point source was placed in the FOV of the scanner for transaxial positions ranging from 0 to 44 mm and for axial positions ranging from 0 to 52 mm from the center. Ninety-two point source positions were scanned, 10 million coincidence counts were collected during each scan.

The coincidence timing window and the energy window were used at their default settings of 3.4 ns and 350-650 keV, respectively. A delayed-window technique was used for randoms subtraction. Dead-time correction was based on a global singles-rate estimate.

For all point source locations, the listmode data were histogrammed into 3D sinograms using the default span = 3, and maximum ring difference = 79. The sinograms were reconstructed using FBP (Fourier rebinning, 256 × 256 × 159 matrix size, 0.39 × 0.39 × 0.80 mm^3 pixel size, ramp filter with cutoff at Nyquist frequency), ordered subset expectation maximization in 2 dimensions (OSEM2D; Fourier rebinning, 256 × 256 × 159 matrix size, 0.39 × 0.39 × 0.80 mm^3 pixel size, 4 iterations) and ordered subset expectation maximization in 3 dimensions followed by MAP reconstruction (OSEM3D/MAP; 256 × 256 × 159 matrix size, 0.43 × 0.43 × 0.80 mm^3 pixel size, 2 OSEM3D iterations, 18 MAP iterations, $\beta = 0.1$ optimized for uniform resolution). This

reconstruction will be referred to as MAP from now on. Although larger matrices with smaller pixel sizes can be chosen for FBP and OSEM2D, this is not possible for MAP reconstructions, because of the limited number of pMatrices provided by the manufacturer. For a proper comparison, we therefore chose 256 × 256 × 159 matrices for all reconstruction algorithms. Histogramming and reconstruction was performed with Inveon Acquisition Workplace (IAW; version 1.2.2.2)

3b.2.2. Analysis

All spatial resolution measurements were performed in MATLAB (R2008a, The MathWorks, Inc, Natick, MA, USA). To determine the full width at half maximum (FWHM) and full width at tenth maximum (FWTM), the position of the maximum pixel was determined. Radial and tangential transaxial profiles through this position were created by summing all one-dimensional profiles parallel to the specific direction within about two times the expected FWHM. In these profiles, the maximum was determined from a parabolic fit though the maximum pixel and its two nearest neighbors. Linear interpolation between two adjacent pixels at half and one-tenth of this maximum determined FWHM and FWTM.

The axial pixel size is not influenced by matrix size selection and has a fixed value of 0.80 mm (half the crystal pitch). Giving that the axial FWHM is less than 2 mm, the axial resolution cannot be determined reliably in a direct manner. By moving the point source stepwise in axial direction with steps smaller than the slice separation, an oversampled axial profile could have been obtained, allowing determination of the axial resolution. This method, however, has not been used in this study and only transaxial resolutions are given.

3b.3. Results

Table 1 shows the minimum and maximum values of the FWHM and FWTM for the three reconstruction algorithms.

MAP has the most uniform spatial resolution with FWHM in tangential direction between 1.29 and 1.47 mm, and a FWHM in radial direction between 1.30 and 1.88 mm. OSEM2D has an overall smaller FWHM tangentially. In the radial direction, the FWHM for OSEM2D is only smaller than MAP in the transaxial center.

Figure 1A and *1B* shows the FWHM in the radial and tangential directions for the three reconstruction algorithms. The horizontal axes show the position of the point source in radial direction, the vertical axes show the FWHM. The thickness of the lines shows the variation in FWHM in axial direction. The difference between the three reconstruction algorithms are quite large, especially at the edges of the transaxial field of view. The most striking outcome of this image is the small variation in the MAP results, both in transaxial and axial direction, and both for tangential and radial FWHM. Especially FBP causes large variation in FWHM in the radial direction.

The results are similar for the FWTM's, as shown in *figure 1C* and *1D*: a relatively uniform distribution for MAP, and large variance in especially the radial FWTM for the other reconstruction algorithms. Again, OSEM2D produced the lowest values in the tangential

Table 3b.1: Minimum and maximum FWHM and FWTM for three reconstruction algorithms.

	Tangential FWHM (mm)		Radial FWHM (mm)		Tangential FWTM (mm)		Radial FWTM (mm)	
	Minimum	Maximum	Minimum	Maximum	Minimum	Maximum	Minimum	Maximum
MAP	1.29	1.47	1.30	1.88	2.33	2.78	2.37	3.67
OSEM2D	1.03	1.44	0.99	2.76	1.89	2.64	2.16	5.26
FBP	1.45	1.83	1.51	2.99	2.51	3.44	3.30	5.80

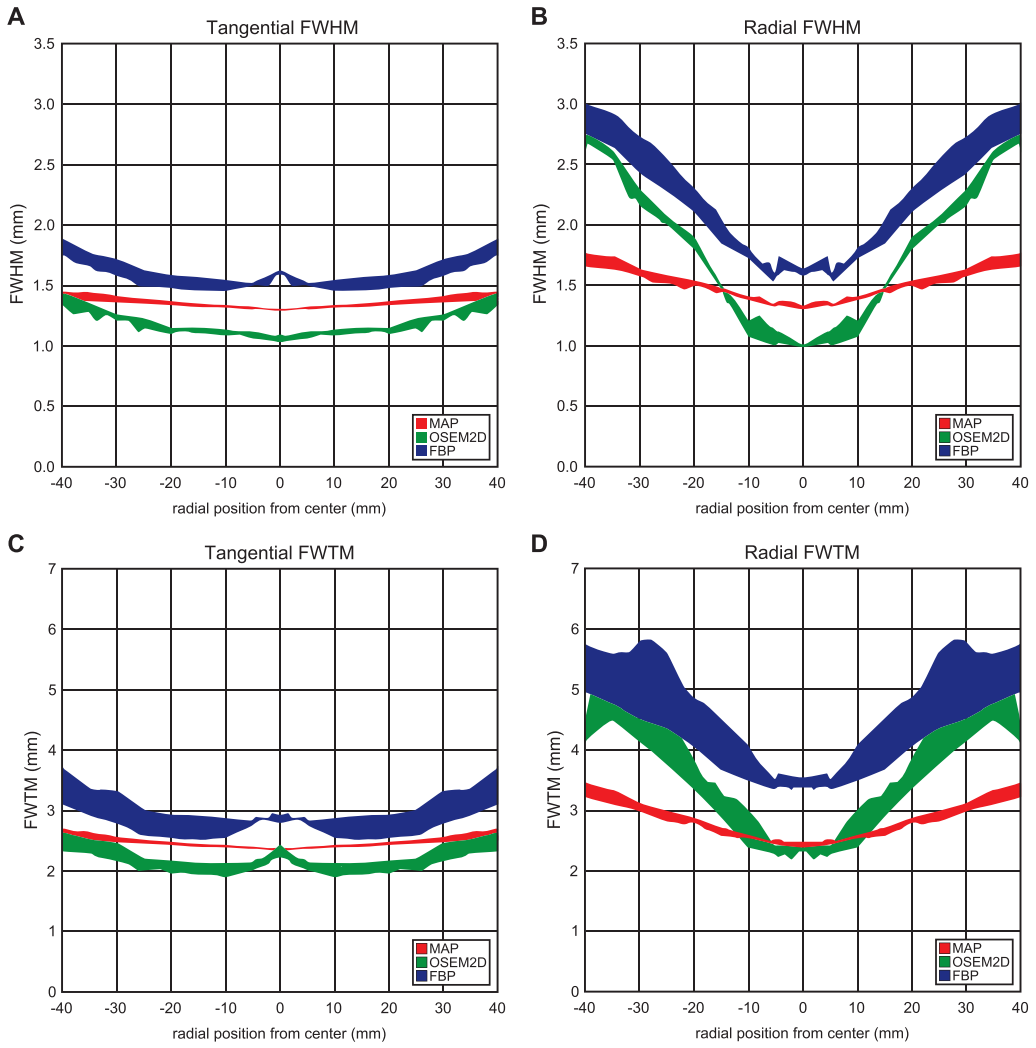

Figure 3b.1: FWHM (A and B) and FWTM (C and D) of the Inveon for FBP, OSEM2D and MAP as a function of radial position. The thickness of the lines represents the variation in axial direction.

direction, but only for the center of the FOV in radial direction.

With these data, one could determine the optimal positioning of the mice in the scanner when multiple (2–4) mice have to be scanned simultaneously. The FWHMs acquired with MAP are presented in *figure 2*. Apart from the spatial resolution, also the distribution of sensitivity should be taken into account. The sensitivity of the Inveon across the FOV has been determined earlier [163].

3b.4. Discussion and conclusion

The present study shows that with MAP reconstruction, the most uniform distribution of spatial resolution can be obtained. OSEM2D performs slightly better in the center of the FOV, but causes a large increase at the edges of the FOV. FBP has no advantages with respect to spatial resolution.

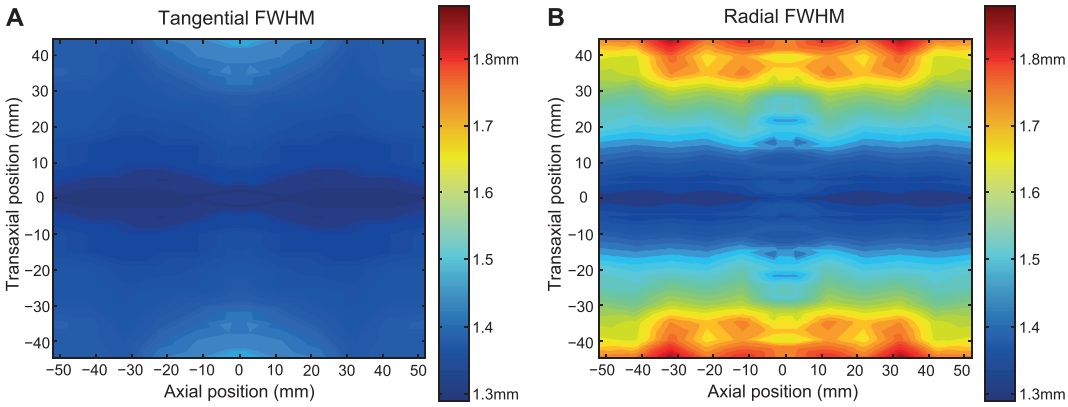

Figure 3b.2: Interpolated sensitivity and tangential (A) and radial (B) FWHM profiles for MAP.

Since MAP results in relatively small variations in spatial resolution across the FOV, the positions with the highest sensitivity should be used for imaging and mice may be placed besides each other, or on top of each other rather than behind each other. However, further studies should be carried out to determine differences in photon attenuation and scatter depending on the positioning of the animals.

Although MAP produces images with a more uniform spatial resolution, reconstruction takes much longer than for FBP or OSEM2D. A typical MAP reconstruction, as used in this study, takes about 2:45 h on a Windows XP 64bit PC with an Intel Xeon E5430 CPU running at 2.66 GHz as opposed to about 30 s for OSEM2D and 5 s for FBP. A faster implementation of the MAP algorithm (FastMAP, [197]) is available, which takes about 15 min for reconstruction, but results in a loss of resolution near the edges of the FOV and has therefore not been considered in this study.

4. Characterization and Optimization of Image Quality as a Function of Reconstruction Algorithms and Parameter Settings in a Siemens Inveon Small-Animal PET Scanner Using the NEMA NU 4-2008 Standards

Eric P. Visser[1], Jonathan A. Disselhorst[1], Monique G.J.T.B. van Lier[1,2], Peter Laverman[1], Gabie M. de Jong[1], Wim J.G. Oyen[1] and Otto C. Boerman[1]

[1] Department of Nuclear Medicine, Radboud University Nijmegen Medical Centre, Nijmegen, The Netherlands

[2] Institute of Technical Medicine, University of Twente, Enschede, The Netherlands

Reprinted from Nucl Instrum Meth A. 2011;629:357-367, with permission from Elsevier.

Abstract

The image reconstruction algorithms provided with the Siemens Inveon small-animal PET scanner are filtered backprojection (FBP), 3-dimensional reprojection (3DRP), ordered subset expectation maximization in 2 or 3 dimensions (OSEM2D/3D) and maximum a posteriori (MAP) reconstruction. This study aimed at optimizing the reconstruction parameter settings with regard to image quality (IQ) as defined by the NEMA NU 4-2008 standards. The NEMA NU 4-2008 image quality phantom was used to determine image noise, expressed as percentage standard deviation in the uniform phantom region (%SD), activity recovery coefficients for the ^{18}F-FDG-filled rods (RC), and spill-over ratios for the non-radioactive water- and air-filled phantom compartments (SOR_{wat} and SOR_{air}). Although not required by NEMA NU 4, we also determined a contrast-to-noise ratio for each rod (CNR), expressing the trade-off between activity recovery and image noise. For FBP and 3DRP the cut-off frequency of the applied filters, and for OSEM2D and OSEM3D, the number of iterations was varied. For MAP, the "smoothing parameter" β and the type of uniformity constraint (variance or resolution) were varied. Results of these analyses were demonstrated in images of an ^{18}F-FDG-injected rat showing tumors in the liver, and of a mouse injected with an ^{18}F-labeled peptide, showing a small subcutaneous tumor and the cortex structure of the kidneys. Optimum IQ in terms of CNR for the small-diameter rods was obtained using MAP with uniform variance and $\beta = 0.4$. This setting led to $RC_{1mm} = 0.21$, $RC_{2mm} = 0.57$, %SD = 1.38, $SOR_{wat} = 0.0011$, and $SOR_{air} = 0.00086$. However, the highest activity recovery for the smallest rods with still very small %SD was obtained using $\beta = 0.075$, for which these IQ parameters were 0.31, 0.74, 2.67, 0.0041, and 0.0030, respectively. The different settings of reconstruction parameters were clearly reflected in the rat and mouse images as the trade-off between the recovery of small structures (blood vessels, small tumors, kidney cortex structure) and image noise in homogeneous body parts (healthy liver background). Highest IQ for the Inveon PET scanner was obtained using MAP reconstruction with uniform variance. The setting of β depended on the specific imaging goals.

4.1. Introduction

Characterization of the performance of small-animal positron emission tomography (PET) scanners has for a long time been hampered by the absence of exact standards. For that reason, several investigators used the NEMA NU 2-2007 [9] or NU 2-2001 [161] standards for clinical PET scanners with adaptations to account for the smaller dimensions of small-animal scanners [164,192,193,198]. Whereas the definitions of spatial resolution, sensitivity and count rate performance could be adapted in a more or less straightforward manner, this was less appropriate for image quality (IQ) due to the absence of a dedicated phantom and the definition of the appropriate IQ parameters. IQ should be measured in a phantom that produces images simulating those obtained in a total body study of a small rodent with hot lesions, as well as uniform hot and some cold areas. However, a straightforward reduction in size of the NEMA NU 2 clinical IQ phantom is not feasible due to physical limitations in producing hot spheres in non-zero background with physical walls much smaller than the spatial resolution of the PET scanner. For qualitative, visual analysis of IQ in small-animal PET, typically Derenzo phantoms with hot or cold rods have been used [164,165,192-194,196,198].

For quantitative measurement of exactly defined IQ parameters, the NEMA NU 4-2008 [10] image quality (NU4IQ) phantom was designed. This phantom contains fillable rods of different diameters in cold solid background. The activity recovery coefficients measured in these hot rods are indicative of the spatial resolution of the scanner. The noise in the uniform region of the phantom is indicative of the signal-to-noise ratio performance, while the uniformity in this region is a measure of the attenuation and scatter correction performance. The activity measured in non-radioactive water- and air-filled compartments is indicative of the scatter correction performance.

To our knowledge, three papers exist in which the NU4IQ phantom was used to characterize IQ in a small-animal PET scanner. Bao *et al.* [162] presented IQ parameters for a Siemens Inveon using FBP with default image reconstruction setting. Bahri *et al.* [199] characterized the MicroPET Focus 120, with emphasis on different methods of attenuation correction (^{57}Co singles and ^{68}Ge positron transmission sources). Lage *et al.* [200] presented the results obtained for their experimental PET/CT scanner based on coplanar detector geometry and a partial ring PET system (VrPET/CT).

The reconstruction software included with the Inveon PET scanner (Inveon Acquisition Workplace, IAW version 1.2) allows for as many as 5 different reconstruction algorithms with several adjustable parameters without specific recommendations. The present study aimed at optimizing IQ for the Inveon PET scanner as a function of these algorithms and parameter settings using the NU4IQ phantom.

In real animal experiments, it is often complicated or even impossible to give exact definitions of optimum IQ. In the trade-off between, e.g., high spatial resolution and corresponding high activity recovery for small lesions versus image noise, different researchers may arrive at different parameter settings depending on study purpose, practical limitations, or personal preference. Whereas "smoothed" images may ease qualitative interpretation, a too high degree of smoothing could conceal small metastases. Quantification of radiopharmaceutical uptake by, e.g., standard uptake values has been shown to be highly dependent on image reconstruction settings [201]. In clinical PET, this was one of the issues leading to the definition of the Netherlands PET acquisition standard [202] to facilitate quantitative multicenter PET studies. In the present study, we evaluated the impact of reconstruction algorithm and parameter settings on quantification, which could influence the comparability of results obtained by different institutions or different types of small-animal PET scanners.

Finally, we will demonstrate some of the NU4IQ phantom results in two animal experiments.

4.2. Materials and methods

4.2.1. NU4IQ phantom and IQ parameters

The NU4IQ phantom is composed of a main phantom body, which contains a fillable cylindrical chamber with 30 mm diameter and 30 mm length, and a solid part of 20 mm length in which 5 fillable rods have been drilled through with diameters of 1, 2, 3, 4, and 5 mm. It further consists of a lid that attaches to the uniform region of the phantom and supports two cold region chambers. These regions are hollow cylinders 15 mm in length and 8 mm inner diameter with 1 mm wall thickness, and should be filled with non-radioactive water and air. The phantom was constructed according to the NEMA NU 4 specifications by Agile Engineering (Knoxville, TN, USA).

According to NEMA NU 4, the phantom was filled with an ^{18}F-FDG solution with a total activity of 3.7 MBq at the start time of the acquisition. Given the total phantom volume of 20.66 mL, this resulted in an activity concentration of 179.1 kBq/mL.

The following NEMA NU 4 IQ parameters were determined: (i) image noise, expressed as the percentage standard deviation (%SD) in a central, cylindrical volume of interest over the centre of the uniform region of the phantom, (ii) activity recovery coefficients for the filled rods (RC), expressed as the measured activity concentration in the rods divided by the mean phantom concentration, and (iii) spill-over ratios for the non-radioactive water- and air-filled compartments (SOR_{wat} and SOR_{air}), defined as the activity concentration measured in these compartments divided by the mean phantom concentration. Exact definitions and phantom locations where these parameters were determined have been described elsewhere [10].

Although not prescribed by NEMA NU 4, a contrast-to-noise ratio (defined as CNR=100×RC/%SD) was determined as it was considered a useful parameter to evaluate the trade-off between spatial resolution and activity recovery in small structures versus image noise. This additional parameter was determined for the 2 smallest rods (1 and 2 mm diameter) for all reconstruction settings.

4.2.2. Acquisition, histogramming and reconstruction settings

Images were recorded on an Inveon PET scanner using the default energy and coincidence timing windows of 350–650 keV and 3.432 ns, respectively. The hardware configuration of this scanner has been described elsewhere [162-165,203].

A 20 min emission scan was recorded in list mode and histogrammed into a 3-dimensional (3D) sinogram of 128 rows and 160 angles with a span of 3 and maximum ring difference of 79, resulting in a 3D sinogram containing 53 segments. For the purpose of attenuation correction, a transmission scan of 20 min was recorded after the emission scan using the built-in ^{57}Co source of 131 MBq with energy window of 120–125 keV. As NEMA NU 4 does not specify the duration of the transmission scan, it was decided to use the same duration as the emission scan leading to a total scan duration of 40 min, which was considered as "reasonable" in most animal experiments.

Component-based normalization with a scan duration of 10 h was used. As reported previously [203], this normalization does not contribute to image noise.

The reconstruction algorithms used were 2-dimensional (2D) filtered backprojection (FBP), 3D reprojection (3DRP), 2D and 3D ordered subset expectation maximization (OSEM2D and OSEM3D, respectively) and 3D maximum a posteriori (MAP) reconstruction. A description of MAP reconstruction for small-animal PET can be found elsewhere [166]. Although the IAW software offers the possibility of using "fastMAP", which speeds up the reconstruction by about a factor of 4, we preferred to use the standard MAP algorithm, since fastMAP showed several unexpected features. Fourier rebinning was used for the 2D reconstruction algorithms (FBP and

OSEM2D). Reconstructions have been performed with and without scatter correction. The implemented scatter correction algorithm is based on direct calculation from analytical formulas and source and object geometry [204]. Transaxial image matrix size was 256 × 256 in all cases with pixel size of 0.388 mm for FBP, 3DRP and OSEM2D, and 0.431 mm for OSEM3D and MAP. In view of the intrinsic spatial resolution of ±1.5 mm [163], this pixel size is in accordance with the Nyquist sampling criterion. The number of axial planes was 159 with plane thickness and separation of 0.796 mm.

For FBP, several types of filters can be selected. A straightforward ramp filter was used with variation of f_{ramp} between 0.1 and 0.5, where 0.5 corresponds to the Nyquist frequency. For 3DRP, only the Hann filter is available, of which the window cut-off frequency f_{Hann} was varied between 0.1 and 0.5.

Whereas for the analytical reconstruction algorithms FBP and 3DRP a spatial frequency based filter can be varied, in OSEM2D and OSEM3D, the number of iterations can be chosen (the number of subsets is fixed at 16). For both algorithms, the number of iterations was varied between 1 and 16.

MAP reconstruction allows for the choice of uniform variance or resolution, the value of the prior expressed as the "smoothing" parameter β, and the number of iterations. In this study, the influence of β and the uniformity conditions on IQ were first analyzed, while keeping the number of iterations fixed at the default value of 18. For the parameter settings that gave highest RC for the smallest diameter rods and low values for %SD and SOR, the influence of the number of MAP iterations was separately investigated. All MAP reconstructions were preceded by 2 OSEM3D iterations. Since OSEM3D converges faster than MAP, this resulted in quick estimates of the intermediate images at the start of the MAP iterations. In this paper, when MAP reconstruction is mentioned, MAP was always preceded by 2 OSEM3D iterations.

4.2.3. Variation of transmission scan duration

Attenuation correction increases image noise due to the finite number of counts in the transmission scan. As NEMA NU 4 does not specify the duration of the transmission scan, additional scans of 5, 10 and 300 min were recorded. The shorter scans of 5 and 10 min duration served to investigate as to what extent transmission scans may be shortened without substantial increase of image noise, and the (extremely) long scan of 300 min was made to obtain a virtually "noiseless" attenuation correction. The influence of these different transmission scan durations on IQ was investigated for the reconstruction setting that was found to give highest RC and small %SD, which is MAP with uniform variance and $\beta = 0.075$.

4.2.4. Animal studies

In a WAG/Rij rat liver tumors were induced by intrahepatic injection of syngeneic rat colon carcinoma cell line CC531. A PET scan of 15 min was performed 1 h after injection of 10 MBq ^{18}F-FDG. For anatomical reference, a CT scan was performed immediately after the PET scan using the Inveon CT scanner [205] in docked configuration with the PET scanner. The CT parameters were 80 kV, 500 μA, 360° rotation in 180 steps, and 300 ms exposure time per step. The image was obtained using 2 bed positions with 20% overlap. An Al beam filter of 0.5 mm thickness was used.

A BALB/c nude mouse with a subcutaneous CEA-expressing tumor was injected with unlabeled TF2, an anti-CEA×anti-HSG bispecific antibody [206]. After pretargeting of the tumor with TF2, 5 MBq of a ^{18}F-labeled HSG containing peptide was injected and a 30-min PET scan was performed 2 h after injection.

For both scans, PET images were obtained using MAP reconstruction with uniform variance

and β = 0.075, the settings that gave highest RC for small rods (highest spatial resolution) and for β = 0.4, which gave highest CNR (optimum trade-off between spatial resolution and image noise).

4.3. Results

4.3.1. FBP reconstructions

IQ parameters for FBP with f_{ramp} between 0.2 and 0.5 are shown in *figure 1*. Although images were also obtained using f_{ramp} = 0.1 and 0.15, their visual quality was very poor and resulted in SOR_{wat} and SOR_{air} values<0. Therefore, reconstructions with f_{ramp} < 0.2 were not considered further. RC is shown in *figure 1A*. Since scatter correction had only minor influence on RC, values obtained with scatter correction are shown for the 1 mm diameter rod only, for which the differences were largest. *Figure 1B* shows %SD and CNR for the 1 and 2 mm diameter rods with and without scatter correction. Highest values of CNR were found for f_{ramp} in the order of 0.25–0.30, or typically half the Nyquist frequency. Applying scatter correction slightly increased %SD. As a combined result of CNR becoming somewhat smaller and %SD somewhat larger, CNR clearly decreased by using scatter correction. *Figure 1C* shows SOR_{wat} and SOR_{air} for reconstruction without and with scatter correction, demonstrating that scatter correction considerably decreased SOR.

4.3.2. 3DRP reconstructions

Figure 2 shows IQ parameters for 3DRP with f_{Hann} between 0.1 and 0.5. RC is shown in *figure 2A*. Again, scatter correction had only minor impact on RC; values obtained with scatter correction are shown for the 1 mm diameter rod only. *Figure 2B* shows %SD and CNR for the 1

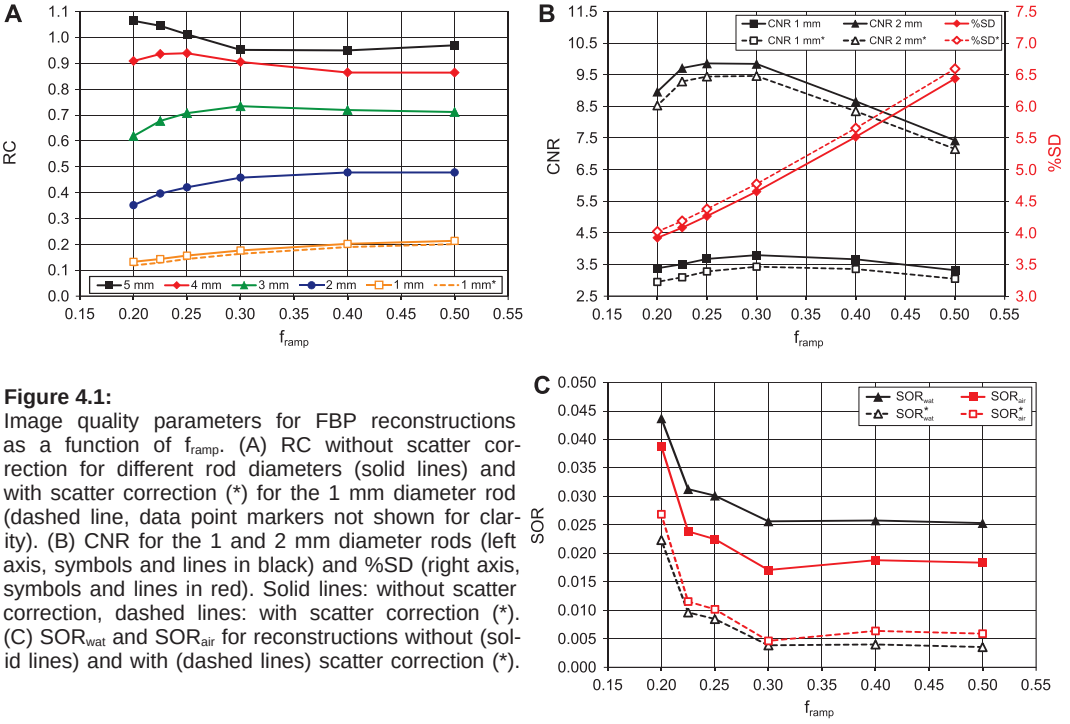

Figure 4.1:
Image quality parameters for FBP reconstructions as a function of f_{ramp}. (A) RC without scatter correction for different rod diameters (solid lines) and with scatter correction (*) for the 1 mm diameter rod (dashed line, data point markers not shown for clarity). (B) CNR for the 1 and 2 mm diameter rods (left axis, symbols and lines in black) and %SD (right axis, symbols and lines in red). Solid lines: without scatter correction, dashed lines: with scatter correction (*). (C) SOR_{wat} and SOR_{air} for reconstructions without (solid lines) and with (dashed lines) scatter correction (*).

and 2 mm diameter rods with and without scatter correction. As for the FBP-reconstructed images, scatter correction slightly increased %SD. Combined with a slight decrease of RC, scatter correction resulted in smaller values for CNR. Highest values of CNR were found for f_{Hann} in the order of 0.2–0.3, or typically half of the Nyquist frequency. *Figure 2C* shows SOR_{wat} and SOR_{air} as a function of f_{Hann} for reconstruction without and with scatter correction, indicating that scatter correction considerably decreased SOR.

4.3.3. OSEM2D reconstructions

Figure 3 shows IQ parameters for OSEM2D as a function of the number of iterations. RC is shown in *figure 3A*. Except for the 1 mm diameter rod, RC only weakly depended on the number of iterations. RC_{1mm}, however, started to drop considerably when the number of iterations became smaller than 4. As opposed to FBP and 3DRP, OSEM2D slightly increased RC when using scatter correction. *Figure 3B* displays %SD and CNR for the 1 and 2 mm diameter rods. Relatively large values for CNR were obtained when lowering the number of iterations (except for CNR for 1 mm in the case of only 1 iteration). This was not related to changes in RC but to the strong decrease of %SD for lower numbers of iterations. Scatter correction had only a small influence on both %SD and CNR. *Figure 3C* shows SOR_{wat} and SOR_{air} as a function of the number of iterations for reconstruction without and with scatter correction. SOR increased when lowering the number of iterations.

4.3.4. OSEM3D reconstructions

OSEM3D reconstructions resulted in "Gibbs-like oscillations" or "Gibss overshoots" [166,171] at the edges of the 5 mm diameter rod. *Figure 4* shows line profiles through the centre of this rod using 4 (default) and 16 iterations, indicating that the effect becomes more prominent for increased numbers of iterations. Since these overshoots result in relative depressions in the

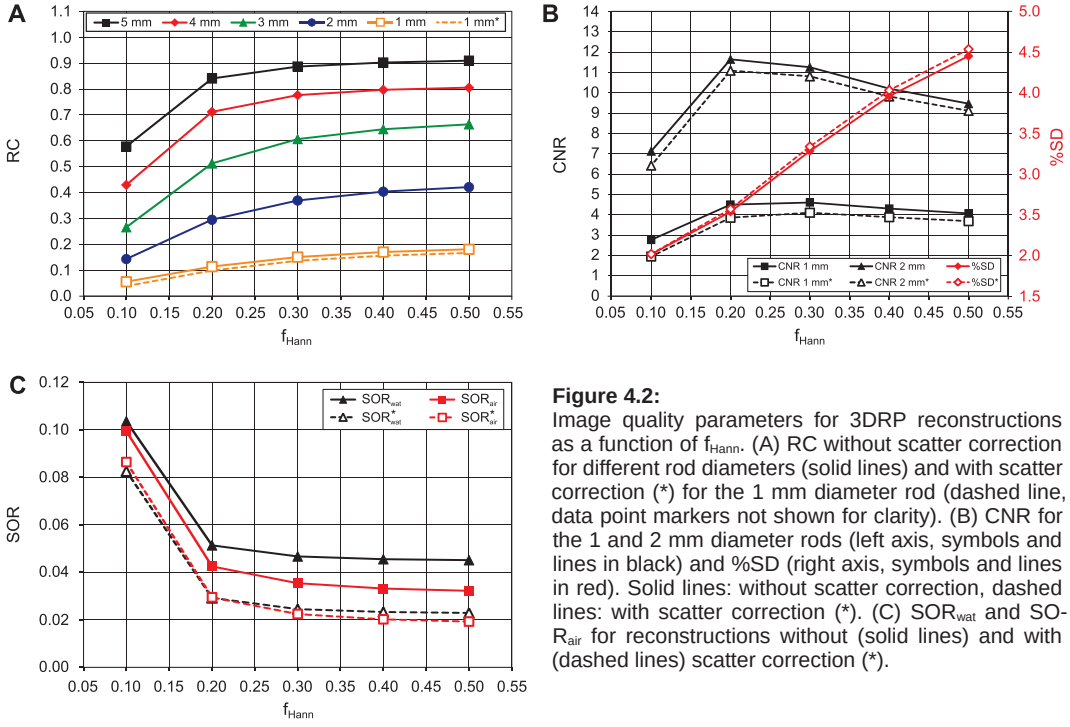

Figure 4.2:
Image quality parameters for 3DRP reconstructions as a function of f_{Hann}. (A) RC without scatter correction for different rod diameters (solid lines) and with scatter correction (*) for the 1 mm diameter rod (dashed line, data point markers not shown for clarity). (B) CNR for the 1 and 2 mm diameter rods (left axis, symbols and lines in black) and %SD (right axis, symbols and lines in red). Solid lines: without scatter correction, dashed lines: with scatter correction (*). (C) SOR_{wat} and SOR_{air} for reconstructions without (solid lines) and with (dashed lines) scatter correction (*).

centre of the active region, the presence of this artifact was considered unacceptable, especially for oncology studies as it could be misinterpreted as necrosis in the centre of a tumor.

Only by decreasing the number of iterations down to 2 or 1, the artifact disappeared. However, for these small numbers of iterations, SOR values increased considerably (0.10 and 0.16 for 2 and 1 iterations, respectively, with almost no difference between the water and air compartments) whereas RC_{1mm} became very small (0.12 and 0.07 for 2 and 1 iterations, respectively). These results make OSEM3D reconstructions with 1 or 2 iterations unattractive in terms of IQ. Since the "depression" artifact disappeared in MAP reconstructions by adjustment of β, while at the same time good IQ parameters were retained (see next section), a full characterization of the OSEM3D results is not reported (full OSEM3D IQ data set available in electronic form on request).

4.3.5. MAP reconstructions

For MAP reconstructions, the same "depression" artifact as for OSEM3D was found when β was chosen too small. In the same way as for OSEM3D, the presence of this artifact was considered unacceptable, and accordingly, reconstruction settings leading to this artifact were not considered further. Values of β below which the artifact occurs ($β_{min}$) depended on the type of uniformity constraint. Uniform variance led to $β_{min} \approx 0.075$, and uniform resolution was characterized by $β_{min} \approx 0.2$.

Figure 5 shows the IQ parameter for MAP reconstructions as a function of β for uniform resolution and uniform variance. RC is shown in *figure 5A*. Decreasing β ("amount of smoothing") clearly resulted in higher RC, especially for the small-diameter rods. The results obtained using scatter correction were highly similar and have not been included in the graph. *Figure 5B* shows CNR for the 1 and 2 mm diameter rods, and %SD. Again, scatter correction had almost no influence (results not plotted). Uniform variance led to much smaller %SD than uniform resolution, and increasing β decreased %SD. *Figure 5C* shows SOR_{wat} and SOR_{air} as a function of β for uni-

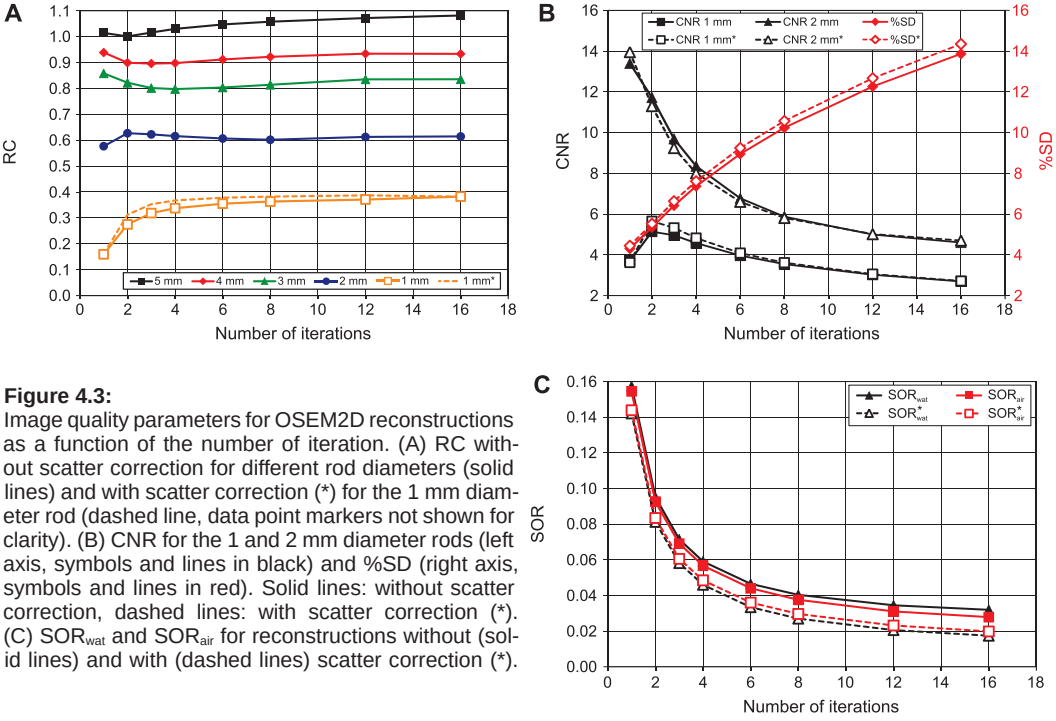

Figure 4.3:
Image quality parameters for OSEM2D reconstructions as a function of the number of iteration. (A) RC without scatter correction for different rod diameters (solid lines) and with scatter correction (*) for the 1 mm diameter rod (dashed line, data point markers not shown for clarity). (B) CNR for the 1 and 2 mm diameter rods (left axis, symbols and lines in black) and %SD (right axis, symbols and lines in red). Solid lines: without scatter correction, dashed lines: with scatter correction (*). (C) SOR_{wat} and SOR_{air} for reconstructions without (solid lines) and with (dashed lines) scatter correction (*).

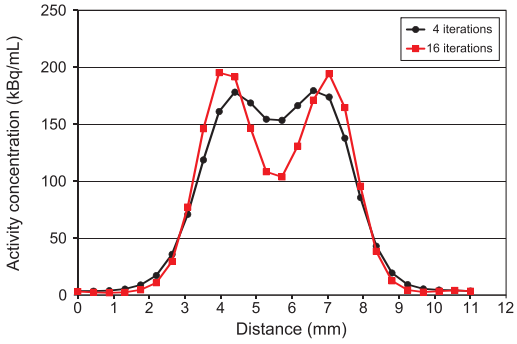

Figure 4.4:
Line profiles through the centre of the 5 mm diameter rod for OSEM3D reconstruction using 4 and 16 iterations.

form resolution and uniform variance. For most settings, SOR_{wat} and SOR_{air} were extremely small as compared to those for FBP, 3DRP and OSEM2D. The highest value in the range investigated was $SOR_{wat} = 0.0041$, occurring for $\beta=1.0$ and uniform resolution. Unexpectedly, however, for $0.1 \leq \beta \leq 0.3$ using uniform variance, SOR values were much larger, although still in the same order of magnitude as for the previously presented reconstruction algorithms.

The effect of scatter correction on SOR_{wat} and SOR_{air} was not always favorable. In some cases, e.g., for uniform resolution with $\beta = 0.1$ and 0.2 (see *figure 5C*), SOR_{air} was increased by using scatter correction, although the values remained extremely small (0.0031 and 0.0034, respectively). However, the larger SOR values for $0.1 \leq \beta \leq 0.3$ using uniform variance were clearly reduced by factors of 2–3 when using scatter correction.

4.3.6. Influence of the number of MAP iterations on IQ parameters

Following from the preceding sections, highest RC for the small rods, small %SD, small SOR and no "depression" artifacts were obtained using MAP reconstruction with uniform vari-

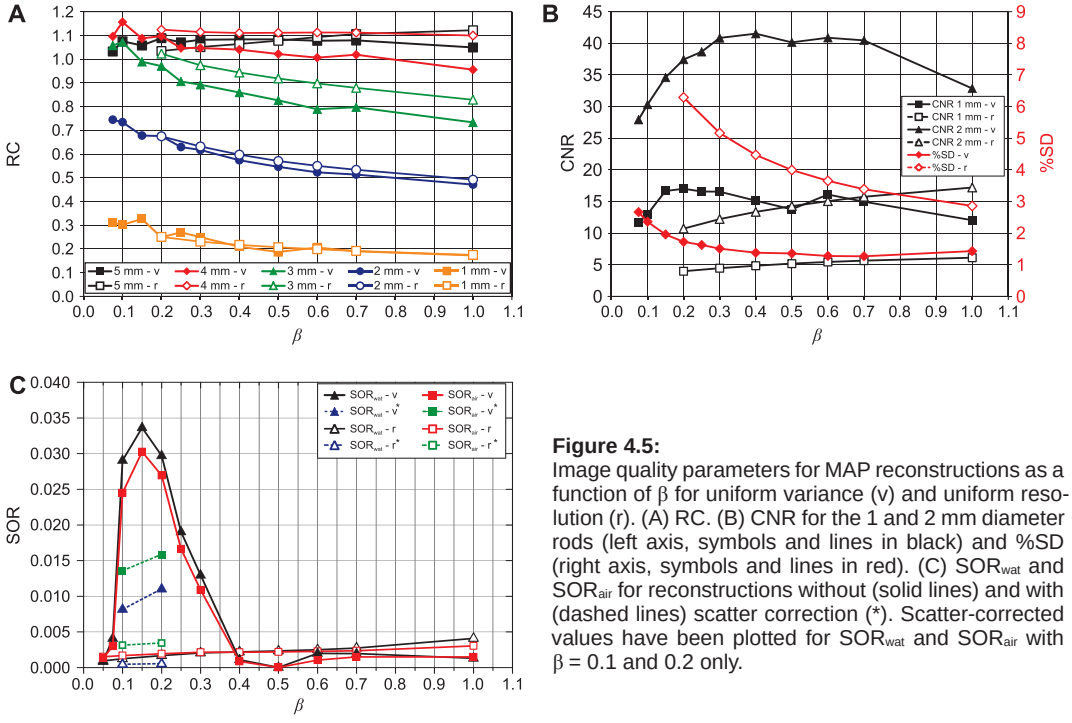

Figure 4.5:
Image quality parameters for MAP reconstructions as a function of β for uniform variance (v) and uniform resolution (r). (A) RC. (B) CNR for the 1 and 2 mm diameter rods (left axis, symbols and lines in black) and %SD (right axis, symbols and lines in red). (C) SOR_{wat} and SOR_{air} for reconstructions without (solid lines) and with (dashed lines) scatter correction (*). Scatter-corrected values have been plotted for SOR_{wat} and SOR_{air} with $\beta = 0.1$ and 0.2 only.

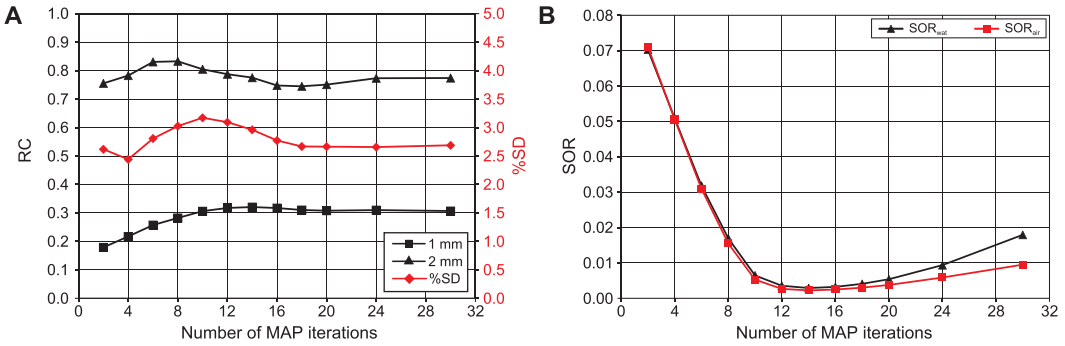

Figure 4.6: Image quality parameters for MAP reconstructions as a function of the number of MAP iterations for β = 0.075 and uniform variance without scatter correction. (A) RC for the 1 and 2 mm diameter rods (left axis, symbols and lines in black) and %SD (right axis, symbols and lines in red). (B) SOR_{wat} and SOR_{air}.

ance and β = 0.075. For this more or less "optimum" setting, additional reconstructions were performed with the number of MAP iterations varying between 2 and 30. The resulting IQ parameters are presented in *figure 6*. Optimum activity recovery for the smallest diameter rod and suppression of spill-over was not yet achieved for small numbers of MAP iterations. Fourteen MAP iterations were needed to obtain highest RC_{1mm} and smallest SOR_{wat} and SOR_{air}. However, in order to also minimize %SD, 18 iterations were necessary. Although this slightly increased SOR_{wat} and SOR_{air} these parameters remained very small (0.004 and 0.003, respectively).

4.3.7. Variation of transmission scan duration

Figure 7 shows RC for the 1 and 2 mm diameter rods and %SD for MAP reconstruction with uniform variance and β = 0.075 as a function of the duration of the transmission scan. Shortening the transmission scan from 20 to 5 min increased %SD (from 2.67 to 3.17) and RC_{1mm} (from 0.31 to 0.34), whereas RC_{2mm} was hardly affected. The long transmission scan of 300 min decreased both RC_{1mm} and RC_{2mm} (from 0.31 to 0.28, and from 0.74 to 0.69, respectively), whereas %SD remained almost unaffected.

4.3.8. Animal results

Figure 8 shows transverse ^{18}F-FDG PET and CT cross-sections of the tumor bearing rat. It is apparent that β = 0.4 (*figure 8B*) yielded a smoother image than the one obtained for β = 0.075 (*figure 8A*), especially for the liver background. However, when comparing the small tumors and blood vessels in both images, it is seen that β = 0.075 provided a more detailed structure than β = 0.4.

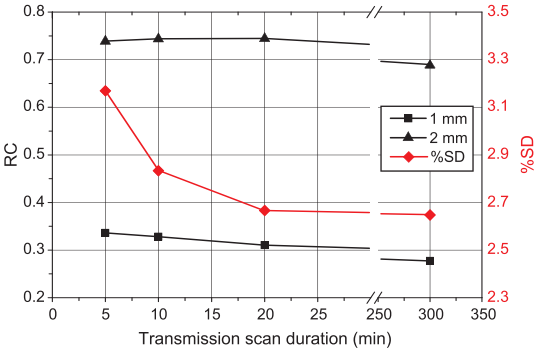

Figure 4.7:
RC for the 1 and 2 mm diameter rods (left axis, symbols and lines in black) and %SD (right axis, symbols and lines in red) for MAP reconstruction with uniform variance and β = 0.075 as a function of the duration of the transmission scan. Scatter correction was not applied.

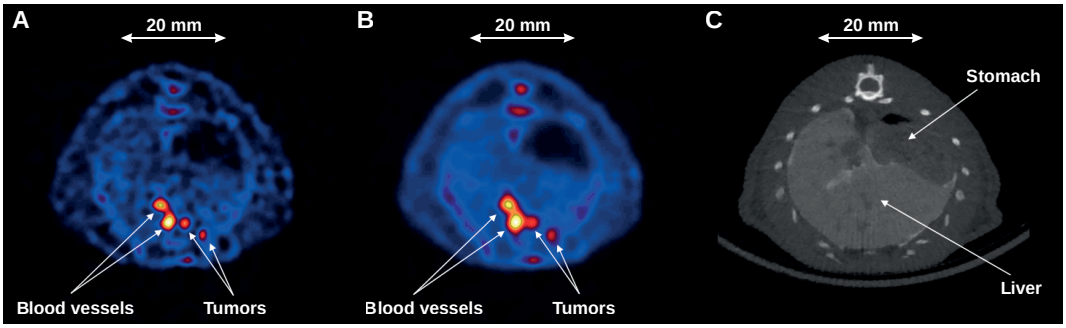

Figure 4.8: Transverse cross-sections through the liver of a tumor bearing rat injected with 10 MBq ^{18}F-FDG. (A) PET image recorded 1 h after injection, reconstructed using MAP with $\beta = 0.075$ and uniform variance. (B) Same image slice and reconstruction as in (A) but reconstructed with $\beta = 0.4$. Color scales have been chosen equal for (A) and (B). (C) CT image recorded immediately after the PET scan.

A different situation exists when noise in background regions is not an issue. This is e.g., the case for the CEA-expressing tumor-bearing mouse, injected with an ^{18}F-labeled peptide after pretargeting as demonstrated in *figure 9*, showing coronal cross-sections of the PET images through the kidneys and tumor. Thanks to the efficacy of pretargeting, there is almost no uptake in background tissues. In this case, one would prefer the highest spatial resolution, resulting in high activity recovery and detection of very small metastases or other small structures. Clearly, $\beta = 0.075$ (*figure 9A*) better fulfilled this requirement than did $\beta = 0.4$ (*figure 9B*), as is also demonstrated by the line profile of *figure 9C*.

4.3.9. Reconstruction times

Table 1 shows the reconstruction times for the available algorithms using the default numbers of iterations for matrices of 256 × 256 pixels on a Windows XP 64 bit PC with an Intel Xeon E5430 CPU running at 2.66 GHz.

The complete set of NEMA NU 4 parameters, including mean, minimum and maximum activity concentrations for the uniform region and the rods, and the standard deviations of RC, SOR_{wat}, and SOR_{air} is available in electronic form on request.

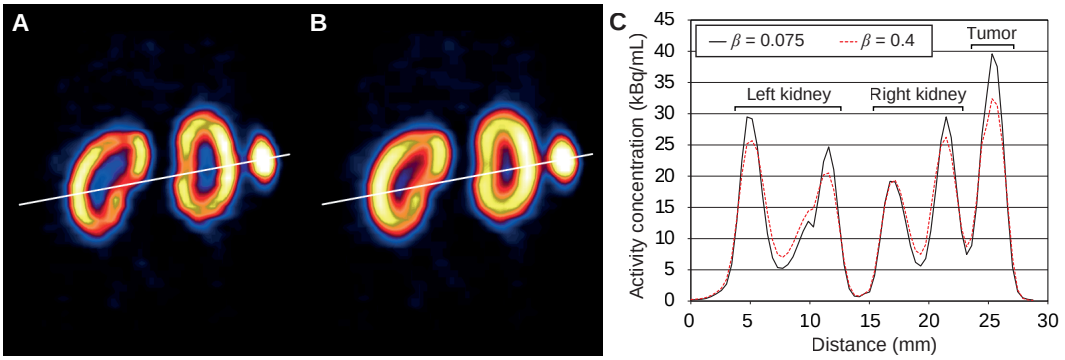

Figure 4.9: Coronal cross-sections through kidneys and tumour of a mouse injected with 5 MBq of a ^{18}F-labeled peptide, scanned 2 h after injection. (A) PET image reconstructed using MAP with $\beta = 0.075$ and uniform variance. (B) Same image slice and reconstruction as in (A) but reconstructed with $\beta = 0.4$. Colour scales have been chosen equal for (A) and (B). (C) Line profiles of activity concentration through kidneys and tumour as indicated by white line in (A) and (B).

4.4. Discussion

For each reconstruction algorithm, one could try to define the optimum parameter settings, that is, the settings that maximize RC (especially for the smallest rods) and minimize %SD, SOR_{wat}, and SOR_{air}. However, these IQ parameters cannot be optimized independently. For the analytical algorithms FBP and 3DRP, increasing the filter frequency increases RC and decreases SOR_{wat} and SOR_{air} (which is desirable), but increases %SD (which is undesirable) and vice versa.

The same holds true for OSEM2D when increasing the number of iterations. Especially %SD becomes very large for large numbers of iterations. On the other hand, many iterations are necessary to obtain small SOR_{wat} and SOR_{air}. Even for 16 iterations, these spill-over ratios are still larger than those for FBP, and are in the same order of magnitude as for 3DRP (with scatter correction applied). Apparently, cold regions in hot environments can only be recovered using enough iterations, as has previously been described for OSEM2D in a clinical scanner [91].

MAP reconstructions are characterized by small %SD, very small SOR_{wat} and SOR_{air}, and still relatively large RC. However, the exact values strongly depend on the "smoothing parameter" β and the uniformity condition. It was found that uniform variance results in much smaller %SD (typically by a factor of 2–3) than uniform resolution, whereas RC for the small rods is virtually the same (see *figure 5A* and *5B*). It is not clear, however, as to why this uniformity condition so strongly affects %SD.

The unexpected relatively high SOR values occurring only for $0.1 \leq \beta \leq 0.3$ using uniform variance (and not using uniform resolution for the whole range of β investigated) remain unexplained. This could be considered as a feature of the MAP reconstruction software, which might be dealt with in upcoming versions of IAW.

As mentioned before, there is no "one-fits-all" reconstruction setting that optimizes all IQ parameters at the same time. However, considering that an optimum trade-off between spatial resolution (activity recovery for small structures) and image noise is generally desirable, an overview of the IQ parameters for reconstruction settings that yielded highest CNR for the 1 mm diameter rod is presented in *table 2*. This allows for a direct comparison of the performance of the different reconstruction algorithms with regard to IQ. It should be noted that OSEM3D has been left out because of the above mentioned "depression" artifact. MAP reconstruction with uniform variance and $\beta = 0.4$ gives optimum IQ in terms of CNR (*table 2*). However, as has been shown by the rat and mouse scans in *figure 8* and *9*, one may not always wish to define IQ in terms of CNR. Since MAP reconstructions are characterized by low noise levels, larger RC could be preferred at the cost of some increase in %SD. In that case, $\beta = 0.075$ with uniform variance would be more "optimal". For completeness, the resulting IQ parameters for this setting have been included in *table 2*.

As expected, scatter correction decreased SOR_{wat} and SOR_{air} for FBP, 3DRP and OSEM2D, and only slightly changed the other IQ parameters. It is therefore desirable to use scatter correction with these algorithms. However, for MAP reconstructions, SOR is already extremely small without scatter correction, and using scatter correction is not always beneficial. We therefore feel that scatter correction should not be applied in MAP reconstructions. Finally, it is worth mentioning that in small-animal PET, photon scatter is less of a problem than in clinical PET. Whereas

Reconstruction algorithm	Default number of iterations	Reconstruction time
FBP	–	0:00:05
3DRP	–	0:55:00
OSEM2D	4	0:00:20
OSEM3D	4	0:54:00
OSEM3D/MAP	2/18	2:36:00

Table 4.1:
Reconstruction times on a Windows XP 64 bit PC with an Intel Xeon E5430 CPU running at 2.66 GHz.

the highest SOR values in the present study were ±0.09 (OSEM2D with only 2 iterations), they are typically more than 2 times higher in clinical scanners using the NEMA NU 2 IQ phantom. Kemp *et al.* [207] reported values of ±20% for the "residual error in the lung insert" (which, in percentage, is the NEMA NU 2 parameter comparable with SOR) for a modern General Electric PET/CT scanner using both OSEM2D and OSEM3D reconstruction.

One of the drawbacks of MAP reconstructions could be the long reconstruction time of 2 h and 36 min using the type of personal computer of this study. However, in view of the much better IQ provided by MAP reconstructions, this is considered as a minor drawback, especially since the IAW reconstruction software can be used on more than one computer for simultaneous reconstructions of different scans, also overnight. MAP reconstructions can be performed somewhat faster by decreasing the default number of 18 iterations. As shown in *figure 6*, high RC_{1mm} and small SOR_{wat} and SOR_{air} are already obtained using ±12 MAP iterations, although %SD is still somewhat larger (3.09 as opposed to 2.67 obtained using 18 iterations). This would result in a reconstruction time of 2 h and 13 min. However, if reconstruction time remains an issue, or if "preview" images are required before carrying out the final MAP reconstructions, FBP or OSEM2D can be used to obtain reconstructed images almost immediately after finishing the PET scan. Given the long reconstruction time of 55 min and no definite improvement of IQ, 3DRP is not recommended.

Total scan time can be decreased by shortening the ^{57}Co transmission scan. As shown in *figure 7*, decreasing the transmission scan duration to 5 min hardly deteriorates IQ using MAP with uniform variance and $\beta = 0.075$. The same was found for other MAP settings (data not shown). On the other hand, transmission scans longer than 20 min will not considerably improve IQ. Please note that our parameters hold for the ^{57}Co single source activity of 131 MBq (nominally 185 MBq at the time of shipment).

As mentioned before, Bao *et al.* [162] have used the NU4IQ phantom to characterize the Inveon PET scanner. Their measurements, however, were part of a general NEMA NU 4 characterization not aiming at a comparison or optimization of different reconstruction algorithms and settings with regard to IQ. Using FBP with $f_{ramp} = 0.5$ and all corrections applied, the resulting RC (0.17, 0.48, 0.72, 0.84, and 0.93 for 1, 2, 3, 4, and 5 mm diameter, respectively) were almost equal to the ones in the present study (0.20, 0.47, 0.71, 0.87, and 0.97). %SD of 5.29 was smaller than our value of 6.59. Their values for SOR_{wat} and SOR_{air} were 0.0165 and 0.0057, respectively, whereas in the present study these were 0.0036 and 0.0059. The results of Bao *et al.* are not exactly comparable to those of the present study. Instead of the total phantom activity of 3.7 MBq as recommended by NEMA NU 4, they used 5.1 MBq. This could explain their lower %SD, resulting

Table 4.2: Reconstruction parameters yielding maximum CNR for the 1 mm diameter rod.

Reconstruction algorithm	Settings		Scatter correction	CNR	RC	%STD	SOR_{wat}	SOR_{air}
FBP	$f_{ramp} = 0.3$		No	3.80	0.177	4.65	0.0256	0.0171
			Yes	3.43	0.164	4.77	0.0039	0.0046
3DRP	$f_{Hann} = 0.3$		No	4.61	0.151	3.28	0.0467	0.0354
			Yes	4.10	0.137	3.34	0.0245	0.0225
OSEM2D	2 iterations		No	5.14	0.275	5.35	0.0952	0.0927
			Yes	5.66	0.312	5.53	0.0813	0.0835
OSEM3D/MAP	Uniform variance, 18 MAP iterations	$\beta = 0.4$ *	No	15.13	0.209	1.38	0.0011	0.0009
		$\beta = 0.075$ †	No	11.64	0.310	2.67	0.0041	0.0030

* This setting yielded maximum CNR for the 2 mm diameter rod. Largest CNR for the 1 mm diameter rod (17.0) was obtained for $\beta = 0.2$. However, as explained in the text, this setting was considered unacceptable in view of the corresponding unexpectedly high SOR values.
† This setting yielded maximum RC for the 1 mm diameter rod.

from better count statistics. Further, attenuation correction in their study was performed using CT as opposed to rotating ^{57}Co source transmission. Since scatter correction essentially uses information from the transmission scan [204], this could possibly explain the differences in SOR values of both studies.

4.5. Conclusion

A wide range of reconstruction algorithms and parameter setting is available for the Inveon PET scanner. In this study, optimum settings have been determined in terms of IQ parameters as defined by NEMA NU 4 using the dedicated phantom. The NEMA NU 4 IQ parameters can be used in future standardization of quantitative small-animal PET experiments in, e.g., multicenter studies, and for comparison of different types of scanners.

5. Optimal Framing in Dynamic ^{18}F-FDG PET

Jonathan A. Disselhorst[1], Dennis Vriens[1], Thomas G. Wright[2], Lioe-Fee de Geus-Oei[1], Wim J.G. Oyen[1], Cornelis H. Slump[3] and Eric P. Visser[1]

[1] Department of Nuclear Medicine, Radboud University Nijmegen Medical Centre, Nijmegen, The Netherlands

[2] Siemens Molecular Imaging, Oxford, United Kingdom

[3] Institute of Technical Medicine, University of Twente, Enschede, The Netherlands

Submitted

Abstract

Dynamic positron emission tomography (PET) using ^{18}F-fluorodeoxyglucose (FDG) is being used to determine the microparameters of glucose kinetics in tumours by using pharmacokinetic models. The estimated values of these microparameters, however, are greatly affected by the method the dynamic acquisition is divided into time frames ("framing"). The purpose of this study was to determine the influence of framing on these microparameters and to find a framing schedule that produces the most accurate parameter values. Because there are no means to find the true values for these parameters in vivo, optimization was performed using simulations in silico.

Methods. Arterial plasma time activity curves, and tissue time activity curves were simulated and different framing schedules were applied. Frame duration and activity-concentration specific noise of the Siemens Biograph Duo was added in order to simulate realistic measured PET signals. All simulated curves were processed with a pharmacokinetic modelling toolbox using non-linear least squares curve fitting. The estimated microparameter values were compared to the input microparameters. The optimal framing schedules were tested and compared using clinical dynamic PET data acquired in listmode.

Results. Clinical dynamic ^{18}F-FDG PET data reconstructed with different framing schedules showed a large difference in estimated microparameters. Only the influx constant (K_i) was unaffected by the framing. The simulations clearly showed the trade-off between noise and temporal resolution. For the most accurate results, the minimal frame duration should be 4 or 5 seconds, and at least a total number of 40 frames is required for a dynamic scan of 60 min with a 40-s infusion of ^{18}F-FDG.

Conclusion. The influence of the framing schedule on the observed tumour microparameters is large. An optimal framing schedule can be obtained to improve the accuracy of estimation.

5.1. Introduction

Positron emission tomography (PET) images can be analyzed quantitatively, that is, images provide absolute activity concentrations of the radiopharmaceutical used. Visual assessment and quantitative methods such as the standardized uptake value (SUV) are often used to describe the biodistribution of the radiopharmaceutical [208]. For some applications, such as therapy response monitoring, more detailed quantification methods may be required. One such method is pharmacokinetic modelling assuming an underlying compartment model, which requires dynamic PET acquisition [188].

PET has the ability to acquire images dynamically, allowing measurements of the concentration of radiopharmaceuticals in volumes of interest (VOIs) over time. Typically, the PET acquisition is divided into multiple independent time frames, which are then analyzed using for instance non-linear regression. However, there is a specific requirement for this method: to be able to observe the rapid changes in activity concentration, especially shortly after injection of the radiopharmaceutical, the time frames should be of sufficiently short duration to provide the required temporal resolution. Normally, PET reconstruction algorithms only make use of the emission data from one single time frame, i.e., each frame is reconstructed in an individual image, which can have high noise levels due to the low amount of counts per unit volume (voxel) per time frame; non-linear regression methods are especially sensitive to noise. Images with less noise can be obtained by increasing the administered activity, by increasing the frame duration or increasing voxel volume. The latter two come at the cost of lower temporal or spatial resolution, respectively. Therefore, a trade-off is expected between temporal resolution and noise related to the choice of frame-durations ("framing"). In the literature, there is no consensus in this area, and most research groups use their own framing schedules. The fastest activity concentration shifts are observed in the first minutes after injection of the radiopharmaceutical. During this time the characteristic "blood peak" is observed, for which sufficient temporal resolution is required. In literature frame durations ranging between 5 and 30 s are used in the initial phase of the scan. In this study we aimed at optimizing the framing in dynamic ^{18}F-fluorodeoxyglucose (FDG) PET studies to obtain the most accurate microparameters in a two-tissue compartment model of ^{18}F-FDG-kinetics. A schematic representation of the two-tissue compartment model is given in *figure 1*.

5.2. Materials and methods

In this study, tissue and arterial plasma time activity curves ($C_t^{sim}(t)$ and $C_p^{sim}(t)$, respectively) were simulated to optimize the framing schedule for dynamic PET scanning. A schematic overview of the different steps in the simulation is shown in *figure 2* and details about each individual step are given below. Simulated curves were generated and analyzed in MATLAB (version R2008a; The MathWorks, Inc; Natick (MA), USA). Different framing schedules were evaluated and the optimal framing schedule was applied to the data of fifteen patients with non small-cell lung carcinoma (NSCLC) who underwent a dynamic ^{18}F-FDG PET scan acquired in listmode (LM) in an ongoing study.

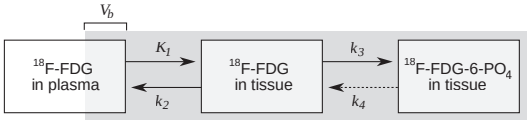

Figure 5.1: The two-tissue compartment ^{18}F-FDG model with pharmacokinetic rate constants K_1, k_2, k_3, and k_4. In this study the irreversible variant of the model was used, where k_4 is assumed to be zero. The measured PET signal (shown as a gray box) is a combination of ^{18}F-FDG in tissue and a fraction of blood plasma, V_b.

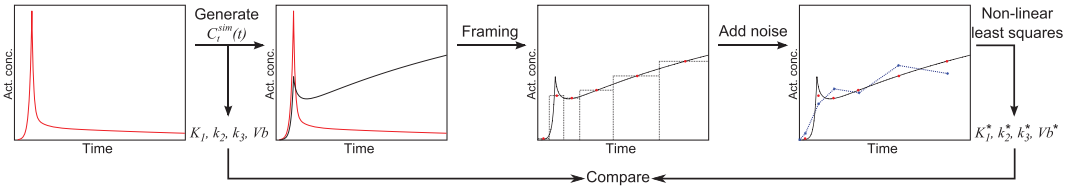

Figure 5.2: Flowchart indicating the different steps in the simulation in simplified form. First, an $C_p^{sim}(t)$ curve is generated (depicted in red), then random tumour microparameters are generated and a $C_t^{sim}(t)$ curve is computed (depicted in black). Both curves are framed (only shown for $C_t^{sim}(t)$) and then random noise based on the PET scanner's characteristics is added (shown in blue) dependent on frame duration and activity concentration. Finally, both curves are processed to obtain the tumour microparameters. The input and output parameters are compared.

5.2.1. Patient population

Newly diagnosed patients with NSCLC of at least 30 mm in diameter (T2a), who opted for primary (curative) surgical resection, were asked to participate in an ongoing dynamic ^{18}F-FDG PET study. Patients with diabetes mellitus or patients who had received prior anticancer treatment were excluded. The study was approved by the Institutional Review Board and written informed consent was obtained from each patient.

5.2.2. ^{18}F-FDG PET scanning

Patients fasted for at least 6 h prior to imaging. Capillary blood glucose level <8.0 mmol/L was confirmed in all patients. All scans were acquired on a Biograph Duo [209] scanner (Siemens Healthcare) in a single bed position (159 mm axial length). First, low-dose CT images were acquired for attenuation correction and anatomical reference. At the start time of the PET scan, about 3.45 MBq per kg body weight of ^{18}F-FDG dissolved in 8 mL saline was injected intravenously in 40 s, using a remotely controlled pump (Medrad, Indianola (PA), USA) followed by a 40 mL saline flush in 8 s using a standardized infusion-rate protocol. In total 60 minutes of LM data were acquired.

PET data were reconstructed with ordered subsets expectation maximization in two dimensions (OSEM2D) in 4 iterations with 16 subsets in a 256 × 256 × 53 image matrix (voxel size: 2.65 × 2.65 × 3.00 mm^3) with a 5 mm full-width at half maximum (FWHM) 3D Gaussian filter. Randoms, scatter, attenuation and decay correction were performed.

5.2.3. Simulated arterial plasma time activity curves

To obtain an population based arterial plasma time activity or input curve $C_p^{pop}(t)$, the dynamic PET scans of 15 patients were analyzed. The scans were framed and reconstructed with high temporal resolution (40 × 2, 8 × 5, 3 × 10, 10 × 15, 10 × 30, 16 × 75 and 12 × 150 s). The summed images 0–74 s showed the highest blood-to-background contrast, and were used to manually draw a VOI in the ascending aorta by an experienced nuclear medicine physician.

The image-derived curves thus obtained ($C_p^{img}(t)$) were synchronized at the (whole-blood) peak activity concentration. The extrapolated activity concentration at 60 min after the peak was obtained using a single exponential fit of the last 5 timeframes (12.5 min). Each time-shifted, image-derived curve was normalized at 60 min after the peak (i.e., divided by the extrapolated activity concentration). The data points of these 15 time-shifted and normalized curves ($C_p^{img^*}(t)$) were combined to fit $C_p^{pop}(t)$ as follows. The descending part of $C_p^{pop}(t)$ was fitted using a tri-exponential curve, similar to Hawkins *et al.* [210]. The ascending part of the curve, however, has been modelled differently. Instead of a linear increase, this part was fitted with a mono-exponentially rising function, which better describes the measured data at the high temporal resolution. It results in the following general equation:

$$C_p^{pop}(t) = F \cdot \begin{cases} e^{\lambda_0 (t - t_p)} & t < t_p \\ (1 - A_1 - A_2) e^{-\lambda_1 (t - t_p)} + A_1 e^{-\lambda_2 (t - t_p)} + A_2 e^{-\lambda_3 (t - t_p)} & t \geq t_p \end{cases} \quad (1)$$

where F is a scaling factor in Bq/mL and t_p is the time to peak.

The simulated plasma curves ($C_p^{sim}(t)$) were created based on $C_p^{pop}(t)$ as follows. The eight free parameters (A_1, A_2, $\lambda_0 - \lambda_3$, t_p, F) were pseudo-randomly chosen from a uniform distribution with a range of 20% above and below the fitted values of $C_p^{pop}(t)$, except for the time to peak which ranged from 49 to 60 s, as observed in the patient scans. The scale factor was determined as follows. The simulated plasma curves were scaled to an activity concentration at 60 min after the peak of mean (μ) 7.0 kBq/mL and standard deviation (σ) 1.6 kBq/mL, truncated at 4 and 11 kBq/mL. In *figure 3* the fifteen $C_p^{img^*}(t)$ curves are shown together with the variation in simulated curves.

5.2.4. Simulated tissue time activity curves

$C_t^{sim}(t)$ were generated from the $C_p^{sim}(t)$ curves according to the standard two-tissue irreversible compartment model [188]. For this, the tumour microparameters K_1, k_2, k_3 and V_b were pseudo-randomly generated within plausible biological ranges. An overview of recent dynamic ^{18}F-FDG PET studies in oncology is shown in *table 1*. In the last row, the distributions from which $C_t^{sim}(t)$ were generated are displayed. As additional constraints, the tumour activity concentration 60 min post-injection had to be at least 1.5 times higher than, and at maximum 20 times higher than the arterial plasma activity concentration 60 min post-injection. This was done in order to represent tumours with obvious ^{18}F-FDG accumulation and within a plausible biological range; all other curves were rejected.

5.2.5. Framing

The pseudo-randomly generated $C_p^{sim}(t)$ and $C_t^{sim}(t)$ curves were sampled into time frames according to various framing schedules, which will be clarified below. These schedules were created with four different methods, i.e., the determinant of the Fisher information matrix, the Max-Lloyd quantizer, transformations of $C_p^{pop}(t)$ and based on literature. The same limitations as in the Biograph reconstruction software were used for the framing schedules, i.e., a maximum of 99 frames, a minimal frame duration of 1 s, and frame durations of integer numbers of seconds only. Frames are described by their average activity concentration and frame mid-time.

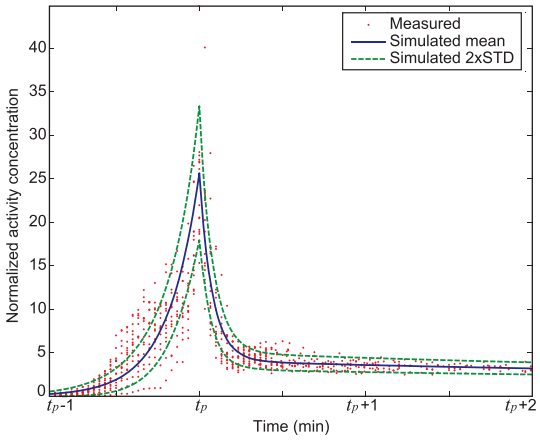

Figure 5.3:
The time-shifted, normalized arterial plasma time activity curves for fifteen study patients ($C_p^{img^*}(t)$; depicted in red) together with the range of simulated curves ($C_p^{sim}(t)$). The variation in time to peak (t_p) and scale factor have not been incorporated in the image for clarity. Only the first few minutes of the curves are shown.

Table 5.1: Tumour microparameters in recent literature and the distributions used in this study.

Study	K_1 (mL/g/min)	k_2 (min^{-1})	k_3 (min^{-1})	V_b
Torizuka *et al*. [71] (1999) Mean ± STD	0.142 ± 0.071	0.290 ± 0.228	0.164 ± 0.139	n/a
Strauss *et al*. [73] (2004) Mean ± STD	0.340 ± 0.262	0.417 ± 0.285	0.072 ± 0.082	0.352 ± 0.262
Spence *et al*. [74] (2004) Mean ± STD	0.073 ± 0.045	0.162 ± 0.093	0.101 ± 0.053	n/a
Nishiyama *et al*. [75] (2007) Mean ± STD	0.082 ± 0.030	0.055 ± 0.035	0.085 ± 0.020	0.054 ± 0.026
Strauss *et al*. [79] (2007) Mean ± STD	0.464 ± 0.195	0.735 ± 0.240	0.110 ± 0.056	0.098 ± 0.079
Vriens *et al*. [211] (2010) Median (interquartile range)	0.11 (0.077 – 0.16)	0.44 (0.25 – 0.89)	0.089 (0.058 – 0.12)	0.089 (0.057 – 0.14)
Distribution used in simulations	Log-normal: μ: -2, σ: 0.8	Log-normal: μ: -1, σ: 0.8	Uniform: 0.065 – 0.110	Uniform: 0.025 – 0.175

The methods could realize a (very) high temporal resolution in the beginning of the scan, the period in which the largest changes in activity concentration occur. Because of this, only a small number of frames remain for later time points, so to prevent this pile-up of short frames in the beginning, framing schedules have also been created with longer minimal frame durations (2–30 s).

I. Determinant of the Fisher information matrix

The first set of framing schedules was obtained by maximizing the determinant of the Fisher information matrix (or the D-optimally criterion). This method has been used to obtain an optimal framing schedule in other studies as well, e.g., Li *et al.* [212]. The objective of these studies, however, has usually been to reduce the number of time frames in order to minimize data storage requirements and reduce the processing time. Nowadays, such limitations are less stringent and the method was applied in this study without this restriction.

In short, the determinant of the Fisher information matrix is maximized by modifying the framing schedule iteratively. During each iteration, the determinant is increased by reducing one time frame in duration while another is increased, keeping the total scan duration at 60 minutes. The process is repeated until the determinant of the Fisher information matrix no longer increases. The Fisher information matrix (F) is a 4-by-4 matrix with each element (row i, column j) described by:

$$F_{i,j} = \sum_{n=1}^{N} \frac{1}{\sigma^2(n)} \left[\frac{\partial C_t^{framed}(n)}{\partial p_i} \right] \left[\frac{\partial C_t^{framed}(n)}{\partial p_j} \right] \qquad (2)$$

With n the time frame, N the total number of time frames, $\sigma^2(n)$ the variance in frame n, $C_t^{framed}(n)$ the activity concentration in frame n, and p the parameters $\{K_1, k_2, k_3, V_b\}$.

A more thorough theoretical background of the method is given by D'Argenio [213] and for nuclear medicine specific application by Li *et al.* [212]. A similar procedure as described by Li and co-workers has been implemented for this study with some differences in both the model and the iterative procedure. We used a log-normal noise distribution (specified below), instead of the normally distributed noise as used by Li *et al.* In addition to the parameters K_1, k_2, and k_3 we also included V_b. The iterative procedure to maximize the determinant of the Fisher information matrix to obtain the optimal sample schedule was used without the merging operation as used by Li *et al.* Instead, the iterative procedure was repeatedly run with increasing numbers of frames (5–80). Furthermore, a decrease in frame duration of one frame was accompanied by an increase of duration in any of the others for a maximal increase in the determinant of the Fisher information matrix per iteration. This was done instead of adjusting two adjacent frames during each iteration as done by Li *et al.*

II. Max-Lloyd quantizer

A second method to obtain framing schedules used the Max-Lloyd algorithm [214,215] for optimal quantization, applied to $C_p^{pop}(t)$. Instead of optimally sampling the curve (i.e., discretizing the time variable), it was optimally quantized (i.e., the activity concentration variable is discretized). This Max-Lloyd algorithm minimizes the quantization error. The times corresponding to the quantization levels produced by the algorithm were used as frame cut-off points.

III. Curve transformations

The third set of framing schedules was obtained from transformations of $C_p^{pop}(t)$. The integral ($\int C_p^{pop}(t)dt$), the decay *un*corrected integral ($\int C_p^{pop}(t)e^{\lambda t}dt$), and the integral of the absolute derivative ($\int \left|\frac{d}{dt}(C_p^{pop}(t))\right|dt$) were used. The latter represents the cumulative change in the blood time-activity curve. By separating the vertical axis into equal parts and obtaining corresponding sample times on the horizontal axis, the framing schedules were created.

IV. Literature

The largest differences in the framing schedules in literature are seen in the first minutes of the scan. Four framing schedules that form a good representation of these differences were selected, with a minimal frame duration of 30 s by Strauss *et al.* [79], 20 s by Nishiyama *et al.* [75], 10 s by Torizuka *et al.* [71], and 5 s by Krak *et al.* [72].

5.2.6. Noise model

After sampling $C_p^{sim}(t)$ and $C_t^{sim}(t)$ according to the framing schedules, these curves are still noiseless. Therefore, a realistic frame-duration dependent amount of noise was added to each mid-frame activity concentration. The relation between frame duration, activity concentration and noise had to be determined. Although nuclear decay probability follows a Poisson distribution, the distribution of voxel values in reconstructed PET images rarely does. This is due to several post-acquisition operations such as randoms and scatter correction, and to the non-negativity constraint generally used in expectation maximization reconstruction algorithms. For this type of algorithms, which are normally used in commercial PET image reconstruction software, it has been shown that the reconstructed activity concentration can be described accurately with a log-normal distribution [216].

$$E(x) = e^{\mu+\frac{1}{2}\sigma^2} \tag{3}$$

$$Var(x) = (e^{\sigma^2}-1)e^{2\mu+\sigma^2} \tag{4}$$

With $E(x)$ the expected value (or mean), and $Var(x)$ the variance of a voxel value, given a certain μ and σ.

A 20 cm diameter cylindrical phantom with a uniform activity distribution was scanned to determine the image noise produced by the Biograph scanner. The mean and standard deviation of the natural logarithm of the voxel values were obtained for reconstructions with varying frame durations (1 s – 60 min) and activity concentrations (2.3 and 1.6 kBq/mL). This resulted in a model describing the noise in the images. The correct values for μ and σ can be obtained through this model, given frame duration and activity concentration. For the simulated curves, log-normally distributed pseudo-random numbers were generated with μ and σ determined using the framing schedule for the frame durations, and the physical decay uncorrected $C_t^{sim}(t)$ and $C_p^{sim}(t)$ curves for the activity concentration.

Pharmacokinetic modelling is often based on VOIs larger than one voxel. Therefore, 40 noisy curves for the tumour were created and averaged. This corresponds to a tumour-VOI of 845 mm^3, or a sphere of 11.7 mm diameter. For blood, 20 voxels were simulated and averaged, corresponding to 423 mm^3, or a sphere of 9.3 mm diameter.

5.2.7. Microparameter estimation

Microparameter estimation was performed with the pharmacokinetic analysis toolbox from Inveon Research Workplace (IRW; v3.0; Siemens Healthcare), which uses the Levenberg-Marquardt algorithm as implemented in Minpack [217] for non-linear least squares parameter fitting. The toolbox has been modified to allow for direct access from MATLAB in order to automatically process many curves in sequence. The number of restarts with random start parameters was set at five.

Uniform weighting and Poisson weighting are available in IRW for non-linear regression. Because Thiele and Buchert [153] have shown that Poisson weighting based on the measured, noisy, tissue curve leads to higher bias and noise than uniform weighting in the resulting microparameters, uniform weighting was selected for microparameter estimation.

5.2.8. Statistical analysis

The resulting set of estimated microparameter values was compared to the set used to generate the $C_t^{sim}(t)$ curves for in total 10,000 sets per framing schedule. The difference between them was expressed as ΔP:

$$\Delta P = \begin{cases} P_{in} / P_{out} - 1 & P_{in} \leq P_{out} \\ -P_{out} / P_{in} + 1 & P_{out} < P_{in} \end{cases} \quad (5)$$

where P indicates the five microparameters, $\{K_1,k_2,k_3,V_b,K_i\}$; *in* and *out*, represent the microparameters used to generate $C_t^{sim}(t)$, and the estimated microparameters, respectively. K_i is calculated according to $K_i = K_1k_3 / (k_2+k_3)$. ΔP is defined in this manner, because underestimations of parameters are thus expressed on the same scale $(0 - \infty)$ as overestimations, with the former being negative and the latter positive. This allows estimation errors to be easily compared.

In order to quantify the accuracy of each framing schedule, the median and two interpercentile ranges (IPRs) of ΔP were calculated. The 50% IPR (between the 25th and 75th percentile) and the 95% IPR (between the 2.5th and 97.5th percentile) were considered.

5.2.9. Clinical applicability

The framing schedule showing the highest accuracy (with lowest IPRs and a median closest to zero) in the simulations was used for the reconstruction of fifteen dynamic PET scans. In addition, the scans were reconstructed with the four framing schedules from literature defined above to evaluate the effect of framing schedules on clinical data. The VOI for the whole-blood input function has been created as described before. For the tissue time activity curve both a 40-voxel VOI in the centre of the tumour, and a 50% isocontour of the maximum value in the tumour were defined on the images representing the last 5 minutes of each scan. Because the tumours were distant from the blood pool from which the whole-blood curve was obtained in all patients, a time delay between plasma and tissue curve was used. The same time delay was used for all four framing schedules. The ^{18}F-FDG influx constant (K_i) was calculated according to $K_i = K_1k_3 / (k_2+k_3)$ and not by Patlak linearization [121].

5.3. Results

5.3.1. Simulation study

Several trends were seen in the simulation results, independent of the method by which the framing schedules were created. As can be seen in the representative example in *figure 4*, an increase in the number of frames increases the accuracy of the estimated microparameters, with especially lower IPRs. Large improvements in accuracy can be observed up to 40 time frames. Accuracy increases even more until about 55 frames, but this improvement is smaller. With more than 55 frames no additional increase in accuracy is seen.

Furthermore, the minimal frame duration has a large influence on the accuracy. When we consider the framing schedules with 40 time frames or more, the median is closest to zero at a minimal frame duration of three seconds for all four microparameters, see *figure 5*. Both IPRs are lowest at a minimal frame duration of about five seconds for all microparameters. Figure 5 clearly shows the trade-off between noise and temporal resolution. With a minimal frame duration of one second, estimation accuracy is low as a result of high noise levels in these short time frames, whereas with a minimal frame duration of 30 seconds, accuracy is reduced as a result of the low temporal resolution. The latter is especially apparent for V_b: clearly a relatively short frame duration is required to obtain an accurate estimate of this microparameter.

The same effects were seen in the accuracy of the estimated influx constant, K_i. The error, however, is much smaller, with a 95% IPR of ~5% or less for all but the framing schedule with a minimal frame duration of 30 seconds.

The various methods used to create framing schedules do not differ much in accuracy as long as the initial frame durations and number of frames are chosen correctly. Therefore, we also tested a manually adjusted framing schedule which met the same requirements: 1 × 10, 21 × 4, 1 × 6, 5 × 10, 5 × 30, 5 × 60, 6 × 120, 6 × 180, 5 × 240 s. The first frame in this schedule is, with 10 s, longer than the rest of the frames in the initial part of the scan. This is because the first activity arrives only after this period. This framing schedule performed as well as the other schedules, and was defined as our optimal schedule.

5.3.2. Clinical applicability

In *figure 6*, the framing schedules of Strauss *et al.* [79], Nishiyama *et al.* [75], Torizuka *et al.* [71] and Krak *et al.* [72] and our optimal framing schedule were compared using the ^{18}F-FDG PET scans of fifteen patients for the VOI segmented with 50% of the maximum uptake in the tumour. In scans of patients that had moved during the scan, the VOIs were manually adjusted to compensate. The differences between the various framing schedules were large, especially in k_2 with an average relative standard deviation of 30%. The average relative standard deviation in K_1, k_3 and V_b were 14%, 13% and 15% respectively. The value of K_i (computed from $K_1k_3/(k_2+k_3)$) was hardly affected by the framing schedule used. The average relative standard deviation was 5%, and without the (single) outlier this value was reduced to only 2%. This outlier was caused by the low value of k_3 in this particular patient in one of the framing schedules.

In case of the 40-voxel VOI, the numbers were similar with an average relative standard deviation in K_1, k_2, k_3, V_b and K_i of 37%, 62%, 28%, 34% and 6% respectively.

5.4. Discussion

Simulations are the only method to assess the effectiveness of the different framing schedules since in clinical data, the true tumour microparameters cannot be determined. Nonetheless, we have used clinical data to evaluate the influence of the framing schedule, showing the

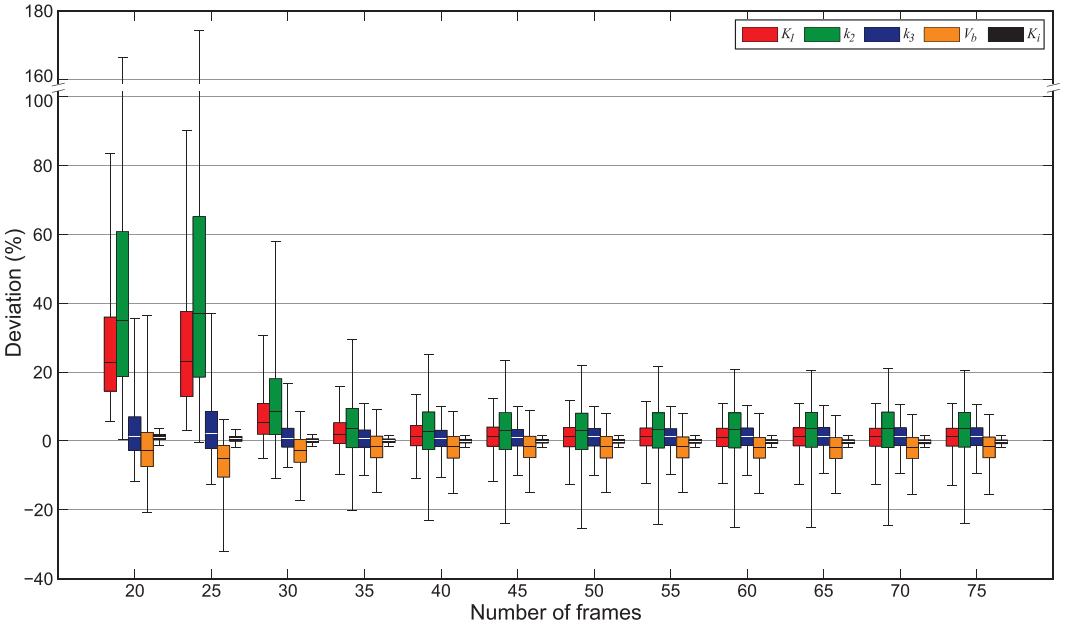

Figure 5.4: Simulation results of framing schedules created with the Fisher information matrix. The horizontal axis shows the total number of time frames, the vertical axis shows ΔP, or the percentage deviation of the estimated (output) parameters from the real (input) parameters. The minimal frame duration was set at 4 s. Each box represents the 25th, 50th (median) and 75th percentile, the whiskers represent the 2.5th and 97.5th percentile of the 10,000 simulation per framing schedule.

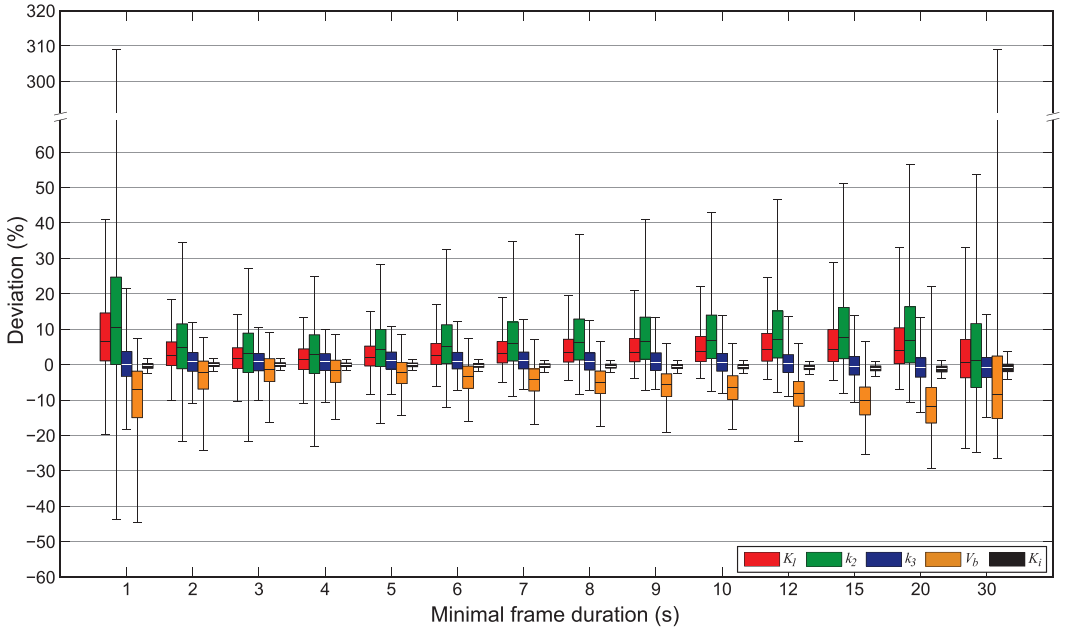

Figure 5.5: Simulation results for all microparameters of framing schedules created with the Fisher information matrix. Only the results for a total of 40 frames are shown. The minimal allowed frame duration is shown on the horizontal axis, ΔP, or the deviation of the estimated (output) parameter from the real (input) parameter is shown on the vertical axis. Each box represents the 25th, 50th (median) and 75th percentile, the whiskers represent the 2.5th and 97.5th percentile of the 10,000 simulation per framing schedule.

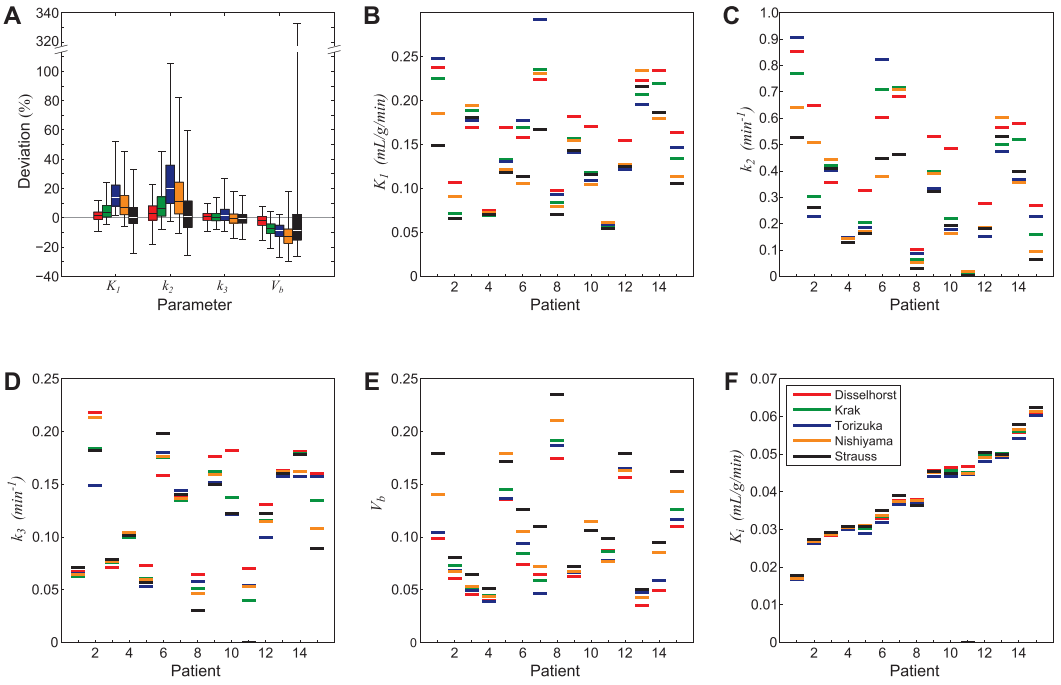

Figure 5.6: Comparison between five different framing schedules, four from literature and one defined in this study. In (A), the results for the simulations are shown. Each box represents the 25th, 50th (median) and 75th percentile, the whiskers represent the 2.5th and 97.5th percentile of the 10,000 simulation per framing schedule. In (B-E), the tumour microparameters obtained in fifteen patients reconstructed with different framing schedules are shown. The K_i parameter, or ^{18}F-FDG influx constant, is shown in (F) defined as $K_i = K_1 k_3 / (k_2 + k_3)$. These results are obtained in VOIs of 50% of the maximum voxel in the tumour.

considerable influence on estimation of all parameters. Only the ^{18}F-FDG influx constant K_i is almost unaffected by the framing schedule. The influx constant has, in this case, been calculated with K_1, k_2 and k_3, but can also be obtained from Patlak analysis [121]. The data-requirements for a Patlak analysis are different than those for full pharmacokinetic modelling, since the area under the curve is most important, eliminating the need for high temporal resolution. Therefore, when the influx constant is the only parameter of interest, our optimal framing schedule does not necessarily apply, regardless the method of calculation.

As can be concluded from both the simulations and clinical data, the framing schedule has a large influence on the analysis results in a dynamic PET study. This is reflected in *figure 6*, where the clinical data has been analyzed with five different framing schedules. The differences are large and this clearly indicates that it is worthwhile to determine the optimal framing schedule for a certain scanner, study and infusion protocol. Although simulations have been performed for ^{18}F-FDG only, conclusions may be adopted to some extent for other radiopharmaceuticals, since the blood peak activity concentration has an especially large influence on the resulting framing schedule. Many PET tracers show similar blood activity concentration-time profiles as long as the infusion is performed in a similar manner. Only when a positron emitter with a much shorter half-life is used, such as ^{13}N, may an optimal framing schedule differ more. The current framework, however, can be easily adapted to handle other tracers, as long as an accurate arterial plasma curve is available and tissue kinetics can be described by a compartment model.

The conclusions of earlier studies to the influence of the framing on the accuracy of pharmacokinetic modelling have been different from our conclusion, principally because of advances in

scanner sensitivity and reconstruction techniques. For instance, Mazoyer *et al.* [32] state that only small improvements in estimation accuracy can be obtained by decreasing the frame duration in the initial phase of the scan to less than 30 s. Also Jovkar *et al.* [68] conclude that 30 s is the optimal duration for the initial sampling. However, the dynamic PET scans were performed with an input function obtained from blood samples in both studies, instead of an image derived input function. Furthermore, Jovkar *et al.* have excluded V_b, the parameter that showed the largest error in our analyses. Raylman *et al.* [27] suggest that a higher framerate is required for studies using an image derived input function.

In images obtained with modern-day PET scanners it is possible to increase estimation accuracy by reducing the frame duration to around 4 or 5 seconds. Li *et al.* [212] never make use of such short durations because a minimum for each frame is set at 10 s. Moreover, their use of a merging operation produces optimal framing schedules with only a limited number of frames. In clinical data, relatively large time variations in occurrence of the blood peak are observed. With few time frames these variations can reduce the accuracy of the microparameter estimation. The accuracy can be improved by using more frames, as can be seen in *figure 4*.

In the simulations, we did not take a time-delay into account, and assumed the highest blood activity concentration in the tumour to be synchronized with the highest activity concentration in the input function. This will not be exactly the case in clinical situations, since the input function is derived from an arterial blood pool distant from the tumour with a different activity concentration-time profile than within the tumour arterioles. Delays of up to several seconds can be encountered in dynamic PET studies when the target tissue is relatively far away from the blood pool used for the input function. Such a time delay may require a different framing schedule optimization, although we do not expect this because during simulations the time to peak was varied and the time delay is usually corrected for in the clinical setting.

Concluding from the present results, it appears that using more frames always leads to more accurate tumour microparameters, although after a certain number of frames, additional frames only lead to a small improvement in accuracy. Aspects such as computation time and storage requirements most probably outweigh these limited accuracy improvements. However, there clearly is an optimum in the minimal frame duration demonstrating the trade-off between noise and temporal resolution. Several methods can be used to generate the optimal framing schedule with only minimal differences in accuracy as long as the minimal framing duration has been chosen correctly and the framing schedule includes a sufficient number of frames.

Not all framing schedules from literature perform adequately. However, caution should be used when interpreting these results: these framing schedules may have been appropriate for a certain infusion protocol and particular scanner or are only used for other analyses such as Patlak. Decreased performance in pharmacokinetic modelling during our simulations only makes them less adequate for dynamic PET studies similar to the one described here. The results presented in this study do show that the minimal frame duration should be short, even with the relatively slow ^{18}F-FDG infusion of 40 seconds. In case of a faster, or even bolus infusion, the peak activity concentration is expected to be only narrower, possibly requiring even shorter time frames in the early portions of the scan. The higher accuracy of our framing schedule as compared to Krak et al. [72] can be explained by our infusion as well. Although Krak *et al.* have 5-s frames in the early portion of the scan, this frame duration is only maintained for the first 30 seconds which is, for our study protocol, too short.

Most of the results are based on simulations, which allow for a high degree of flexibility, but also have their limitations. Heterogeneity in tumour microparameters cannot be estimated easily in real tumours, and has therefore been neglected in these simulations. All voxels in one simulated tumour have the same microparameters, which is unlikely to occur in a real tumours in vivo. How-

ever, in these simulations, each tumour is only represented by a 40 voxel VOI, which is relatively small compared to the size of many tumours. Within such a small region we expect only small biological variations within the microparameters. Because the results are VOI-based, noise had a smaller effect than it would have with single voxel simulations.

5.5. Conclusion

These analyses clearly demonstrate that the framing schedule used in a dynamic PET study has a strong influence on the tumour microparameters obtained after pharmacokinetic modelling, and optimized framing schedules can be created. The minimal duration of the time frames has a large influence on the accuracy of the estimated microparameters. The optimum frame duration in the early part of the scan is 4–5 s. Naturally, there should be a sufficient number of time frames of this duration to capture the blood peak completely. With shorter durations, the noise in the images hampers pharmacokinetic analysis. With longer frames, the temporal resolution is too low for accurate estimation, especially of V_b. The accuracy of microparameter estimation increases with number of frames. The largest improvements can be expected up to about 40 frames, moderate improvements up to about 55 frames, and a negligible increase in accuracy when more time frames are used, in a 60-min dynamic study with 40-s ^{18}F-FDG infusion. The influx constant K_i is almost unaffected by the choice of framing.

5.6. Acknowledgement

This work was supported by Siemens Molecular Imaging, Oxford. We thank Dr. Xiao-Bo Pan and Dr. Jérôme Declerck for valuable discussions.

6. Quantitative Assessment of Heterogeneity in Tumor Metabolism using ^{18}F-FDG PET

Dennis Vriens[1*], Jonathan A. Disselhorst[1*], Wim J.G. Oyen[1], Lioe-Fee de Geus-Oei[1] and Eric P. Visser[1]

[1] Department of Nuclear Medicine, Radboud University Nijmegen Medical Centre, Nijmegen, The Netherlands

* Both authors contributed equally

Int J Radiat Oncol Biol Phys. Accepted

Abstract

^{18}F-fluorodeoxyglucose-positron emission tomography (^{18}F-FDG PET) images are usually quantitatively analyzed in "whole-tumor" volumes of interest. Also parameters determined with dynamic PET acquisitions, such as the Patlak glucose metabolic rate (MR_{glc}) and pharmacokinetic rate constants of 2-tissue compartment modeling are most often derived per lesion. We propose segmentation of tumors to determine tumor heterogeneity, potentially useful for dose-painting in radiotherapy and elucidating mechanisms of ^{18}F-FDG uptake.

Methods: In 41 patients with 104 lesions dynamic ^{18}F-FDG PET was performed. On MR_{glc} images, tumors were segmented in quartiles of background subtracted maximum MR_{glc} (0 – 25%, 25 – 50%, 50 – 75% and 75 – 100%). Pharmacokinetic analysis was performed using an irreversible two-tissue compartment model in the three segments with highest MR_{glc} to determine the rate constants of ^{18}F-FDG-metabolism.

Results: From the highest to the lowest quartile, significant decreases of uptake (K_1), washout (k_2) and phosphorylation (k_3) rate constants were seen with significant increases in tissue blood volume fraction (V_b).

Conclusions: Tumor-regions with highest MR_{glc} are characterized by high cellular uptake and phosphorylation rate constants with relatively low blood volume fractions. In regions with less metabolic activity, the blood volume fraction increases and cellular uptake, washout and phosphorylation rate constants decrease. These results support the hypothesis that regional tumor glucose phosphorylation rate is not dependent on the transport of nutrients (i.e., ^{18}F-FDG) to the tumor.

6.1. Introduction

Positron emission tomography (PET) is a molecular imaging technique to quantitatively assess various tissue properties with an appropriate radiotracer such as ^{18}F-fluoromisonidazole (FMISO) for hypoxia [218] or ^{18}F-fluorothymidine (FLT) for proliferation [219]. However, ^{18}F-fluorodeoxyglucose (FDG), which visualizes glucose metabolic processes in tissues, remains the most commonly used radiotracer with PET. ^{18}F-FDG PET has obtained a clear role in tumor staging [220] and is used to assess therapy response and predict outcome [221]. In most cases the standardized uptake value (SUV) is used to quantify whole-tumor ^{18}F-FDG-uptake. Most tumors however, display heterogeneous uptake in ^{18}F-FDG PET images, which may reflect different biologic behavior in the different regions within these lesion. Identifying this metabolic heterogeneity would not only be useful for understanding tumor biology, but might be of prognostic significance or of use for radiotherapy planning and dose painting by intensity-modulated radiation therapy (IMRT) as well [222].

To examine processes underlying the uptake of ^{18}F-FDG in a tumor, sophisticated quantification methods such as determination of pharmacokinetic rate constants of 2-tissue compartment models can be used [110,152], requiring dynamic PET images. With these pharmacokinetic analyses, the properties of the ^{18}F-FDG metabolism can be elucidated. Delivery of ^{18}F-FDG in and out the cell corresponds to the rate constants K_1 and k_2, respectively. Once intracellular, phosphorylation of ^{18}F-FDG is represented by k_3, dephosphorylation by k_4, and V_b finally, indicates the fraction of blood within the volume of interest (VOI). The 2-tissue compartment model of FDG metabolism is shown in *figure 6.1*. Pharmacokinetic rate constants, and other model-based parameters are usually derived in a VOI, mostly representing the whole tumor. These parameters therefore, correspond to averaged values of tumor glucose metabolic activity. To assess intratumoral heterogeneity, the parameters could be obtained for every individual voxel within the tumor (voxel-wise modeling). The time-activity curves for single voxels, however, are relatively noisy. This prevents accurate determination of tumor parameters using non-linear least squares (NLLS) methods [223]. Moreover, tumor movement (e.g., as a result of breathing) has a relatively large influence in these small volumes as in this case each voxel does not necessarily represent a single volume of tissue.

As a trade-off, less detailed parameters (such as the metabolic rate of glucose (MR_{glc})) can be used, for which voxel-wise quantification is feasible, since they can be based on linearization methods which are far less sensitive to noise (e.g., using the Patlak method [121]). Another method to overcome high noise levels is to decrease spatial image resolution by reconstruction at smaller matrix sizes. Post-reconstruction smoothing could also be used to increase signal-to-noise ratios at the cost of spatial resolution.

Similarly, higher signal-to-noise ratios can be obtained by tumor segmentation and taking the mean value in each segment, which could be used to determine tumor regional variation in 2-tissue compartment model rate constants of ^{18}F-FDG metabolism (K_1-k_4) and blood volume fraction (V_b).

We applied the latter method and segmented the tumors based on the MR_{glc} images, taking advantage of the higher tumor-to-background ratio as compared to standard uptake images [224]. Furthermore, we wanted to verify our hypothesis that tumor regions with the highest MR_{glc} are characterized by high ^{18}F-FDG extraction and phosphorylation rates.

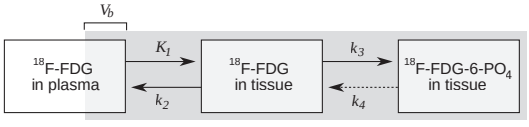

Figure 6.1: The 2-tissue compartment FDG model with pharmacokinetic rate constants K_1, k_2, k_3, and k_4. The measured PET signal (shown as a gray box) is a combination of ^{18}F-FDG in tissue and a fraction of blood, V_b. The influx constant, K_i, can be calculated from the other rate constants with: $K_1k_3/(k_2+k_3)$.

6.2. Patients and methods

6.2.1. Patient population & data acquisition procedure

From an existing database of dynamic ^{18}F-FDG PET scans of oncological patients acquired on a Siemens ECAT EXACT47 (Siemens Healthcare), 41 patients with 104 tumors of different origin (*table 1*) were selected [2,3]. Selection criteria were: previously untreated patients in whom a fully arterially sampled input function is available. The study was approved by the Institutional Review Board of the Radboud University Nijmegen Medical Centre and written informed consent was obtained from each patient. Details of the study have been described before with the only difference that the present images were reconstructed in 128 × 128 × 47 matrices using 2D ordered subsets expectation maximization (OSEM2D) with 4 iterations and 16 subsets and a 5 mm 3-dimensional (3D) Gaussian filter. In brief, fasted patients were injected with ^{18}F-FDG by an automated standardized infusion protocol. Immediately thereafter, 17 arterial blood samples were taken at set time points from which plasma was obtained to provide a sampled arterial plasma time activity concentration curve ($C_{plasma}(t)$). Simultaneously, a dynamic PET-acquisition consisting of 16 time-frames of variable duration was obtained to provide the tissue time activity curve). Voxel volumes in the reconstructed images were 39.75 mm^3 (transaxial voxel size 3.432 × 3.432 mm, axial voxel size 3.375 mm).

6.2.2. Data analysis

Data analysis was performed using Inveon Research Workplace (IRW version 2.2, Siemens Healthcare). First, voxel-wise Patlak linear regression [121] of acquired data 10 – 50 min post injection (the last 5 time-frames) was used to obtain the influx constant (K_i) of each voxel.

Table 6.1: Patient characteristics (n=41).

	Value	Range
Mean age [y]	60.8	44.7 – 77.7
Proportion male [%]	68.3	
Median plasma glucose level [mmol·L^{-1}]	5.2	4.2 – 8.3
Median AA per unit body mass [MBq·kg^{-1}]	2.7	1.6 – 5.9
Origin of primary tumor [% of patients]:		
NSCLC	71	
CRC	24	
Breast carcinoma	5	
Origin of primary tumor [% of lesions]:		
NSCLC	82	
CRC	16	
Breast carcinoma	2	
Proposed treatment [%]:		
Induction chemotherapy	22	
First line curative chemotherapy	76	
Palliative care	2	
Differentiation [%]:		
Poor	20	
Slight	15	
Moderate	27	
Mucinous	2	
Unknown	37	

AA: administered activity, CRC: colorectal carcinoma, NSCLC: non-small cell lung carcinoma.

The slope of the Patlak plot equals K_i, and MR_{glc} was calculated by multiplication with the measured venous plasma glucose concentration, thereby assuming a lumped constant (LC) of 1, see *equation 1*. The real value of LC is time and tissue dependent and therefore unknown [225].

$$MR_{glc} = \frac{[Glc]}{LC} K_i = \frac{[Glc]}{LC} \frac{K_1 k_3}{k_2 + k_3} \quad (1)$$

Since pharmacokinetic analysis of dynamic data is sensitive to time-delay (t_d, i.e., the difference in time of arrival of the ^{18}F-FDG-bolus in the tumor and in the sampled artery), manual time-offset synchronization of $C_{plasma}(t)$ and $C_{tumor}(t)$ of VOI_{tumor} was performed by visually shifting the ascending limbs of both curves until they overlapped.

On images of MR_{glc}, one representative background VOI (VOI_{BG}) and three tumor VOIs were determined per lesion, defined by increasing levels of background-corrected MR_{glc} (VOI_{low}, VOI_{medium} and VOI_{high}, summing up to VOI_{tumor}; *table 2*). The quartile with lowest metabolic rate was not included, as the edges of the metabolic volume may contain non-tumor tissues and the noise levels in this segment is higher due to a lower ^{18}F-FDG uptake. We did not attempt any partial-volume correction strategies. VOI_{BG} was defined as an ellipsoidal volume of at least the size of the corresponding tumor and placed in a representative volume of tissue with normal ^{18}F-FDG-uptake (e.g., contralateral lung in case of a lung metastasis).

IRW uses the iterative Levenberg-Marquardt algorithm for NLLS curve fitting, minimizing the weighted least squares deviation [217] to obtain all rate constants and V_b simultaneously, in each tumor VOI separately. The weighting function was chosen as the square root of the frame duration divided by the measured non-decay-corrected activity concentration in each time frame (i.e., Poisson weighting). For initialization of the NLLS algorithm, multiple (=99), randomly selected starting parameters within a defined range (0.0 – 2.0 for the rate constants, 0.0 – 1.0 for V_b) were used.

Data from the literature suggest that the rate of dephosphorylation of ^{18}F-FDG by glucose-6-phosphatase activity (k_4 in the Phelps 4K [110]) is very low in mammalian tissues, except in liver tissue [226]. Moreover, from simulation studies it has been warned that a k_4 might result from tissue heterogeneity rather than real dephosphorylation [148]. All pharmacokinetic analyses were performed using the Sokoloff 3K (K_1-k_3) model [152], as it showed a better fit than the Phelps 4K (K_1-k_4) model [110] in a majority of lesions (data on file).

The resulting values for each parameter were classified as being biologically plausible or not. Values within 3 standard deviations (99.7% confidence interval) of the mean described elsewhere [79,227] were considered biologically plausible by definition. This criterion was set to label unrealistic tumor parameter values, which could be the result of the instability of the nonlinear optimization of extremely noisy time-activity concentration curves. For K_1 this meant the interval 0 – 1.049 mL·g^{-1}·min^{-1}, for k_2 0 – 1.455 min^{-1}, for k_3 0 – 0.511 min^{-1} and for V_b 0.001 – 0.335. The subgroup of lesions considered having biologically plausible results was analyzed separately, to validate that the conclusions drawn based on the whole group were not due to (implausible) outliers. Next, in order to evaluate the influence of blurring caused by the partial-volume effect and

Table 6.2: VOI definitions.

Name	Lower bound	Upper bound
VOI_{high}	BG_{mean} + 0.75 (T_{max}- BG_{mean})	T_{max}
VOI_{medium}	BG_{mean} + 0.50 (T_{max} - BG_{mean})	BG_{mean} + 0.75 (T_{max} - BG_{mean})
VOI_{low}	BG_{mean} + 0.25 (T_{max} - BG_{mean})	BG_{mean} + 0.50 (T_{max} - BG_{mean})
VOI_{tumor}	BG_{mean} + 0.25 (T_{max} - BG_{mean})	T_{max}

BG_{mean}: mean background MR_{glc}, T_{max}: maximum tumor MR_{glc}. MR_{glc}: glucose metabolic rate. VOI: volume of interest.

motion, the subgroup of lesions with a volume of at least 14.1 cm^3 were analyzed, as this volume represents a lesion with a spherical diameter of ±3 cm, which is 5 times the resolution of the scanner (±0.6 cm full width at half maximum).

Finally, these parameters were interpreted in view of their reliability (relative standard error) and mutual independence (correlation matrix).

6.2.3. Statistical analysis

(Log_e)-normally distributed variables are described by mean and 95%-confidence interval (95%-CI: mean ± 1.96 × standard deviation). Variables not obeying the (log_e)-normal distribution are described by median and interquartile range (IQR). For normally distributed values the (paired) t-test and the squared Pearson's Product-Moment Correlation Coefficient (R^2) were used to compare means or express correlation. In case of non-normality, Spearman's ρ was used. Correlation was qualified based on R^2: very high ($R^2 \geq 0.9$), high ($0.7 < R^2 < 0.9$), intermediate ($0.5 < R^2 < 0.7$) or low ($R^2 < 0.5$).

Comparison of multiple groups was performed by non-parametric analysis of variance (Friedman's ANOVA). To correct for multiple comparisons, a *post-hoc* analysis with Wilcoxon signed rank test was conducted with a Dunn's (or Bonferroni's) correction.

Relations between tumor parameters on the one hand and biological plausibility on the other hand were determined using univariable logistic regression. The following continuous variables were candidate predictors: volume, K_i, MR_{glc} and SUV of the smallest VOI (segment). Their discriminative ability was evaluated by determination of the area under the receiver operating characteristics curves (AUC). Difference between the AUC and 0.500 (i.e., AUC for an indiscriminative test) was assessed by asymptotic distribution assumption for significance. All statistical analyses were performed using SPSS version 16.0.2. The cut-off point for statistical significance was set at 0.05.

6.3. Results

Median lesion volume based on VOI_{tumor} was 11.3 cm^3 (corresponding to 283.5 voxels), ranging from 1.7 to 504 cm^3 (42 to 12668 voxels). VOI characteristics of tumor segments are displayed in *table 3*.

Correlation of the VOI_{tumor} parameters showed significant but weak correlation between MR_{glc} and K_1 (ρ: 0.286, p = 0.003), MR_{glc} and k_3 (ρ: 0.488, p < 0.001) but not between MR_{glc} and k_2 (ρ: -0.088, p = 0.372) and MR_{glc} and V_b (ρ: 0.189, p = 0.055). There was also no significant correlation between k_3 and V_b (ρ: 0.045, p = 0.652). The subgroups of NSCLC and CRC showed similar results, as summarized in *table 4*.

An example of lesion segmentation with corresponding time-activity concentration curves is displayed in *figure 2*. As demonstrated in *figure 3*, a clear trend in reduction of K_1, k_2, k_3 and increase in V_b was observed from VOI_{high} toward VOI_{low}, which was significant for all four investigated parameters. The within-group differences were significant between all segments, except for VOI_{high} versus VOI_{medium} for both K_1 and k_2 (*table 3* for values). These trends were seen in significantly more than the expected 25% (if divided equally between the 4 possibilities) of the analyzed lesions: 42% (95%-CI: 33 – 52%) for K_1, 40% (95%-CI: 31 – 50%) for k_2, 79% (95%-CI: 70 – 86%) for k_3 and 93% (95%-CI: 87 – 97%) for V_b. Similar trends are observed when NSCLC and CRC lesions are considered separately. Forty lesions had a volume larger than 14.1 cm^3. In this subgroup, the trends were observed in a higher percentage of the lesions, as displayed in *table 5*.

In 90% of the lesions all four VOI_{tumor} parameters were considered biologically plausible. In

Table 6.3: VOI characteristics.

	VOI_{tumor}	VOI_{high}	VOI_{medium}	VOI_{low}
Median volume * [cm^3] (range)	11.3 (1.67 – 504)	0.556 (0.0795 – 8.11)	1.83 (0.278 – 92.2)	7.85 (1.07 – 406)
Mean MR_{glc} † [$nmol \cdot mL^{-1} \cdot min^{-1}$] (95%-CI)	99.7 (36.4 – 274)	187 (69.8 – 503)	135 (50.3 – 361)	82.7 (30.9 – 221)
Median SUV [$g \cdot cm^{-3}$] (IQR)	4.1 (2.8 – 5.5)	6.8 (4.8 – 8.7)	5.3 (3.7 – 6.8)	3.6 (2.5 – 4.8)
Median K_1 [$mL \cdot g^{-1} \cdot min^{-1}$] (IQR)	0.11 (0.077 – 0.16)	0.18 (0.81 – 0.37)	0.15 (0.092 – 0.23)	0.11 (0.072 – 0.15)
Median k_2 [min^{-1}] (IQR)	0.44 (0.25 – 0.89)	0.99 (0.31 – 2.9)	0.55 (0.29 – 1.1)	0.4 (0.22 – 0.75)
Median k_3 [min^{-1}] (IQR)	0.089 (0.058 – 0.12)	0.19 (0.090 – 0.39)	0.12 (0.070 – 0.17)	0.073 (0.051 – 0.099)
Median V_b (IQR)	0.089 (0.057 – 0.14)	0.036 (0.00063 – 0.086)	0.071 (0.037 – 0.11)	0.095 (0.056 – 0.15)

95%-CI: 95% confidence interval; IQR: interquartile range; MR_{glc}: mean glucose metabolic rate computed assuming a lumped constant of 1 and a blood volume fraction of 0; SUV: standardized uptake value with bodyweight correction measured 40 – 50 minutes post injection; $K_1 - k_3$: rate constants of the 2-tissue compartment model of glucose metabolism; V_b: blood volume fraction; VOI: volume of interest. * one voxel equals a volume 39.75 mm^3. † calculated after log_e-transformation.

the 10 lesions with one or more implausible parameters, K_1 was not within the defined plausible range in 20%, k_2 in 70%, k_3 in 40% and V_b in 50% of these lesions. Multivariable logistic regression showed only K_i to be independently related to plausibility.

When looking at the four parameters in the segments VOI_{high}, VOI_{medium} and VOI_{low} separately, in 45 lesions (43% of the analyzed tumors) all 12 values were within the range of biologic plausibility. In the other 59 lesions (57%) with at least one or more resulting implausible parameters in one or more VOIs, K_1 was not within the plausible range in 15%, k_2 in 81%, k_3 in 34% and V_b in 61% of these lesion. Only the smallest K_i was related to biologically plausible results, which had moderate discriminative ability (AUC 0.680, 95%-CI: 0.578 – 0.783).

When looking only at the 45 lesions with all 12 values within the defined range of biological plausibility we saw similar between VOI_{high} – VOI_{low} for K_1, k_3 and V_b. However this did not reach statistical significance for k_2 (Friedman = 2.80, p = 0.257, downslope trend for VOI_{high} – VOI_{low} in 33%), see *table 5*.

For the 312 NLLS operations (3 tumor segment VOIs in each of the 104 lesions), 10% of K_1, 10% of k_2, 12% of k_3 and 20% of V_b showed relative standard errors larger than 5%. In the 104 (larger VOI) whole-tumor parameters this was only the case in 4%, 4%, 5% and 5% respectively. Correlation matrices of the 312 parameters, showed very high mutual dependence between K_1 and k_2 (median R: 0.96, IQR: 0.96 – 0.97), intermediate mutual dependence between K_1 and V_b (median R: -0.73, IQR: -0.83 to -0.68) and low mutual dependence between K_1 and k_3 (median R: 0.06, IQR: -0.38 to 0.43), between k_2 and k_3 (median R: 0.36, IQR: -0.13 to 0.68), between k_2 and V_b (median R: -0.60, IQR: -0.70 to -0.54) and between k_3 and V_b (median R: 0.34, IQR: 0.03 – 0.66).

Table 6.4: Correlation of VOI_{tumor} parameters.

	MR_{glc} and K_1	MR_{glc} and k_2	MR_{glc} and k_3	MR_{glc} and V_b	k_3 and V_b
All lesions (n=104)	0.286 (0.003) *	-0.088 (0.372)	0.488 (<0.001) *	0.189 (0.055)	0.045 (0.652)
NSCLC (n=85)	0.255 (0.018) *	-0.114 (0.298)	0.507 (<0.001) *	0.141 (0.198)	0.102 (0.352)
CRC (n=17)	0.235 (0.363)	-0.039 (0.881)	0.363 (0.152)	0.365 (0.149)	-0.159 (0.541)

Correlations are obtained on a whole-lesion basis, and are expressed as Spearman's ρ with statistical significance between parentheses. * Statistically significant.

6.4. Discussion

When comparing tumor regions with stepwise decreasing MR_{glc}, there is decreasing phosphorylation rate (k_3) but increasing fractional blood volume (V_b). This cannot be explained by mutual dependence of these variables in the fitting process, since the fit-correlation was low. We could not find a significant correlation between whole-tumor V_b and k_3 between lesions. Glucose phosphorylation rate therefore is not correlated with lesion blood volume fraction. Miles and Williams [228] have reviewed the relation between tumor vascularization and tumor metabolism. Although the total uptake of ^{18}F-FDG is considered rather than k_3, they show that literature on this subject is highly variable. It was reported that the relationship appeared to depend on tumor type, tumor size and tumor grade. In the present study, no significant correlations between V_b and k_3 could be found, not even in the subgroups per tumor type or the subgroup of large tumors, see *table 4*. The weak correlations between MR_{glc} and k_3 (significant) and MR_{glc} and V_b (not significant) might indicate that using MR_{glc} as tumor segmentation variable is responsible for the within-patient inverse relation between the k_3- and V_b-trends over the segments, but the absence of between-lesion correlation between V_b and k_3 suggests another underlying mechanism. Multiple groups reported a correlation between ^{18}F-FDG-uptake during the first few minutes after injection and tumor blood-flow measured by [^{15}O]-H_2O in various tumor types [229,230]. Since a large V_b is mainly responsible for the tumor ^{18}F-FDG-concentration in the (very) early time-frames, at which blood ^{18}F-FDG activity concentrations are still very high, our results suggest that V_b (hence regional tumor perfusion) is inversely related with phosphorylation rate (k_3). Our results suggest that the "metabolic center" of the tumor can maintain high phosphorylation rates (k_3) at relatively low blood volume fractions (V_b). This interesting result may support the hypothesis that as the tumor grows, angiogenesis becomes unable to maintain an adequate blood supply, contributing to the uncoupling of glucose metabolism and blood flow, a theory also

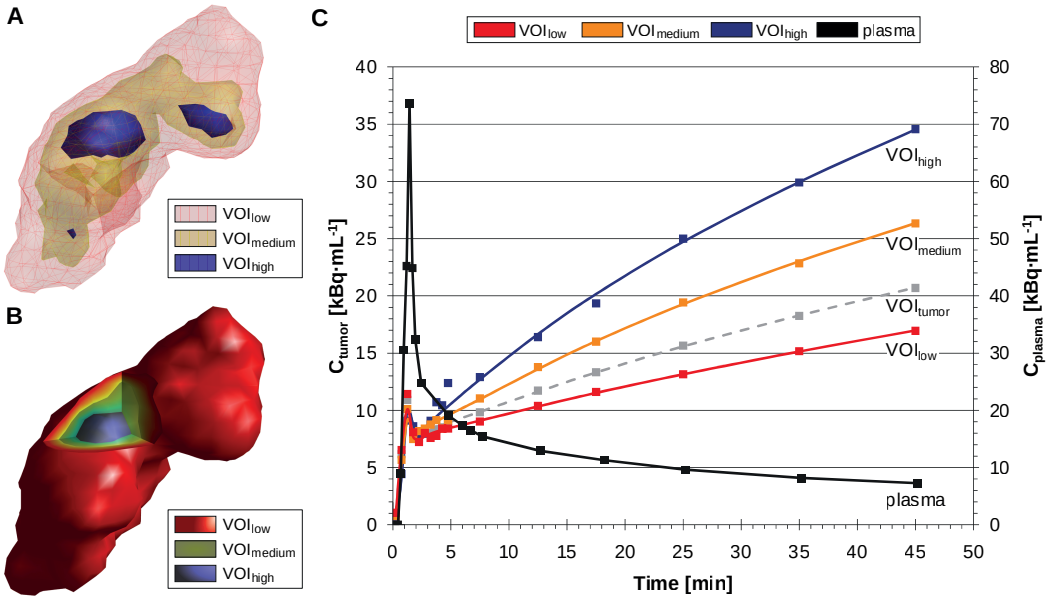

Figure 6.2: Representative example of a patient with cT3N2M0 NSCLC. The lesion's largest diameter was 58 mm. (A) A surface rendered image of the 3 VOIs clearly demonstrating the heterogeneity in ^{18}F-FDG metabolism. (B) The same lesion "opened up". (C) graph showing the activity concentration curves in the 4 tumor VOIs (VOI_{low}, VOI_{medium}, VOI_{high} and VOI_{tumor}, left axis) and in the sampled arterial plasma (plasma, right axis).
C_{plasma}: sampled arterial plasma activity concentration, C_{tumor}: tumor (VOI) activity concentration, NSCLC: non-small cell lung carcinoma, VOI: volume of interest.

known as the Warburg Effect [231]. It should be noted that V_b as obtained with pharmacokinetic modeling may not reflect the complete blood fraction in the tumor. The venous blood time activity curve may have a shape very different from the arterial blood time activity curve as used for the compartment analysis. This could result in an underestimation of V_b.

Tumor hypoxia is disadvantageous property for several cancer treatments including radiation therapy [232]. Numerous methods to detect or visualize hypoxia in vivo are available which include hypoxia specific PET tracers such as ^{18}F-FMISO. Some suggest to employ ^{18}F-FDG PET for dose painting because of the disadvantages of hypoxia tracers, e.g., a low tumor to background ratio, low reproducibility, and slow clearance of these tracers in non-hypoxic regions [233]. Although ^{18}F-FDG is certainly not a tracer specific for hypoxia, there is a correlation between ^{18}F-FDG uptake and hypoxia in tumors [234]. More details about the metabolism of ^{18}F-FDG can be obtained using dynamic PET. We have shown an inverse relation between V_b and k_3, which might be indicative for a poorer oxygenation in the metabolic centre of the tumor, because of increased demand of oxygen and nutrients (higher phosphorylation), but decreased delivery (lower volume fraction of blood). Continuous

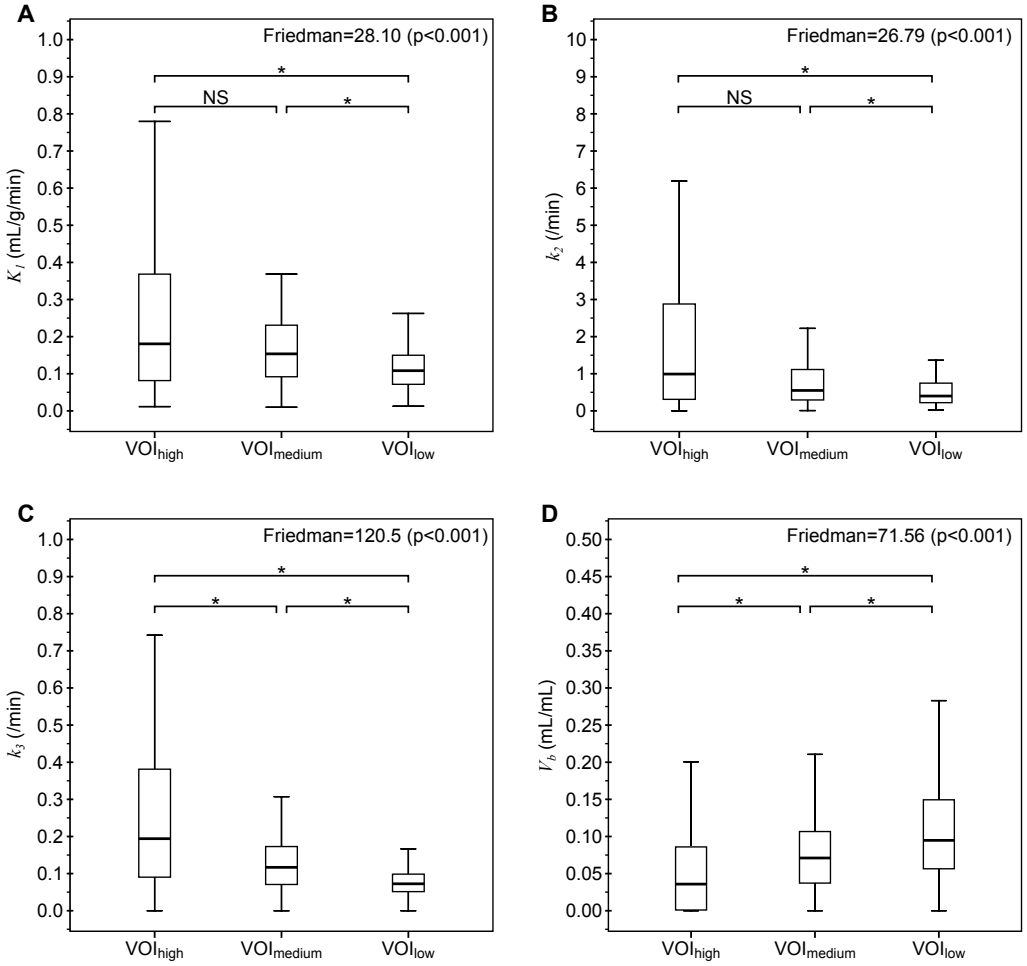

Figure 6.3: Differences in rate constants and blood volume fraction in different tumor VOIs. Friedman: Friedman's non-parametric analysis of variance overall test. NS: not significant, *: significant with Wilcoxon signed rank test *post-hoc* analysis with Dunn's correction applied (p<0.001). VOI: volume of interest.

Table 6.5: Comparisons between tumor segments.

	K_1	k_2	k_3	V_b
All lesions (n=104)	28.1 (< 0.001) Follows trend in 42.3%	26.8 (<0.001) Follows trend in 40.4%	120.5 (<0.001) Follows trend in 78.8%	71.6 (<0.001) Follows trend in 93.3%
NSCLC (n=85)	26.6 (<0.001) Follows trend in 40.0%	16.3 (<0.001) Follows trend in 36.5%	99.7 (<0.001) Follows trend in 77.6%	54.5 (<0.001) Follows trend in 92.9%
CRC (n=17)	2.5 (0.312) Follows trend in 47.1%	12.1 (0.002) Follows trend in 52.9%	17.3 (<0.001) Follows trend in 82.4%	22.2 (<0.001) Follows trend in 100%
Plausible † (n=45)	9.0 (0.011) Follows trend in 40.0%	2.8 (0.247) Follows trend in 33.3%	37.9 (<0.001) Follows trend in 68.9%	14.4 (0.001) Follows trend in 86.7%
Volume >14.1 cm^3 (n=40)	25.6 (<0.001) Follows trend in 62.5%	43.6 (<0.001) Follows trend in 65.0%	61.4 (<0.001) Follows trend in 92.5%	52.9 (<0.001) Follows trend in 95%

Comparison between tumor segments is expressed as Friedman's χ^2 with statistical significance between parentheses. A trend between the segments is expressed as a percentage of lesions, for $K_1 - k_3$ this trend is $VOI_{high} > VOI_{medium} > VOI_{low}$, for V_b this trend is $VOI_{high} < VOI_{medium} < VOI_{low}$. † Lesions with all 12 parameters within the defined range of biological plausibility.

uptake of ^{18}F-FDG, despite a poor vasculature, is a sign of adaptation of the tumor to the hypoxic conditions. The intratumoral metabolic heterogeneity suggests differences in the tumor microenvironment (including distribution of hypoxia), which might have an impact on radiation treatment planning.

We do not believe that the high number of lesions with outlying parameters influenced our conclusions as we saw similar results in the subgroup of lesions in which all parameter values were considered biologically plausible.

A potentially disturbing factor is image blurring, both due to partial-volume-effects and (periodic) movements such as breathing. However, the subgroups of lesions least influenced by both causes of blurring (i.e., tumor volumes at least 5 times the scanners spatial resolution) showed similar results to the whole-group analysis, which demonstrates the limited role of these perturbing factors on our results.

6.5. Conclusion

Regions of tumors with highest MR_{glc} are characterized by high cellular uptake and phosphorylation rate constants with relatively low blood volume fractions. In regions with less metabolic activity, the blood volume fraction gradually increases and cellular uptake, washout and phosphorylation rate constants decrease. These results are not due to covariance of the regression coefficients and might be relevant for understanding tumor biology and for dose-painting in radiotherapy.

6.6. Acknowledgement

We would like to thank Siemens Molecular Imaging for providing the software, and specifically X.B. Pan and J. Declerck for commenting on the manuscript.

7a. Shortened Dynamic ^{18}F-FDG PET

Jonathan A. Disselhorst[1], Dennis Vriens[1], Lioe-Fee de Geus-Oei[1], Wim J.G. Oyen[1] and Eric P. Visser[1]

[1] Department of Nuclear Medicine, Radboud University Nijmegen Medical Centre, Nijmegen, The Netherlands

Reprinted by permission of the Society of Nuclear Medicine from: J Nucl Med. 2011;52:1330

TO THE EDITOR: With great interest we read a recent article by Strauss *et al.* [42]. The authors describe a support vector machine-based method to predict the parameters of the 2-tissue compartment model from shortened dynamic ^{18}F-FDG PET acquisitions by analyzing a large database of 1,474 time-activity curves obtained from 539 patients. Shortening the standard 1-h protocol to more convenient acquisition times of less than 30 min would not only improve patient comfort but also reduce demand on camera time and facilitate scheduling of dynamic scans. In this manner, the likelihood that dynamic PET will actually be used for routine imaging purposes would increase. The authors have shown that their method can accurately estimate tumor microparameters using a short dynamic ^{18}F-FDG PET scan. However, we wish to suggest additional analyses.

Accumulation of ^{18}F-FDG in a tumor increases with time. Hamberg *et al.* [235] have shown a continuing rise in standardized uptake value in some lung tumors even several hours post injection. With decreasing blood concentrations, the tumor-to-background ratio continues to increase, but conversely, the decreasing counting rates as a result of the physical decay of ^{18}F dictate an upper limit to the optimal uptake period. Most optimized protocols advise that acquisition of static PET scans begin at least 45 min after administration of ^{18}F-FDG [12,13], and many centers use an uptake period of about 60 min.

Volumes-of-interest (VOIs) to assess uptake or pharmacokinetic parameters are often defined on a threshold basis, such as the 3-dimensional isocontour at 50% of the maximum voxel value within a lesion. Other methods include manually placed VOIs or fixed volumes. These methods have variable advantages and limitations, but all have in common that voxels included in the VOI defined at an earlier time point may differ from those defined in the final time frame. Also, with manually placed VOIs it may be difficult to accurately delineate the lesion, as the contrast is still relatively low at an earlier time point. Consequently, the lesion's time-activity curve can differ as well, which, in turn, could alter the parameters of the 2-tissue compartment model.

In our experience, the VOI often differs significantly depending on time after injection. The Jaccard index [236] can be used to determine the similarity between 2 VOIs, defined as the number of overlapping voxels divided by the number of voxels in both or any of the VOIs. Comparing VOIs defined in early time frames and the final time frame shows a gradually decreasing similarity. Especially with scans of less than 30 min, the index can become relatively low, because of insufficiently high tumor-to-background ratios. Obviously, with a short dynamic PET acquisition and an additional time frame at 60 min after injection, as also described by Strauss *et al.*, accurate VOI definition is no longer a problem as long as both scans can be registered properly. However, the benefits of a shortened acquisition period would be reduced.

Strauss *et al.* appear to have shortened the dynamic PET scan by removing time points from the original time-activity curves, without redefining the VOIs in the earlier time frames—at least this is not mentioned in their paper. We would be interested in the combined effect of redefining VOIs on the shortened acquisition and the significantly shorter time-activity curve. When the parameters of the 2-tissue compartment model can still be estimated with great accuracy, shortened dynamic PET acquisitions could be a valuable addition to standard, static, ^{18}F-FDG PET.

7b. Volume of interest definition of tumors in dynamic ^{18}F-FDG PET images

Jonathan A. Disselhorst[1], Lioe-Fee de Geus-Oei[1], Dennis Vriens[1], Dimitris Visvikis[2], Cornelis H. Slump[3], Wim J.G. Oyen[1] and Eric P. Visser[1]

[1] Department of Nuclear Medicine, Radboud University Nijmegen Medical Centre, Nijmegen, The Netherlands

[2] LaTIM, INSERM U650, CHU Morvan, Brest, France

[3] Institute of Technical Medicine, University of Twente, Enschede, The Netherlands

Submitted

Abstract

Dynamic ^{18}F-FDG PET scans in oncology often take about one hour to acquire, which interferes with routine clinical application. Several attempts have been made to shorten the duration of these scans. One important, often neglected, aspect is volume of interest (VOI) definition of tumors in shortened scans. In this study we consider its influence in the analysis of shortened dynamic ^{18}F-FDG PET scans.

Methods. Different methods were used to define the VOI in dynamic ^{18}F-FDG PET scans of 15 patients. The VOIs were defined on each of the last 11 (5-minute duration) time frames of a 60 min scan. Concordance between the VOIs was calculated and the effect of the VOI on the tumor pharmacokinetic parameters obtained with compartment modeling and Patlak analysis was determined.

Results. Based on the effect of VOI definition alone, dynamic PET acquisitions can be shortened to about 30 minutes. Shortening acquisition times even further would considerably alter outcome parameters.

Conclusion. VOI definition has a major effect when a dynamic PET acquisition is shortened.

7b.1. Introduction

Accurate tumor delineation is important for quantification in ^{18}F-FDG PET. Volumes of interest (VOIs) should be reproducible and representative for the lesion. Moreover, the volume of the VOI should be in agreement with pathology. This is of special importance in radiotherapy planning, when PET images are used to determine the gross tumor volume (GTV). The same requirements are valid in dynamic PET studies, where the lesion should remain in the VOI for the entirety of the scan. In order to accurately determine pharmacokinetic properties in a lesion, these dynamic acquisitions often take 60 minutes. Such long acquisition times hamper routine clinical application of dynamic PET because of the high demand on camera time, and because it is uncomfortable for the patient to lie still on the scan-bed for an hour. The latter also increases the chance of unintentional patient movement.

In several studies it has been attempted to shorten the duration of dynamic ^{18}F-FDG PET scans [39-42]. The emphasis in many of these studies was put on the effect of the reduced number of time points, i.e., shorter duration of the time activity curves. Reasonably accurate results from pharmacokinetic analysis can be obtained from the shorter acquisition. The influence of VOI definition on shortened dynamic ^{18}F-FDG PET, however, has largely been ignored. Some methods utilize two scans at separate time points (e.g., [40]). In this manner, the VOI has no significant influence, provided that the two scans can be properly aligned. To perform two separate scans, however, is inconvenient in terms of logistics.

Optimal scan-protocols for static ^{18}F-FDG PET acquisitions dictate an uptake period between ^{18}F-FDG administration and scanning of at least 45 min [12], but preferably 60 min [13]. The main reason for this is that it takes time for tissues to accumulate ^{18}F-FDG and to obtain a sufficiently high contrast to distinguish lesions. Scanning at much later time points will result in additional noise due to a decrease of count rates as a result of physical decay of ^{18}F. This reveals a dilemma in shortened dynamic ^{18}F-FDG PET acquisitions; As the VOIs for analyses are generally defined in the final time frame of the dynamic PET scan, it may not be straightforward to delineate the lesion using a shortened acquisition period. It may result in differently shaped and sized VOIs and consequently a different time activity curve. The phenomenon alone could alter the results of the pharmacokinetic analysis, apart from the effect of the reduced number of data points. To prevent this, it should be possible to define the same VOIs in the different time frames of a dynamic PET scan.

In this study, several methods to define the VOI have been used on dynamic ^{18}F-FDG PET scans in order to analyse the variability of the VOI over time, and to indicate limits imposed by VOI definition alone, for shortening dynamic acquisitions. The full 60 min dynamic acquisition was used to obtain pharmacokinetic parameters by compartment modeling and Patlak analysis, only the VOI was defined in different time frames.

7b.2. Materials and methods

7b.2.1. Patients and image acquisition

Twenty patients with operable, non small cell lung carcinoma (NSCLC) of at least 30 mm in diameter on computed tomography (CT) images, were included. Only patients who had not received prior anticancer treatment and patients without diabetes mellitus were included. The study was approved by the Institutional Review Board and written informed consent was obtained from each patient. Patients fasted for at least 6 h prior to imaging.

Dynamic PET acquisition were performed for 60 min on a Biograph Duo [209] scanner (Siemens Healthcare) in a single bed position (159 mm axial length) after intravenous injection of, on

average, 3.3 MBq/kg body weight. A low-dose CT acquisition preceded the PET scan and was used for attenuation correction and anatomical reference.

PET data were reconstructed using a 35-frame protocol (10 s delay after ^{18}F-FDG injection, 16 × 5, 3 × 20, 5 × 30, 11 × 300 s). Reconstructions were performed with ordered subsets expectation maximization in two dimensions (OSEM2D) in 4 iterations with 16 subsets in a 256 × 256 × 53 image matrix (voxel size: 2.65 × 2.65 × 3.00 mm^3) with a 5 mm full-width at half maximum (FWHM) 3D Gaussian filter. Randoms, scatter, attenuation and decay correction were applied. Apart from periodic movements (e.g., breathing), 15 patients did not move during acquisition of the dynamic PET scans, of whom details are presented in *table 1*. The other patients (n=5) have been excluded because of small movements during the scan. No motion correction technique have been used because the influence of these methods on pharmacokinetic modeling is unknown.

7b.2.2. Volume of Interest Definition

To obtain a blood input function, a VOI was drawn manually in the ascending aorta on the summed first 12 time frames (1 min total duration). For the tumor time activity curve, different methods for VOI definition were used, as described below. In each of the last 11 time frames (5 – 60 min post injection) a VOI was drawn using the methods described below. To prevent that non-tumor high-uptake tissues were inadvertently added to the VOI (myocardium, liver), most of the image matrix was masked except from a region well around the tumor. Definition of VOIs was performed in MATLAB (version R2008a; The MathWorks, Natick (MA), USA) unless stated otherwise. The background activity concentration was determined from a manually drawn VOI in healthy lung tissue.

1. Fixed volume. A spherical VOI with a diameter of about 15 mm (81 voxels in total) was placed in the lesion, such that the average voxel value within the VOI was maximal. This method will be denoted by VOI_{15mm}. Next to that, the maximum voxel in the lesion was used, a method indicated by VOI_{max}.
2. Fixed relative threshold. All voxels with a value larger than, or equal to a percentage of the maximum value within the lesion are included in the VOI. In this study 50% and 70% were used as thresholds, indicated by $VOI_{50\%}$ and $VOI_{70\%}$, respectively. The same procedure was used after subtraction of the average background activity concentration, these methods will be indicated by $VOI_{B50\%}$ and $VOI_{B70\%}$, respectively.
3. Adaptive relative threshold. Using an iterative procedure as described by van Dalen *et al.* [135], the optimal threshold to obtain the most accurate tumor volume was found for each lesion, in each time frame individually. This method takes the point spread function (PSF) of the scanner and the background activity into account, the method will be indicated by VOI_{RTL}. An isotropic 3D Gaussian with full-width at half maximum (FWHM) of 6.1 mm [209] was used for the PSF.

Table 7b.1: Patient characteristics (n=15)

	Value ± SD	Range
Mean age [y]	63 ± 10	44 – 78
Proportion male [%]	67	
Mean plasma glucose level [mmol/L]	5.6 ± 1.0	4.5 – 7.7
Mean body weight [kg]	78 ± 16	47 – 104
Mean administered activity per unit body mass [MBq/kg]	3.3 ± 0.5	2.6 – 4.3

4. Fuzzy c-means (FCM). The FCM algorithm as described by Bezdec [136] was used with 3 clusters. In an iterative process, voxel membership to all clusters is calculated based on distance to cluster mean. The cluster with the highest mean activity was used for the analyses. This method will be denoted by VOI_{FCM}.
5. Otsu method. A background and foreground (or tumor) class is defined, and voxel assignment is based on a threshold. This threshold is chosen in such a way that the variance in voxels within each class is the lowest. The method has been described by Otsu [237], and will be referred to as VOI_{Otsu}.
6. Fuzzy locally adaptive Bayesian (FLAB). The 3-FLAB and 2-FLAB algorithm as described by Hatt *et al.* [137,138] implemented in a dedicated program were used to define VOIs. The image was segmented into three and two classes, respectively. FLAB is an iterative procedure to segment a lesion, taking into account spatial correlations between voxels, voxel intensities, and variance. The segmented results were processed with MATLAB. The methods will be denoted by VOI_{FLAB2} and VOI_{FLAB3}. Both VOIs correspond to the class with the highest mean activity.

7b.2.3. Pharmacokinetic analyses

For the pharmacokinetic analyses, full one-hour time activity curves were used. These curves were obtained from the VOIs defined in each of the last eleven time frames. This was done to evaluate the effect of VOI definition alone, rather than this effect combined with shortened time-activity curves.

The influx constant (K_i) was determined with Patlak analysis [121] using the last 8 time frames (20–60 min) for linear regression. The microparameters of the two-tissue compartment model were determined with the Levenberg-Marquardt [217] non-linear least squares (NLLS) algorithm. Irreversible uptake (trapping) of ^{18}F-FDG in tissue was assumed in both analyzes, i.e., absence of ^{18}F-FDG-6-PO_4 dephosphorylation, or k_4.

7b.2.4. Data analysis

To compare the VOIs determined in each dynamic acquisition, the Jaccard [236] concordance index (CI) was determined, the tumor volumes (number of voxels) were compared, and the VOI effects on the tumor microparameters and influx constant were evaluated.

CI is defined as the number of voxels in the intersection, divided by the number of voxels in the union of two VOIs:

$$CI_n = \frac{VOI_n \cap VOI_{ref}}{VOI_n \cup VOI_{ref}} \quad (1)$$

Where VOI_{ref} stands for the VOI in the reference time frame *ref*, which is the final frame (55–60 min after injection), and VOI_n is the VOI in each time frame n of the dynamic scan. CI can vary between 0 (no overlapping voxels) and 1 (complete overlap of the two VOIs).

In this study, the differences that arose from the definition of VOIs at earlier time points are relevant, not the between-patient variation. Hence, the relative differences in volume and the pharmacokinetic parameters of frame n with respect to frame *ref* were determined. The error in the volume and pharmacokinetic parameters was expressed as ΔP_n:

$$\Delta P_n = \frac{P_n - P_{ref}}{P_{ref}} \quad (2)$$

Where P is any of the five pharmacokinetic parameters (K_1, k_2, k_3, V_b, or the influx constant), or the total volume of the VOI.

7b.2.5. Statistical analysis

We tested the minimum scan duration for a dynamic ^{18}F-FDG PET acquisition without altering the volumetric or pharmacokinetic parameters, exclusively based on VOI definition. As indicated above, the volumetric and pharmacokinetic parameters obtained in each time frame were compared to the parameters obtained in the final time frame. The statistical analysis was then performed using each individual time frame compared to the next-to-last time frame using the Wilcoxon rank sum test [238]. The cut-off point for statistical significance was set at $p = 0.01$. The next-to-last time frame was chosen because in the final frame CI is, per definition, equal to one and ΔP equals zero, and on account of noise; the shorter uptake period and corresponding lower contrast are not the exclusive source of differences in the VOIs between early and late time frames. Due to the random nature of radioactive decay and the finite number of coincidences per time frame, dissimilarities can be explained to some extent by image variations as a result of noise. Such differences should not be the restriction for the introduction of shortened dynamic PET. This noise effect is greatly reduced by analyzing the data with respect to the next-to-last time frame, since the real differences between these last two time frames (e.g., a difference in tumor to background ratio) are assumed to be small and the differences can mainly be explained by noise.

7b.3. Results

In *figure 1*, the CIs for the different VOI definition methods are shown. Clearly, CI is lower at earlier time frames. Furthermore, it appears that many different VOI definition methods lead to similar CIs, except VOI_{max}, VOI_{15mm}, $VOI_{70\%}$, and $VOI_{B70\%}$. These four methods can be classified as the smallest according to total volume. VOI_{Otsu} and VOI_{FLAB2} can be classified as large, and $VOI_{50\%}$, $VOI_{B50\%}$, VOI_{FCM}, and VOI_{FLAB3} as intermediate in size. In *figure 2*, CIs are shown, as well as the absolute value of the relative difference in tumor volume, both for $VOI_{50\%}$ alone. Statistically significant differences from the next-to-last frame are indicated in this figure with a single asterisk (*) for $p \leq 0.05$ and double asterisk (**) for $p \leq 0.01$. The figure indicates that VOIs defined on dynamic PET studies shortened to 30 min or less are significantly different from those defined on 60 min scans. *Figure 3* shows the pharmacokinetic parameters, expressed as the absolute value of the relative difference from the final time frame. Because V_b showed large variations without a clear trend, this parameter is not included in the figure. Most parameters measured using a VOI defined in an early time frame deviate significantly from the values measured at 60 min after injection. For instance, the influx constant deviates 7% on average when the scantime is

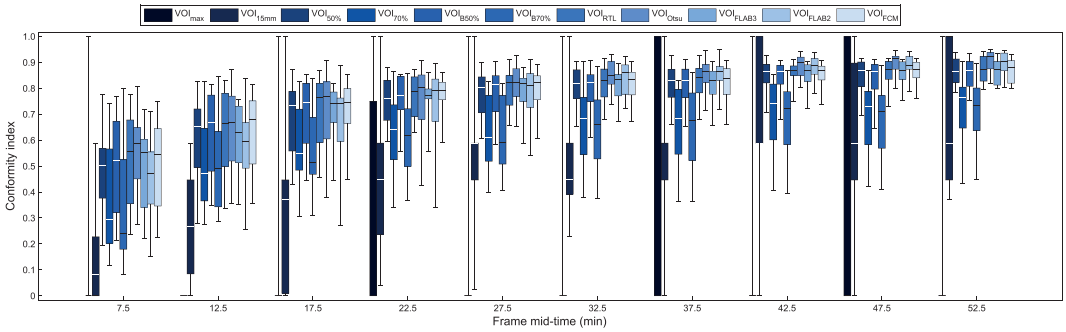

Figure 7b.1: Concordance index of VOIs in each time frame with the VOI in the final time frame as the reference for eleven different VOI techniques. The box shows the lower and upper quartile and the median. The whiskers show the most extreme values. No box or whiskers are shown at 12.5 min for VOI_{max}, because the CI for all patients was 0.

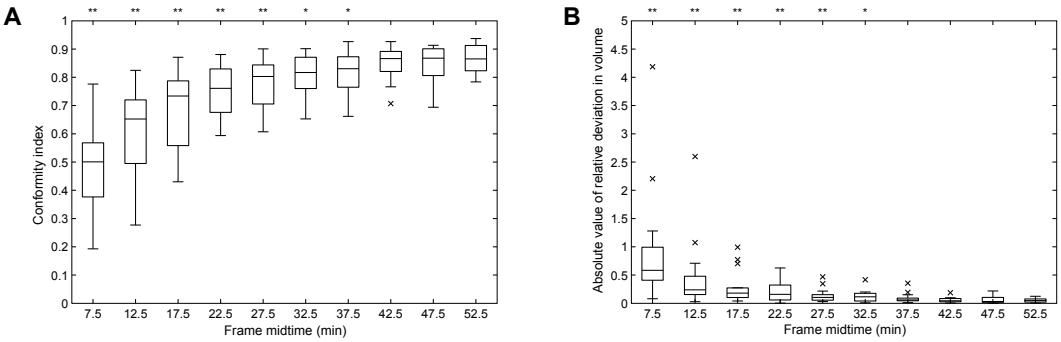

Figure 7b.2: Volumetric parameters for $VOI_{50\%}$. Time frames that yield parameters statistically different from the next-to-last are indicated with * ($p \leq 0.05$) and ** ($p \leq 0.01$) (upper horizontal axis). (A) Concordance index of VOIs in each time frame and the final time frame as the reference; (B) Absolute value of the relative difference in volume with respect to the last time frame. The box shows the lower and upper quartile and median. The whiskers show the most extreme values within 1.5 times the interquartile range from the box. Outliers beyond the end of the whisker are shown as crosses.

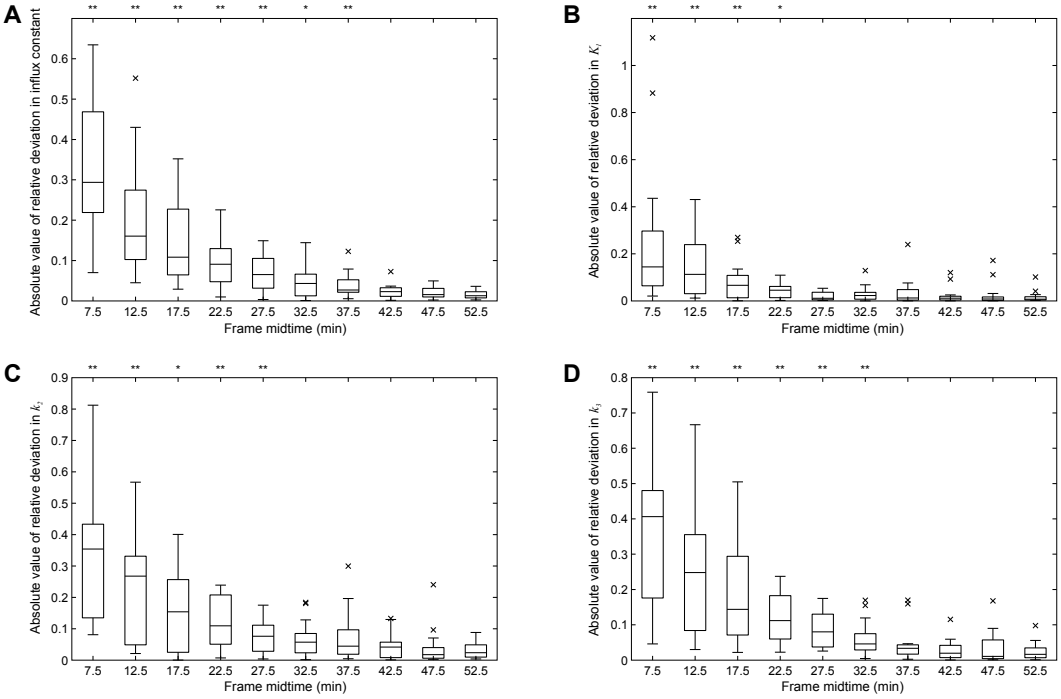

Figure 7b.3: Pharmacokinetic parameters for $VOI_{50\%}$. Time frames that are statistically different from the next-to-last are indicated with * ($p \leq 0.05$) and ** ($p \leq 0.01$) (upper horizontal axis). (A) Influx constant; (B) K_1; (C) k_2; (D) k_3; The box shows the lower and upper quartile and median. The whiskers show the most extreme values within 1.5 times the interquartile range from the box. Outliers beyond the end of the whisker are shown as crosses. All values are given as an absolute value of the relative deviation from the final time frame.

reduced to 30 min. This deviation is 10% at 25 min, 15% at 20 min and 21% at 15 min. Similar values were observed for k_2 and k_3. For K_1, these values are lower, and the deviation became significant at a scan time of 20 min. Also the between-patient variation at earlier time points is larger, indicating that these deviations are not only systematic, which would mean they could simply be corrected with a correction factor.

Considering the relative change in the parameters, without taking its absolute value, we observe a significant decrease in the influx constant and k_3, and a significant increase in total tumor volume. The relative change in K_1, k_2 and V_b is not significant (results not shown). On average, the small VOIs, as compared to the large VOIs, lead to a larger influx constant, lower CI and larger k_3.

7b.4. Discussion

The purpose of this study was to show the effect of the VOI alone on shortened dynamic scans rather than to indicate the most appropriate VOI definition method in terms of an accurate GTV or most representative for the tumor. Therefore, a selection of the many existing VOI definition techniques was examined. Figure 1 clearly showed the lowest CIs for the four smallest VOIs (in volume). Smaller VOIs give less favourable results than larger ones, i.e., a small change in a small VOI has a relatively large effect on CI, as compared to large VOIs. The tumors included in this study were relatively large with a diameter of at least 3 cm. Therefore, differences in VOI location or size among time frames are expected to have a smaller effect on volumetric and pharmacokinetic parameters than in smaller tumors. Also, lung tumors may give a too favourable representation of shortened dynamic PET, because of their generally high tumor-to-background ratios as compared to tumors in organs such as the liver or the brain.

The pharmacokinetic analyses have been performed with the full 60 minutes of scan data. This was explicitly done to separate the effect of the VOI from the effect of a shortened time activity curve, but also because standard NLLS algorithms such as Levenberg-Marquardt have difficulties with short dynamic series [42]. The framing schedule that has been used is somewhat unconventional, with 5-min frames for nearly the entire scan. The first minutes of the scan, however, have been framed with a high temporal resolution. This ensures that the first passage of radioactivity in the blood through the aorta and tumor, or the "blood peak" is captured accurately, which is required for valid microparameter values. Furthermore, the framing is not very critical for the Patlak analyses since especially the integral of the blood input function is important, which is not fundamentally different with another framing schedule.

Some of the iterative VOI definition methods that use random start points (e.g., FLAB) can converge to a local optimum, and for that reason yield a slightly different VOI in subsequent runs with the same image data. Because this is a randomly occurring effect, it has no significant influence on the conclusions.

For the purpose of therapy response monitoring, small changes between a baseline and follow-up scan suggesting response, could be obscured by a larger variation when a shortened dynamic PET protocol is used. However in our study, based on VOI definition alone, we did not find significant differences comparing the whole 60 min scan to a shortened scan with a duration of 30 min or more.

7b.5. Conclusion

The results of the present study indicate that a dynamic PET acquisition should not be shorter than 30 minutes. This is based on the effect of VOI definition alone; with shorter acquisitions, the VOI is significantly altered and with it the measured tumor microparameters. The

influence of VOI definition on pharmacokinetic parameters in shortened dynamic PET scans is often disregarded, but should be considered in future studies.

7b.6. Acknowledgement

The authors would like thank Dr. Jérôme Declerck and Dr. Thomas Wright of Siemens Molecular Imaging for providing the pharmacokinetic modeling software.

8a. Summary and future perspectives

8a.1. Summary

In this thesis several aspects related to the quantification of dynamic positron emission tomography (PET) are discussed, and the quantification of small-animal PET scanners. Some of these relate to characterization and optimization of the scanner and the scanner settings. This is important for dynamic but also static PET acquisitions. Optimized settings can improve the quality of the images, which allows for more accurate quantification. Obtaining a good understanding of the possibilities and impossibilities of the scanner, enables investigators to design better study protocols.

The influence of the radionuclide on the image quality is evaluated in *chapter 2*, using the NEMA NU 4 [10] phantom and the Siemens Inveon PET scanner. Four different positron emitters are compared: ^{18}F, ^{68}Ga, ^{89}Zr and ^{124}I. Particularly differences in positron range and the presence of additional gamma emissions can have an effect on image quality. Image quality can be assessed in the NU 4 phantom using three distinct regions. Noise can be assessed in a region with a uniform activity distribution, two compartments without activity provide the spillover (the measured activity in a region with no real activity). Finally, there is a region in which the recovery coefficient (RC) can be determined. The RC indicates how well small objects can be detected by the scanner. The influence of the additional gamma emissions on the three quality parameters is limited. However, it is clear that the larger positron range of ^{68}Ga and ^{124}I affects the resolution of the images, and causes a reduction in RC. Also larger spillover ratios are observed in these two radionuclides. In short, when a PET scanner is used with a resolution of ±1.5 mm (similar to the Inveon), the choice of radionuclides with a high positron range can form a limiting factor for observing small objects. Selecting an optimal reconstruction algorithm can improve image quality for all four radionuclides remarkably.

Chapter 3 discusses the resolution and sensitivity of the Inveon. The scanner is characterized by a high resolution and sensitivity. The latter can largely be attributed to the large aspect ratio (the axial length of the scanner relative to the detector ring diameter). A uniform resolution throughout the field of view (FOV) can be obtained by using 3D reconstruction, and including a resolution model of the scanner. These features of the scanner can be included in the design of PET studies. In this case, with a small-animal PET scanner, to consider, for example, scanning multiple animals simultaneously.

Because of the wide variety of reconstruction algorithms and their settings, it is not immediately obvious how the PET images can best be reconstructed. The influence of the reconstruction settings are studied in *chapter 4*, and optimal settings are determined for each algorithm. The differences in image quality are assessed using the NEMA NU 4 phantom.

The second part of this thesis focuses specifically on dynamic PET. Again, improvements can be achieved through optimizations, such as in the framing of a dynamic scan. In addition, it covers a practical application of dynamic PET, in which more information can be obtained about tumors. More details about tumor behavior can be observed using dynamic PET than with a static acquisition. Finally, whether the acquisition time of a dynamic PET scan can be reduced is studied.

In *chapter 5*, the framing of dynamic PET scans is examined. There is no consensus in literature on the optimal division in time frames of dynamic PET acquisitions. As a result, there is a great variation in framing schedules between different dynamic PET studies. A large number of PET scans of tumors were simulated with different characteristics (the tumor microparameters) by means of computer simulations. Different framing methods were then tested, where noise was added based on the length of the frames and the simulated activity concentration. Subsequently, the microparameters were estimated. An optimal framing schedule provides the smallest possible difference between the simulated and estimated microparameters. An optimal schedule has

short frames in the beginning of the scan (approximately 4–6 seconds), and a total of at least 40, but preferably even more frames. The increased noise levels deteriorate the results when shorter frames are used in the beginning of the scan, while with longer frames, the temporal resolution is not high enough for accurate estimation. The framing clearly has a major influence on the accuracy of a dynamic scan, and is therefore important to optimize.

An application of dynamic PET is described in *chapter 6*. Because dynamic PET images have relatively high noise levels, analyses cannot always be performed at the level of individual voxels. Therefore, a larger area of interest is often considered, comprising many voxels. The result is an average, so that any differences within the region remain unknown. However, these differences do exist within tumors. By dividing the tumor into three areas with a decreasing metabolic activity (MR_{glc}), tumor heterogeneity can be observed to some extent without the need for the analysis of individual voxels. The analysis reveals that tumor regions with a high MR_{glc} are characterized by a higher uptake and phosphorylation of ^{18}F-FDG, but lower blood fraction.

It usually takes one hour to acquire a dynamic scan, but this is uncomfortable for the patient besides being logistically unattractive. It would be an advantage if the scan time could be shortened. However, most important is that this does not compromise the reliability of the results. In many cases, only the effect of the reduced amount of data on the results is considered. Whether the tumor can still be distinguished adequately from the background in the shorter scan is often disregarded. Correct tumor delineation in short dynamic PET scans was therefore studied specifically, this is described in *chapter 7*. The study shows that the tumor region can be defined less accurately when the scan time is reduced.

8a.2. Future perspectives

Dynamic PET is not routinely used in the clinic, and limited mainly to scientific applications. As many possible settings should be optimized for the successful implementation of dynamic PET for diagnosis. A number of these have been described in this thesis. In addition, the added value of dynamic scanning should be demonstrated, that clearly outweighs the relatively complex procedure.

The importance of imaging is increasing, also in preclinical research. Small-animal PET scanners are therefore used increasingly. The technique and operation of these scanners is not substantially different from clinical scanners, but they usually have other properties such as a higher resolution. A large positron range, for example, will therefore have an effect on image quality in these scanners rather than clinical scanners.

New techniques for acquisition or reconstruction of PET images are introduced continuously. It is interesting to study whether their benefits also apply for dynamic PET reconstructions. Until 4D reconstruction algorithms have become commonplace, such refinements may still contribute to a higher accuracy of dynamic PET. Modeling the positron range within the maximum a posteriori (MAP) algorithm [159,239] is another reconstruction improvement. The detrimental effect of a high positron range on the resolution can be corrected to a certain extent. It seems to be a promising technique, but it still needs to be refined. Time-of-flight, another innovation available in modern PET scanners, could be particularly interesting in situations of low-counting statistics, such as dynamic PET. The value, however, should be investigated in further studies.

Chapter 5 presents results of a simulation study to obtain an optimal framing schedule in dynamic PET. In this case, a fixed infusion protocol was used, as were the noise characteristics of the scanner. An extension to this question could be the simultaneous optimization of the framing schedule and infusion protocol. A different infusion could possibly further increase the accuracy of the results. In addition, other refinements of this method could be investigated such as

inclusion of k_4 in the compartment model, introducing heterogeneity in the simulated tumors, dispersion in the input curve or an imperfect input function (e.g., caused by partial volume effects and spillover when the input function is obtained from the left ventricle). In addition, also to *chapter 7*, an optimal framing schedule could be developed for a shortened dynamic scan. Also the minimal acceptable scan time could be studied.

The results presented in *chapter 6* on the heterogeneity within tumors were obtained with a relatively old scanner (ECAT EXACT). The resolution and sensitivity of this scanner are remarkably lower than scanners currently on the market. Although interesting conclusions can be drawn from the current results, a study using modern equipment may lead to new insights. Instead of three areas defined based on descending MR_{glc}, individual voxel-based analysis may be possible. Metabolic heterogeneity within the tumor could then be observed in more detail. It would be particularly interesting when this could be linked to the actual biological situation. The tumor could, after surgical resection, be analyzed immunohistochemically for parameters such as glucose transporters and hexokinase. The evidence that the various tumor microparameters are related to the expression of both is strong [240], but this has only been established on a whole-tumor basis. Especially the heterogeneous distribution can be interesting for diagnosis or prediction of therapy outcome.

8b. Samenvatting en toekomstperspectief

8b.1. Samenvatting

In dit proefschrift worden een aantal aspecten gerelateerd aan de kwantificatie van dynamische positron emissie tomografie (PET) behandeld, en kwantificatie van PET-scanners voor proefdieren. Sommigen hiervan hebben betrekking op het karakteriseren en optimaliseren van de scanner en de scanner instellingen. Dit is van belang voor dynamische, maar ook voor statische PET acquisities. Door optimalisatie van instellingen kan de kwaliteit van de beelden verbeteren, waarmee nauwkeuriger kwantificatie mogelijk wordt. Door een goed beeld van de mogelijkheden en onmogelijkheden van de scanner te verkrijgen, is een onderzoeker in staat betere onderzoeksplannen op te stellen.

In *hoofdstuk 2* wordt de invloed van het radionuclide op de beeldkwaliteit onderzocht, gebruik makend van het NEMA NU 4 fantoom [10] en de Siemens Inveon PET scanner. Vier verschillende positron emitters zijn vergeleken: ^{18}F, ^{68}Ga, ^{89}Zr en ^{124}I. Met name de verschillen in positrondracht en eventuele aanwezigheid van extra gamma straling kunnen een effect hebben op de beeldkwaliteit. Het NU 4 fantoom biedt de mogelijkheid om beeldkwaliteit te beoordelen aan de hand van drie verschillende regio's. Ruis kan beoordeeld worden in een regio met een uniforme activiteitsverdeling, twee compartimenten zonder activiteit geven de *spillover* (gemeten activiteit in een regio zonder werkelijke activiteit). Als laatste is er een regio waarin de *recovery coefficient* (RC) bepaald kan worden. De RC geeft aan hoe goed kleine objecten waargenomen kunnen worden door de scanner. De invloed van extra gamma straling op de drie kwaliteitsparameters is beperkt. Wel wordt duidelijk dat de grotere positrondracht van ^{68}Ga en ^{124}I invloed heeft op de resolutie van de beelden, en zorgt voor een verlaging van de RC. Ook wordt er bij deze twee radionucliden een grotere *spillover* waargenomen. Kortom, bij het gebruik van een scanner met een resolutie $\pm$1.5 mm (zoals de Inveon) kan de keuze van een radionuclide met hoge positrondracht een beperkende factor gaan vormen voor het waarnemen van kleine objecten. Hierop is het gebruikte reconstructie algoritme ook van invloed. De juiste keuze hierin kan voor alle vier de radionucliden een grote kwaliteitsverbetering opleveren.

Hoofdstuk 3 behandelt de resolutie en gevoeligheid van de Inveon. De scanner wordt gekenmerkt door een hoge resolutie en gevoeligheid. Dat laatste is voor een groot deel toe te schrijven aan de grote aspect ratio (de axiale lengte van de scanner ten opzichte van de detector ring diameter). Door gebruik te maken van een resolutie model en 3D reconstructie is een uniforme resolutie binnen het gehele *field of view* (FOV) te verkrijgen. Deze scanner eigenschappen kunnen gebruikt worden bij het ontwerpen van PET studies. In dit geval, met een PET scanner voor proefdieren, is bijvoorbeeld te overwegen om meerdere dieren tegelijk te scannen.

Door de grote variëteit in reconstructie algoritmes en bijbehorende instellingen ligt het niet voor de hand hoe PET beelden het beste te reconstrueren zijn. In *hoofdstuk 4* wordt de invloed van de instellingen onderzocht, en worden optimale instellingen bepaald voor elk algoritme. Opnieuw met behulp van het NU 4 fantoom worden verschillen in beeldkwaliteit beoordeeld.

Het tweede deel van dit proefschrift heeft specifiek betrekking op dynamische PET. Ook hier zijn verbeteringen mogelijk door optimalisaties, bijvoorbeeld in de framing van een dynamische scan. Daarnaast wordt gekeken naar een praktische toepassing van dynamische PET, waarin meer informatie kan worden verkregen over een tumor. Er komen hierbij meer details over het gedrag van de tumor naar voren dan waargenomen kunnen worden met een statische opname. Tenslotte wordt onderzocht of de acquisitietijd van een dynamische PET scan verkort kan worden.

In *hoofdstuk 5* wordt de framing van dynamische PET scans onderzocht. In de literatuur is geen overeenstemming over de optimale manier waarin een dynamische PET scan in tijd frames verdeeld moet worden. Hierdoor is er een grote variatie in framingschema's tussen verschillende dynamische PET onderzoeken. Met computer simulaties werden een groot aantal PET scans van

tumoren gesimuleerd met verschillen in eigenschappen (de tumor microparameters). Vervolgens werden verschillende manieren van framing getest, waarbij ruis werd toegevoegd op basis van de lengte van de frames en de gesimuleerde activiteitsconcentratie. Hierna werden de microparameters geschat. Een optimaal framingschema levert een zo klein mogelijk verschil tussen de gesimuleerde en geschatte microparameters. Een optimaal schema heeft korte frames in het begin van de scan (ongeveer 4–6 seconden), en in totaal tenminste 40, maar bij voorkeur zelfs meer frames. Bij het gebruik van kortere frames in het begin van de scan verslechtert de toegenomen ruis de resultaten, bij langere frames is de temporele resolutie onvoldoende hoog voor een nauwkeurige schatting. Duidelijk wordt dat de framing een grote invloed heeft op de nauwkeurigheid van een dynamische scan, en het dus van belang is om te optimaliseren.

Een toepassing van dynamische PET wordt beschreven in *hoofdstuk 6*. Omdat dynamische PET beelden relatief veel ruis kunnen bevatten, kunnen de analyses niet altijd op het niveau van individuele voxels worden uitgevoerd. Daarom wordt vaak een groter interesse gebied beschouwd, bestaande uit vele voxels. De uitkomst is een gemiddelde, waardoor eventuele verschillen binnen de regio verborgen blijven. Deze verschillen bestaan echter wil binnen tumoren. Door de tumor op te delen in drie gebieden met een aflopende metabole activiteit (MR_{glc}) kan tumor heterogeniteit tot op zekere hoogte waargenomen worden zonder dat hiervoor individuele voxels geanalyseerd worden. Uit de analyses komt naar voren dat tumor regio's met een hoge MR_{glc} gekenmerkt worden door een hogere opname en fosforylatie van ^{18}F-FDG, maar lager bloedvolume.

Normaal gesproken duurt een scan een uur, maar dit is naast onaangenaam voor de patiënt ook logistiek onaantrekkelijk. Het is dus een voordeel als de scanduur verkort kan worden. Het is echter wel van belang dat dit niet ten koste gaat van de betrouwbaarheid van de resultaten. In veel gevallen wordt alleen beoordeeld of verminderde hoeveelheid data nog tot dezelfde resultaten leidt. Of de tumor nog wel voldoende te onderscheiden is van de achtergrond op de kortere scan wordt hierbij vaak buiten beschouwing gelaten. Derhalve werd correcte tumordeliniatie in verkorte dynamische PET scans specifiek onderzocht, dit wordt beschreven in *hoofdstuk 7*. Uit dit onderzoek blijkt dat de tumorregio minder accuraat te definiëren is, bij het verkorten van de scanduur.

8b.2. Toekomstperspectief

Dynamische PET wordt in de kliniek nog niet routinematig toegepast, en beperkt zich voornamelijk tot wetenschappelijke toepassingsgebieden. Voor het succesvol gebruik van dynamische PET voor diagnostiek moeten zo veel mogelijk instellingen geoptimaliseerd zijn waarvan er in dit proefschrift een aantal zijn beschreven. Daarnaast moet een duidelijke meerwaarde van dynamisch scannen worden aangetoond, die opweegt tegen de relatief ingewikkelde procedure.

Het gebruik van imaging wordt steeds belangrijker, ook voor preklinisch onderzoek. PET scanners voor proefdieren worden daarmee ook steeds vaker gebruikt. De techniek van deze scanners is niet wezenlijk anders dan van klinische scanners, maar ze hebben meestal wel andere eigenschappen, zoals een hoge resolutie. Hierdoor kan een grote positrondracht bijvoorbeeld eerder een effect hebben op de beeldkwaliteit.

Er worden doorlopend nieuwe technieken geïntroduceerd voor de acquisitie of reconstructie van PET beelden, die mogelijk een verbetering opleveren. Het is interessant om te onderzoeken of dit ook voor dynamische PET reconstructies voordelen oplevert. Totdat volledige 4D reconstructie algoritmes gemeengoed zijn geworden, kunnen dergelijke verfijningen nog bijdragen aan een hogere nauwkeurigheid van dynamische PET. Een andere reconstructie verbetering is het modelleren van de positrondracht binnen het *maximum a posteriori* (MAP) algoritme [159,239], waardoor het resolutieverlagende effect van een hoge positrondracht tot op zekere hoogte gecorrigeerd kan worden. De techniek lijkt veelbelovend, maar moet nog wel verder verfijnd worden.

Ook een vernieuwing zoals *time-of-flight* dat op moderne PET scanners mogelijk is, kan juist in situaties met weinig tel statistiek, zoals bij dynamische PET acquisities, interessant worden. De waarde ervan dient echter in vervolg studies onderzocht te worden.

Hoofdstuk 5 beschrijft resultaten van een simulatiestudie naar de optimale framing in dynamische PET. In dit geval was het infusieprotocol een vast gegeven, net zoals de ruiseigenschappen van de scanner. Een uitbreiding op deze vraagstelling kan het gelijktijdig optimaliseren van het framingprotocol en de toediening van activiteit zijn. Mogelijk dat een andere toedieningsprotocol nog nauwkeuriger resultaten kan opleveren. Daarnaast kunnen andere verfijningen van deze methode onderzocht worden zoals het opnemen van k_4 in het compartiment model, het introduceren van heterogeniteit in de gesimuleerde tumoren, dispersie in de input curve of een imperfecte input functie als gevolg van bijvoorbeeld *partial volume* effecten en *spill-in* zoals bij gebruik van de linker ventrikel voor de input functie. Als aanvulling, mede ook op *hoofdstuk 7* is een optimaal framingprotocol te ontwikkelen voor een verkorte dynamische scan. Daarbij kan ook onderzocht worden wat de nog acceptabele minimale scan duur moet zijn.

De in *hoofdstuk 6* gepresenteerde resultaten over de heterogeniteit binnen tumoren zijn verkregen met een relatief oude scanner (ECAT EXACT). De resolutie en gevoeligheid van deze scanner zijn minder goed dan scanners die op dit moment op markt zijn. Hoewel al interessante conclusies getrokken kunnen worden met de huidige data, kan een studie die gebruik maakt van een modernere scanner mogelijk tot nieuwe inzichten leiden. In plaats van drie gebieden gedefinieerd op basis van aflopende MR_{glc}, kan voor analyse per voxel gekozen worden. Hiermee is heterogeniteit binnen de tumor nog beter waar te nemen. Het zou met name interessant zijn als een koppeling gemaakt kan worden met de werkelijke biologische situatie. Hiertoe zou de tumor, na chirurgische resectie, immunohistochemisch geanalyseerd kunnen worden op parameters zoals glucose transporters en hexokinase. De aanwijzingen dat de verschillende microparameters onder andere gerelateerd zijn aan de expressie van beiden zijn sterk [240], maar dit is bepaald voor een hele tumor. Juist de heterogene verdeling kan interessant zijn voor diagnostiek of voorspelling van therapie uitkomst.

9. References

1. Dimitrakopoulou-Strauss A, Strauss LG, Burger C, *et al*. Prognostic aspects of 18F-FDG PET kinetics in patients with metastatic colorectal carcinoma receiving FOLFOX chemotherapy. *J Nucl Med* 2004;45:1480–1487.
2. de Geus-Oei L-F, van der Heijden HFM, Visser EP, *et al*. Chemotherapy response evaluation with 18F-FDG PET in patients with non-small cell lung cancer. *J Nucl Med* 2007;48:1592–1598.
3. de Geus-Oei L-F, van Laarhoven HWM, Visser EP, *et al*. Chemotherapy response evaluation with FDG-PET in patients with colorectal cancer. *Ann Oncol* 2008;19:348–352.
4. Rudin M and Weissleder R. Molecular imaging in drug discovery and development. *Nat Rev Drug Discov* 2003;2:123–131.
5. Cunningham VJ, Gunn RN, and Matthews JC. Quantification in positron emission tomography for research in pharmacology and drug development. *Nucl Med Commun* 2004;25:643–646.
6. Chen DL, Ferkol TW, Mintun M a, *et al*. Quantifying pulmonary inflammation in cystic fibrosis with positron emission tomography. *Am J Resp Crit Care* 2006;173:1363–1369.
7. Burack MA, Hartlein J, Flores HP, *et al*. In vivo amyloid imaging in autopsy-confirmed Parkinson disease with dementia. *Neurology* 2010;74:77–84.
8. Isozaki M, Kiyono Y, Arai Y, *et al*. Feasibility of 62Cu-ATSM PET for evaluation of brain ischaemia and misery perfusion in patients with cerebrovascular disease. *Eur J Nucl Med Mol Imaging* 2011;38:1075–1082.
9. NEMA Standards Publication NU 2-2007: Performance Measurements of Positron Emission Tomographs. Rosslyn, VA: National Electrical Manufacturers Association (NEMA); 2007.
10. NEMA Standards Publication NU 4-2008: Performance Measurements for Small Animal Positron Emission Tomographs. Rosslyn, VA: National Electrical Manufacturers Association (NEMA); 2008.
11. Zanzonico P. Routine quality control of clinical nuclear medicine instrumentation: a brief review. *J Nucl Med* 2008;49:1114–1131.
12. Delbeke D, Coleman RE, Guiberteau MJ, *et al*. Procedure guideline for tumor imaging with 18F-FDG PET/CT 1.0. J Nucl Med 2006;47:885–895.
13. Boellaard R, O`Doherty MJ, Weber WA, *et al*. FDG PET and PET/CT: EANM procedure guidelines for tumour PET imaging: version 1.0. Eur J Nucl Med Mol Imaging 2010;37:181–200.
14. Kawasaki K, Ishii K, Saito Y, *et al*. Influence of mild hyperglycemia on cerebral FDG distribution patterns calculated by statistical parametric mapping. *Ann Nucl Med* 2008;22:191–200.
15. Lindholm P, Minn H, Leskinen-Kallio S, *et al*. Influence of the blood glucose concentration on FDG uptake in cancer--a PET study. *J Nucl Med* 1993;34:1–6.
16. Hadi M, Bacharach SL, Whatley M, *et al*. Glucose and insulin variations in patients during the time course of a FDG-PET study and implications for the "glucose-corrected" SUV. *Nucl Med Biol* 2008;35:441–445.
17. Dunn JT, Anthony K, Amiel SA, *et al*. Correction for the effect of rising plasma glucose levels on quantification of MR(glc) with FDG-PET. *J Cereb Blood Flow Metab* 2009;29:1059–1067.
18. Bøtker HE, Böttcher M, Schmitz O, *et al*. Glucose uptake and lumped constant variability in normal human hearts determined with [18F]fluorodeoxyglucose. *J Nucl Cardiol* 1997;4:125–132.
19. Graham MM, Muzi M, Spence AM, *et al*. The FDG lumped constant in normal human brain. *J Nucl Med* 2002;43:1157–1166.
20. Selberg O, Müller MJ, van den Hoff J, *et al*. Use of positron emission tomography for the assessment of skeletal muscle glucose metabolism. *Nutrition* 2002;18:323–328.
21. Bass L, Sørensen M, Lajord Munk O, *et al*. Analogue tracers and lumped constant in capillary beds. *J Theor Biol* 2011;285:177–181.
22. Gjedde A, Wienhard K, Heiss W-D, *et al*. Comparative regional analysis of 2-fluorodeoxyglucose and methylglucose uptake in brain of four stroke patients. With special reference to the regional estimation of the lumped constant. *J Cereb Blood Flow Metab* 1985;5:163–178.
23. Spence AM, Muzi M, Graham MM, *et al*. Glucose metabolism in human malignant gliomas measured quantitatively with PET, 1-[C-11]glucose and FDG: analysis of the FDG lumped constant. *J Nucl Med* 1998;39:440–448.
24. Kopka L, Vosshenrich R, Rodenwaldt J, *et al*. Differences in injection rates on contrast-enhanced breath-hold three-dimensional MR angiography. *Am J Roentgenol* 1998;170:345–348.
25. Walker MD, Matthews JC, Asselin M-C, *et al*. Development and validation of a variance model for dynamic PET: uses in fitting kinetic data and optimizing the injected activity. *Phys Med Biol* 2010;55:6655–6672.
26. Sadato N, Carson RE, Daube-Witherspoon ME, *et al*. Optimization of noninvasive activation studies with 15O-water and three-dimensional positron emission tomography. *J Cereb Blood Flow Metab* 1997;17:732–739.
27. Raylman RR, Caraher JM, and Hutchins GD. Sampling requirements for dynamic cardiac PET studies using image-derived input functions. *J Nucl Med* 1993;34:440–447.
28. Eriksson O, Wallberg A, Syvänen S, *et al*. A computerized Infusion Pump for control of tissue tracer concentration during Positron Emission Tomography in vivo Pharmacokinetic/Pharmacodynamic measurements. *Med Phys* 2008;8:2.
29. Iida H, Takahashi A, Tamura Y, *et al*. Myocardial blood flow: comparison of oxygen-15-water bolus injection, slow infusion and oxygen-15-carbon dioxide slow inhalation. *J Nucl Med* 1995;36:78–85.
30. Beason-Held LL, Desmond RE, Herscovitch P, *et al*. Bolus injection versus slow infusion of [15O]water for positron emission tomography activation studies. *J Cereb Blood Flow Metab* 1999;19:843–852.
31. Evans AC, Diksic M, Yamamoto YL, *et al*. Effect of vascular activity in the determination of rate constants for the uptake of 18F-labeled 2-fluoro-2-deoxy-D-glucose: error analysis and normal values in older subjects. *J Cereb Blood Flow Metab* 1986;6:724–738.
32. Mazoyer BM, Huesman RH, Budinger TF, *et al*. Dynamic PET data analysis. *J Comput Assist Tomogr* 1986;10:645–653.
33. deKemp R, Klein R, Lortie M, *et al*. Constant-activity-rate infusions for myocardial blood flow quantification with 82Rb and 3D PET. *In: IEEE Nucl Sci Symp Conf Rec. IEEE;* 2006. p. 3519–3521.
34. Freedman NM, Bacharach SL, McCord ME, *et al*. Spatially dependent deadtime losses in high count rate cardiac PET. *J Nucl Med* 1992;33:2226–2231.
35. Bettinardi V, Presotto L, Rapisarda E, *et al*. Physical Performance of the new hybrid PET/CT Discovery-690. *Med Phys* 2011;38:5394–5411.
36. Surti S, Kuhn A, Werner ME, *et al*. Performance of Philips Gemini TF PET/CT scanner with special consideration for its time-of-flight imaging capabilities. *J Nucl Med* 2007;48:471–480.

37. Jakoby BW, Bercier Y, Conti M, *et al*. Physical and clinical performance of the mCT time-of-flight PET/CT scanner. *Phys Med Biol* 2011;56:2375–2389.
38. Strauss LG. Reply: Shortened Dynamic 18F-FDG PET. *J Nucl Med* 2011;52:1330–1331.
39. Ho-Shon K, Feng D, Hawkins RA, *et al*. Optimized sampling and parameter estimation for quantification in whole body PET. *IEEE Trans Biomed Eng* 1996;43:1021–1028.
40. Dai X, Chen Z, and Tian J. Performance evaluation of kinetic parameter estimation methods in dynamic FDG-PET studies. *Nucl Med Commun* 2011;32:4–16.
41. Huang SC, Phelps ME, Hoffman EJ, *et al*. Error sensitivity of fluorodeoxyglucose method for measurement of cerebral metabolic rate of glucose. *J Cereb Blood Flow Metab* 1981;1:391–401.
42. Torizuka T, Nobezawa S, Momiki S, *et al*. Short dynamic FDG-PET imaging protocol for patients with lung cancer. *Eur J Nucl Med* 2000;27:1538–1542.
43. Strauss LG, Dimitrakopoulou-Strauss A, and Haberkorn U. Shortened PET data acquisition protocol for the quantification of 18F-FDG kinetics. *J Nucl Med* 2003;44:1933–1939.
44. Monden T, Kudomi N, Sasakawa Y, *et al*. Shortening the duration of [18F]FDG PET brain examination for diagnosis of brain glioma. *Mol Imaging Biol* 2011;13:754–758.
45. Strauss LG, Pan L, Cheng C, *et al*. Shortened acquisition protocols for the quantitative assessment of the 2-tissue-compartment model using dynamic PET/CT 18F-FDG studies. *J Nucl Med* 2011;52:379–385.
46. Sureshbabu W and Mawlawi O. PET/CT imaging artifacts. *J Nucl Med Technol* 2005;33:156–161.
47. Beyer T, Bockisch A, Kühl H, *et al*. Whole-body 18F-FDG PET/CT in the presence of truncation artifacts. *J Nucl Med* 2006;47:91–99.
48. Kinahan PE, Hasegawa BH, and Beyer T. X-ray-based attenuation correction for positron emission tomography/computed tomography scanners. *Semin Nucl Med* 2003;33:166–179.
49. Beyer T, Antoch G, Müller S, *et al*. Acquisition protocol considerations for combined PET/CT imaging. *J Nucl Med* 2004;45 Suppl 1:25S-35S.
50. Vera P, Ouvrier MJ, Hapdey S, *et al*. Does chemotherapy influence the quantification of SUV when contrast-enhanced CT is used in PET/CT in lymphoma? *Eur J Nucl Med Mol Imaging* 2007;34:1943–1952.
51. Mourik JEM, Lubberink M, Lammertsma A a, *et al*. Image derived input functions: effects of motion on tracer kinetic analyses. *Mol Imaging Biol* 2011;13:25–31.
52. Nehmeh SA, Erdi YE, Ling CC, *et al*. Effect of respiratory gating on quantifying PET images of lung cancer. *J Nucl Med* 2002;43:876–881.
53. Klein GJ, Reutter BW, Ho MH, *et al*. Real-time system for respiratory-cardiac gating in positron tomography. *IEEE Trans Nucl Sci* 1998;45:2139–2143.
54. Wang Y, Baghaei H, Li H, *et al*. A simple respiration gating technique and its application in high-resolution PET camera. *IEEE Trans Nucl Sci* 2005;52:125–129.
55. Nehmeh SA, Erdi YE, Rosenzweig KE, *et al*. Reduction of respiratory motion artifacts in PET imaging of lung cancer by respiratory correlated dynamic PET: methodology and comparison with respiratory gated PET. *J Nucl Med* 2003;44:1644–1648.
56. Menke M, Atkins MS, and Buckley KR. Compensation methods for head motion detected during PET scans. *IEEE Nucl Sci Symp Conf Rec* 1995;4:1638–1642.
57. El Naqa I, Low DA, Bradley JD, *et al*. Deblurring of breathing motion artifacts in thoracic PET images by deconvolution methods. *Med Phys* 2006;33:3587–3600.
58. Li T, Thorndyke B, Schreibmann E, *et al*. Model-based image reconstruction for four-dimensional PET. *Med Phys* 2006;33:1288–1298.
59. Wang J, del Valle M, Goryawala M, *et al*. Computer-assisted quantification of lung tumors in respiratory gated PET/CT images: phantom study. *Med Biol Eng Compu* 2010;48:49–58.
60. Rahmim A, Dinelle K, Cheng J-C, *et al*. Accurate event-driven motion compensation in high-resolution PET incorporating scattered and random events. *IEEE Trans Med Imaging* 2008;27:1018–1033.
61. Picard Y and Thompson CJ. Motion correction of PET images using multiple acquisition frames. *IEEE Trans Med Imaging* 1997;16:137–144.
62. Costes N, Dagher A, Larcher K, *et al*. Motion correction of multi-frame PET data in neuroreceptor mapping: simulation based validation. *Neuroimage* 2009;47:1496–1505.
63. van den Heuvel OA, Boellaard R, Veltman DJ, *et al*. Attenuation correction of PET activation studies in the presence of task-related motion. *Neuroimage* 2003;19:1501–1509.
64. Lu W and Mackie TR. Tomographic motion detection and correction directly in sinogram space. *Phys Med Biol* 2002;47:1267–1284.
65. Jin X, Mulnix T, Planeta-Wilson B, *et al*. Accuracy of Head Motion Compensation for the HRRT: Comparison of Methods. *IEEE Nucl Sci Symp Conf Rec* 2009;2009:3199–3202.
66. Rahmim A, Rousset O, and Zaidi H. Strategies for Motion Tracking and Correction in PET. *PET Clinics* 2007;2:251–266.
67. Nehmeh SA and Erdi YE. Respiratory motion in positron emission tomography/computed tomography: a review. *Semin Nucl Med* 2008;38:167–176.
68. Jovkar S, Evans AC, Diksic M, *et al*. Minimisation of parameter estimation errors in dynamic PET: choice of scanning schedules. *Phys Med Biol* 1989;34:895–908.
69. Li X, Feng D, and Chen K. Optimal image sampling schedule for both image-derived input and output functions in PET cardiac studies. *IEEE Trans Med Imaging* 2000;19:233–242.
70. Hunter GJ, Hamberg LM, Alpert NM, *et al*. Simplified measurement of deoxyglucose utilization rate. *J Nucl Med* 1996;37:950–955.
71. Torizuka T, Zasadny KR, and Wahl RL. Diabetes Decreases FDG Accumulation in Primary Lung Cancer. *Clin Positron Imaging* 1999;2:281–287.
72. Krak NC, van der Hoeven JJM, Hoekstra OS, *et al*. Measuring [(18)F]FDG uptake in breast cancer during chemotherapy: comparison of analytical methods. *Eur J Nucl Med Mol Imaging* 2003;30:674–681.
73. Strauss LG, Dimitrakopoulou-Strauss A, Koczan D, *et al*. 18F-FDG kinetics and gene expression in giant cell tumors. *J Nucl Med* 2004;45:1528–1535.

74. Spence AM, Muzi M, Mankoff DA, *et al*. 18F-FDG PET of gliomas at delayed intervals: improved distinction between tumor and normal gray matter. *J Nucl Med* 2004;45:1653–1659.
75. Nishiyama Y, Yamamoto Y, Monden T, *et al*. Diagnostic value of kinetic analysis using dynamic FDG PET in immunocompetent patients with primary CNS lymphoma. *Eur J Nucl Med Mol Imaging* 2007;34:78–86.
76. Partridge SC, Vanantwerp RK, Doot RK, *et al*. Association between serial dynamic contrast-enhanced MRI and dynamic 18F-FDG PET measures in patients undergoing neoadjuvant chemotherapy for locally advanced breast cancer. *J Magn Reson Imaging* 2010;32:1124–1131.
77. Parker BJ. Graph-based Mumford-Shah segmentation of dynamic PET with application to input function estimation. *IEEE Trans Nucl Sci* 2005;52:79–89.
78. Su K-H, Wu L-C, Liu R-S, *et al*. Quantification method in [18F]fluorodeoxyglucose brain positron emission tomography using independent component analysis. *Nucl Med Commun* 2005;26:995–1004.
79. Strauss LG, Klippel S, Pan L, *et al*. Assessment of quantitative FDG PET data in primary colorectal tumours: which parameters are important with respect to tumour detection? Eur J Nucl Med Mol Imaging 2007;34:868–877.
80. Zanotti-Fregonara P, Fadaili EM, Maroy R, *et al*. Comparison of eight methods for the estimation of the image-derived input function in dynamic [(18)F]-FDG PET human brain studies. *J Cereb Blood Flow Metab* 2009;29:1825–1835.
81. Zanotti-Fregonara P, Maroy R, Comtat C, *et al*. Comparison of 3 methods of automated internal carotid segmentation in human brain PET studies: application to the estimation of arterial input function. *J Nucl Med* 2009;50:461–467.
82. O`Sullivan F, Muzi M, Spence AM, *et al*. Nonparametric Residue Analysis of Dynamic PET Data With Application to Cerebral FDG Studies in Normals. *J Am Stat Assoc* 2009;104:556–571.
83. Ogden RT, Zanderigo F, Choy S, *et al*. Simultaneous estimation of input functions: an empirical study. *J Cereb Blood Flow Metab* 2010;30:816–826.
84. Croteau E, Lavallée E, Labbe SM, *et al*. Image-derived input function in dynamic human PET/CT: methodology and validation with (11)C-acetate and (18)F-fluorothioheptadecanoic acid in muscle and (18)F-fluorodeoxyglucose in brain. *Eur J Nucl Med Mol Imaging* 2010;37:1539–1550.
85. Hapdey S, Buvat I, Carson JM, *et al*. Searching for Alternatives to Full Kinetic Analysis in 18F-FDG PET: An Extension of the Simplified Kinetic Analysis Method. *J Nucl Med* 2011;52:634–641.
86. Rahmim A, Tang J, and Zaidi H. Four-dimensional (4D) image reconstruction strategies in dynamic PET: Beyond conventional independent frame reconstruction. *Med Phys* 2009;36:3654–3670.
87. Wang G and Qi J. Generalized algorithms for direct reconstruction of parametric images from dynamic PET data. *IEEE Trans Med Imaging* 2009;28:1717–1726.
88. Hove JD, Rasmussen R, Freiberg J, *et al*. Clinical evaluation of iterative reconstruction (ordered-subset expectation maximization) in dynamic positron emission tomography: quantitative effects on kinetic modeling with N-13 ammonia in healthy subjects. *J Nucl Cardiol* 2008;15:530–534.
89. Søndergaard HM, Madsen MM, Boisen K, *et al*. Evaluation of iterative reconstruction (OSEM) versus filtered back-projection for the assessment of myocardial glucose uptake and myocardial perfusion using dynamic PET. *Eur J Nucl Med Mol Imaging* 2007;34:320–329.
90. Morimoto T, Ito H, Takano A, *et al*. Effects of image reconstruction algorithm on neurotransmission PET studies in humans: comparison between filtered backprojection and ordered subsets expectation maximization. *Ann Nucl Med* 2006;20:237–243.
91. Boellaard R, van Lingen A, and Lammertsma AA. Experimental and clinical evaluation of iterative reconstruction (OSEM) in dynamic PET: quantitative characteristics and effects on kinetic modeling. *J Nucl Med* 2001;42:808–817.
92. Reilhac A, Tomeï S, Buvat I, *et al*. Simulation-based evaluation of OSEM iterative reconstruction methods in dynamic brain PET studies. *Neuroimage* 2008;39:359–368.
93. Bélanger MJ, Mann JJ, and Parsey RV. OS-EM and FBP reconstructions at low count rates: effect on 3D PET studies of [11C] WAY-100635. *Neuroimage* 2004;21:244–250.
94. Oda K, Toyama H, Uemura K, *et al*. Comparison of parametric FBP and OS-EM reconstruction algorithm images for PET dynamic study. *Ann Nucl Med* 2001;15:417–423.
95. van Velden FHP, Kloet RW, van Berckel BNM, *et al*. Accuracy of 3-dimensional reconstruction algorithms for the high-resolution research tomograph. *J Nucl Med* 2009;50:72–80.
96. Byrne C. Iterative algorithms for deblurring and deconvolution with constraints. *Inverse Probl* 1998;14:1455–1467.
97. Verhaeghe J and Reader AJ. AB-OSEM reconstruction for improved Patlak kinetic parameter estimation: a simulation study. *Phys Med Biol* 2010;55:6739–6757.
98. Walker MD, Asselin M-C, Julyan PJ, *et al*. Bias in iterative reconstruction of low-statistics PET data: benefits of a resolution model. *Phys Med Biol* 2011;56:931–949.
99. Christian BT, Vandehey NT, Floberg JM, *et al*. Dynamic PET denoising with HYPR processing. *J Nucl Med* 2010;51:1147–1154.
100. Cherry SR and Dahlbom M. PET: Physics, Instrumentation, and Scanners. *In: PET, Molecular Imaging and Its Biological Applications.* Phelps ME, editor. New York, NY: Springer; 2004. p. 1–124.
101. Cherry SR and Huang S-C. Effects of scatter on model parameter estimates in 3D PET studies of the human brain. *IEEE Trans Nucl Sci* 1995;42:1174–1179.
102. Macq B, Sibomana M, Coppens A, *et al*. Lossless compression for 3D PET. *IEEE Trans Nucl Sci* 1994;41:2765–2770.
103. Asma E, Shattuck DW, and Leahy RM. Lossless compression of dynamic PET data. *IEEE Trans Nucl Sci* 2003;50:9–16.
104. Vandenberghe S, Staelens S, van de Walle R, *et al*. Compression and reconstruction of sorted PET listmode data. *Nucl Med Commun* 2005;26:819–825.
105. Cunningham VJ, Hume SP, Price GR, *et al*. Compartmental analysis of diprenorphine binding to opiate receptors in the rat in vivo and its comparison with equilibrium data in vitro. *J Cereb Blood Flow Metab* 1991;11:1–9.
106. Gunn RN, Lammertsma AA, Hume SP, *et al*. Parametric imaging of ligand-receptor binding in PET using a simplified reference region model. *Neuroimage* 1997;6:279–287.
107. Litton JE, Hall H, and Pauli S. Saturation analysis in PET--analysis of errors due to imperfect reference regions. *J Cereb Blood Flow Metab* 1994;14:358–361.
108. Everett BA, Oquendo MA, Abi-Dargham A, *et al*. Safety of radial arterial catheterization in PET research subjects. *J Nucl Med* 2009;50:1742.

109. Zanotti-Fregonara P, Chen K, Liow J-S, *et al*. Image-derived input function for brain PET studies: many challenges and few opportunities. *J Cereb Blood Flow Metab* 2011;
110. Phelps ME, Huang SC, Hoffman EJ, *et al*. Tomographic measurement of local cerebral glucose metabolic rate in humans with (F-18)2-fluoro-2-deoxy-D-glucose: validation of method. *Ann Neurol* 1979;6:371–388.
111. Weinberg IN, Huang SC, Hoffman EJ, *et al*. Validation of PET-acquired input functions for cardiac studies. *J Nucl Med* 1988;29:241–247.
112. de Geus-Oei L-F, Visser EP, Krabbe PFM, *et al*. Comparison of image-derived and arterial input functions for estimating the rate of glucose metabolism in therapy-monitoring 18F-FDG PET studies. *J Nucl Med* 2006;47:945–949.
113. Lüdemann L, Sreenivasa G, Michel R, *et al*. Corrections of arterial input function for dynamic H215O PET to assess perfusion of pelvic tumours: arterial blood sampling versus image extraction. *Phys Med Biol* 2006;51:2883–2900.
114. Litton JE. Input function in PET brain studies using MR-defined arteries. *J Comput Assist Tomogr* 1997;21:907–909.
115. Chen K, Bandy D, Reiman E, *et al*. Noninvasive quantification of the cerebral metabolic rate for glucose using positron emission tomography, 18F-fluoro-2-deoxyglucose, the Patlak method, and an image-derived input function. *J Cereb Blood Flow Metab* 1998;18:716–723.
116. Wu HM, Hoh CK, Choi Y, *et al*. Factor analysis for extraction of blood time-activity curves in dynamic FDG-PET studies. *J Nucl Med* 1995;36:1714–1722.
117. Liptrot M, Adams KH, Martiny L, *et al*. Cluster analysis in kinetic modelling of the brain: a noninvasive alternative to arterial sampling. *Neuroimage* 2004;21:483–493.
118. Feng D, Wong KP, Wu CM, *et al*. A technique for extracting physiological parameters and the required input function simultaneously from PET image measurements: theory and simulation study. *IEEE Trans Inf Technol Biomed* 1997;1:243–254.
119. Wong KP, Feng D, Meikle SR, *et al*. Simultaneous estimation of physiological parameters and the input function–in vivo PET data. *IEEE Trans Inf Technol Biomed* 2001;5:67–76.
120. Vriens D, de Geus-Oei L-F, Oyen WJG, *et al*. A curve-fitting approach to estimate the arterial plasma input function for the assessment of glucose metabolic rate and response to treatment. *J Nucl Med* 2009;50:1933–1939.
121. Patlak CS, Blasberg RG, and Fenstermacher JD. Graphical evaluation of blood-to-brain transfer constants from multiple-time uptake data. *J Cereb Blood Flow Metab* 1983;3:1–7.
122. Moriyasu F, Nishida O, Ban N, *et al*. "Congestion index" of the portal vein. *Am J Roentgenol* 1986;146:735–739.
123. Munk OL, Bass L, Roelsgaard K, *et al*. Liver kinetics of glucose analogs measured in pigs by PET: importance of dual-input blood sampling. *J Nucl Med* 2001;42:795–801.
124. Brix G, Ziegler SI, Bellemann ME, *et al*. Quantification of [(18)F]FDG uptake in the normal liver using dynamic PET: impact and modeling of the dual hepatic blood supply. *J Nucl Med* 2001;42:1265–1273.
125. Winterdahl M, Keiding S, Sørensen M, *et al*. Tracer input for kinetic modelling of liver physiology determined without sampling portal venous blood in pigs. *Eur J Nucl Med Mol Imaging* 2011;38:263–270.
126. Munk OL, Keiding S, and Bass L. A method to estimate dispersion in sampling catheters and to calculate dispersion-free blood time-activity curves. *Med Phys* 2008;35:3471–3481.
127. Iida H, Higano S, Tomura N, *et al*. Evaluation of regional differences of tracer appearance time in cerebral tissues using [15O] water and dynamic positron emission tomography. *J Cereb Blood Flow Metab* 1988;8:285–288.
128. Hinz R and Turkheimer FE. Determination of tracer arrival delay with spectral analysis. *IEEE Trans Nucl Sci* 2006;53:212–219.
129. Meyer E. Simultaneous correction for tracer arrival delay and dispersion in CBF measurements by the H215O autoradiographic method and dynamic PET. *J Nucl Med* 1989;30:1069–1078.
130. van den Hoff J, Burchert W, Müller-Schauenburg W, *et al*. Accurate local blood flow measurements with dynamic PET: fast determination of input function delay and dispersion by multilinear minimization. *J Nucl Med* 1993;34:1770–1777.
131. Fox JL, Rengan R, O'Meara W, *et al*. Does registration of PET and planning CT images decrease interobserver and intraobserver variation in delineating tumor volumes for non-small-cell lung cancer? *Int J Radiat Oncol Biol Phys* 2005;62:70–75.
132. van Baardwijk A, Bosmans G, Boersma L, *et al*. PET-CT-based auto-contouring in non-small-cell lung cancer correlates with pathology and reduces interobserver variability in the delineation of the primary tumor and involved nodal volumes. *Int J Radiat Oncol Biol Phys* 2007;68:771–778.
133. Janssen MHM, Aerts HJWL, Ollers MC, *et al*. Tumor delineation based on time-activity curve differences assessed with dynamic fluorodeoxyglucose positron emission tomography-computed tomography in rectal cancer patients. *Int J Radiat Oncol Biol Phys* 2009;73:456–465.
134. Soret M, Bacharach SL, and Buvat I. Partial-volume effect in PET tumor imaging. *J Nucl Med* 2007;48:932–945.
135. van Dalen JA, Hoffmann AL, Dicken V, *et al*. A novel iterative method for lesion delineation and volumetric quantification with FDG PET. *Nucl Med Commun* 2007;28:485–493.
136. Bezdek JC. Pattern recognition with fuzzy objective function algorithms. *New York: Plenum Press;* 1981.
137. Hatt M, Cheze le Rest C, Turzo A, *et al*. A fuzzy locally adaptive Bayesian segmentation approach for volume determination in PET. *IEEE Trans Med Imaging* 2009;28:881–893.
138. Hatt M, Cheze le Rest C, Descourt P, *et al*. Accurate automatic delineation of heterogeneous functional volumes in positron emission tomography for oncology applications. *Int J Radiat Oncol Biol Phys* 2010;77:301–308.
139. Evans AC, Beil C, Marrett S, *et al*. Anatomical-functional correlation using an adjustable MRI-based region of interest atlas with positron emission tomography. *J Cereb Blood Flow Metab* 1988;8:513–530.
140. Bentourkia M and Zaidi H. Tracer Kinetic Modeling in Nuclear Medicine: Theory and Applications. *In: Quantitative Analysis in Nuclear Medicine Imaging.* Zaidi H, editor. New York, NY: Springer; 2006. p. 391–413.
141. Carson RE. Tracer Kinetic Modeling in PET. *In: Positron Emission Tomography.* Bailey DL, Townsend DW, *et al.*, editors. London, UK: Springer; 2005. p. 127–159.
142. Akaike H. A new look at the statistical model identification. *IEEE Trans Automat Contr* 1974;19:716–723.
143. Schwarz G. Estimating the Dimension of a Model. *Ann Stat* 1978;6:461–464.
144. Herscovitch P and Raichle ME. Effect of tissue heterogeneity on the measurement of cerebral blood flow with the equilibrium C15O2 inhalation technique. *J Cereb Blood Flow Metab* 1983;3:407–415.

145. Herholz K and Patlak CS. The influence of tissue heterogeneity on results of fitting nonlinear model equations to regional tracer uptake curves: with an application to compartmental models used in positron emission tomography. *J Cereb Blood Flow Metab* 1987;7:214–229.
146. Blomqvist G, Lammertsma AA, Mazoyer B, *et al*. Effect of tissue heterogeneity on quantification in positron emission tomography. *Eur J Nucl Med* 1995;22:652–663.
147. Schmidt K, Mies G, and Sokoloff L. Model of kinetic behavior of deoxyglucose in heterogeneous tissues in brain: a reinterpretation of the significance of parameters fitted to homogeneous tissue models. *J Cereb Blood Flow Metab* 1991;11:10–24.
148. Schmidt K, Lucignani G, Moresco RM, *et al*. Errors introduced by tissue heterogeneity in estimation of local cerebral glucose utilization with current kinetic models of the [18F]fluorodeoxyglucose method. *J Cereb Blood Flow Metab* 1992;12:823–834.
149. Logan J. Graphical analysis of PET data applied to reversible and irreversible tracers. *Nucl Med Biol* 2000;27:661–670.
150. Hoekstra CJ, Hoekstra OS, Stroobants SG, *et al*. Methods to monitor response to chemotherapy in non-small cell lung cancer with 18F-FDG PET. *J Nucl Med* 2002;43:1304–1309.
151. Slifstein M and Laruelle M. Effects of statistical noise on graphic analysis of PET neuroreceptor studies. *J Nucl Med* 2000;41:2083–2088.
152. Sokoloff L, Reivich M, Kennedy C, *et al*. The [14C]deoxyglucose method for the measurement of local cerebral glucose utilization: theory, procedure, and normal values in the conscious and anesthetized albino rat. *J Neurochem* 1977;28:897–916.
153. Thiele F and Buchert R. Evaluation of non-uniform weighting in non-linear regression for pharmacokinetic neuroreceptor modelling. *Nucl Med Commun* 2008;29:179–188.
154. Yaqub M, Boellaard R, Kropholler MA, *et al*. Optimization algorithms and weighting factors for analysis of dynamic PET studies. *Phys Med Biol* 2006;51:4217–4232.
155. Groves AM, Win T, Haim SB, *et al*. Non-[18F]FDG PET in clinical oncology. *Lancet Oncol* 2007;8:822–830.
156. Tanaka K and Fukase K. PET (positron emission tomography) imaging of biomolecules using metal-DOTA complexes: a new collaborative challenge by chemists, biologists, and physicians for future diagnostics and exploration of in vivo dynamics. *Org Biomol Chem* 2008;6:815–828.
157. Laforest R and Liu X. Cascade removal and microPET imaging with 76Br. *Phys Med Biol* 2009;54:1503–1531.
158. Bigott HM, Laforest R, Liu X, *et al*. Advances in the production, processing and microPET image quality of technetium-94m. *Nucl Med Biol* 2006;33:923–933.
159. Bai B, Ruangma A, Laforest R, *et al*. Positron Range Modeling for Statistical PET Image Reconstruction. *In: IEEE Nucl Sci Symp Conf Rec. IEEE;* 2003. p. 2501–2505.
160. NEMA Standards Publication NU 2-1994: Performance Measurements of Positron Emission Tomographs. Rosslyn, VA: National Electrical Manufacturers Association (NEMA); 1994.
161. NEMA Standards Publication NU 2-2001: Performance Measurements of Positron Emission Tomographs. Rosslyn, VA: National Electrical Manufacturers Association (NEMA); 2001.
162. Bao Q, Newport D, Chen M, *et al*. Performance evaluation of the inveon dedicated PET preclinical tomograph based on the NEMA NU-4 standards. *J Nucl Med* 2009;50:401–408.
163. Visser EP, Disselhorst JA, Brom M, *et al*. Spatial resolution and sensitivity of the Inveon small-animal PET scanner. *J Nucl Med* 2009;50:139–147.
164. Kemp BJ, Hruska CB, McFarland AR, *et al*. NEMA NU 2-2007 performance measurements of the Siemens Inveon preclinical small animal PET system. *Phys Med Biol* 2009;54:2359–2376.
165. Constantinescu CC and Mukherjee J. Performance evaluation of an Inveon PET preclinical scanner. *Phys Med Biol* 2009;54:2885–2899.
166. Qi J, Leahy RM, Cherry SR, *et al*. High-resolution 3D Bayesian image reconstruction using the microPET small-animal scanner. *Phys Med Biol* 1998;43:1001–1013.
167. Radionuclide Decay Data [Internet]. Health Physics Society (HPS). *Accessed: 2010 Feb 16; Available from: http://hps.org/publicinformation/radardecaydata.cfm*
168. ICRU report 37: Stopping Powers for Electrons and Positrons. Bethesda, MD: International Commission on Radiation Units & Measurements (ICRU); 1984.
169. Watson CC. New, faster, image-based scatter correction for 3D PET. *IEEE Nucl Sci Symp Conf Rec* 1999;3:1637–1641.
170. Palmer MR, Zhu X, and Parker JA. Modeling and Simulation of Positron Range Effects for High Resolution PET Imaging. *IEEE Trans Nucl Sci* 2005;52:1391–1395.
171. Snyder DL, Miller MI, Thomas LJ, *et al*. Noise and edge artifacts in maximum-likelihood reconstructions for emission tomography. *IEEE Trans Med Imaging* 1987;6:228–238.
172. Liu X and Laforest R. Quantitative small animal PET imaging with nonconventional nuclides. *Nucl Med Biol* 2009;36:551–559.
173. Pentlow KS, Graham MC, Lambrecht RM, *et al*. Quantitative imaging of iodine-124 with PET. *J Nucl Med* 1996;37:1557–1562.
174. Herzog H, Tellman L, Qaim SM, *et al*. PET quantitation and imaging of the non-pure positron-emitting iodine isotope 124I. *Appl Radiat Isot* 2002;56:673–679.
175. Gregory RA, Hooker CA, Partridge M, *et al*. Optimization and assessment of quantitative 124I imaging on a Philips Gemini dual GS PET/CT system. *Eur J Nucl Med Mol Imaging* 2009;36:1037–1048.
176. Beattie BJ, Finn RD, Rowland DJ, *et al*. Quantitative imaging of bromine-76 and yttrium-86 with PET: A method for the removal of spurious activity introduced by cascade gamma rays. *Med Phys* 2003;30:2410.
177. Ribeiro MJ, Almeida P, Strul D, *et al*. Comparison of fluorine-18 and bromine-76 imaging in positron emission tomography. *Eur J Nucl Med* 1999;26:758–766.
178. Lubberink M, Schneider H, Bergström M, *et al*. Quantitative imaging and correction for cascade gamma radiation of 76Br with 2D and 3D PET. *Phys Med Biol* 2002;47:3519–3534.
179. Walrand S, Jamar F, Mathieu I, *et al*. Quantitation in PET using isotopes emitting prompt single gammas: application to yttrium-86. *Eur J Nucl Med Mol Imaging* 2003;30:354–361.

180. Buchholz HG, Herzog H, Förster GJ, *et al*. PET imaging with yttrium-86: comparison of phantom measurements acquired with different PET scanners before and after applying background subtraction. *Eur J Nucl Med Mol Imaging* 2003;30:716–720.
181. Kull T, Ruckgaber J, Weller R, *et al*. Quantitative imaging of yttrium-86 PET with the ECAT EXACT HR+ in 2D mode. *Cancer Biother Radiopharm* 2004;19:482–490.
182. Newport DF, Siegel SB, Swann BK, *et al*. QuickSilver: A Flexible, Extensible, and High-Speed Architecture for Multi-Modality Imaging. *In: IEEE Nucl Sci Symp Conf Rec. IEEE;* 2006. p. 2333–2334.
183. Atkins BE, Pressley DR, Lenox MW, *et al*. A Data Acquisition, Event Processing and Coincidence Determination Module for a Distributed Parallel Processing Architecture for PET and SPECT Imaging. *In: IEEE Nucl Sci Symp Conf Rec. IEEE;* 2006. p. 2439–2442.
184. McFarland AR, Newport DF, Atkins BE, *et al*. A Compact PCI Based Event Routing Subsystem for PET and SPECT Data Acquisition. *In: IEEE Nucl Sci Symp Conf Rec. IEEE;* 2006. p. 3091–3093.
185. McFarland AR, Siegel S, Newport DF, *et al*. Continuously sampled digital pulse processing for inveon small animal PET scanner. *In: IEEE Nucl Sci Symp Conf Rec. IEEE;* 2007. p. 4262–4265.
186. Mintzer RA and Siegel SB. Design and performance of a new pixelated- LSO/PSPMT gamma-ray detector for high resolution PET imaging. *In: IEEE Nucl Sci Symp Conf Rec. IEEE;* 2007. p. 3418–3422.
187. Defrise M, Kinahan PE, Townsend DW, *et al*. Exact and approximate rebinning algorithms for 3-D PET data. *IEEE Trans Med Imaging* 1997;16:145–158.
188. Cherry SR, Sorenson JA, and Phelps ME. Physics in Nuclear Medicine. 3rd ed. Philadelphia PA: Saunders; 2003.
189. Matej S, Karp JS, Lewitt RM, *et al*. Performance of the Fourier rebinning algorithm for PET with large acceptance angles. *Phys Med Biol* 1998;43:787–795.
190. Fahey FH. Data acquisition in PET imaging. *J Nucl Med Technol* 2002;30:39–49.
191. Stabin MG and da Luz LCQP. Decay data for internal and external dose assessment. *Health Phys* 2002;83:471–475.
192. Kim JS, Lee JS, Im KC, *et al*. Performance measurement of the microPET focus 120 scanner. *J Nucl Med* 2007;48:1527–1535.
193. Huisman MC, Reder S, Weber AW, *et al*. Performance evaluation of the Philips MOSAIC small animal PET scanner. *Eur J Nucl Med Mol Imaging* 2007;34:532–540.
194. Wang Y, Seidel J, Tsui BMW, *et al*. Performance evaluation of the GE healthcare eXplore VISTA dual-ring small-animal PET scanner. *J Nucl Med* 2006;47:1891–1900.
195. Sempere-Roldan P, Canadas M, Dietzel O, *et al*. Performance evaluation of raytest ClearPET, a PET scanner for small and medium size animals. *In: IEEE Nucl Sci Symp Conf Rec. IEEE;* 2007. p. 2859–2864.
196. Sempere-Roldan P, Chereul E, Dietzel O, *et al*. Raytest ClearPETTM, a new generation small animal PET scanner. *Nucl Instrum Meth A* 2007;571:498–501.
197. Cho S, Li Q, Ahn S, *et al*. Iterative image reconstruction using inverse Fourier rebinning for fully 3-D PET. *IEEE Trans Med Imaging* 2007;26:745–756.
198. Tai Y-C, Ruangma A, Rowland D, *et al*. Performance evaluation of the microPET focus: a third-generation microPET scanner dedicated to animal imaging. *J Nucl Med* 2005;46:455–463.
199. Bahri MA, Plenevaux A, Warnock G, *et al*. NEMA NU4-2008 image quality performance report for the microPET focus 120 and for various transmission and reconstruction methods. *J Nucl Med* 2009;50:1730–1738.
200. Lage E, Vaquero JJ, Sisniega A, *et al*. Design and performance evaluation of a coplanar multimodality scanner for rodent imaging. *Phys Med Biol* 2009;54:5427–5441.
201. Westerterp M, Pruim J, Oyen WJG, *et al*. Quantification of FDG PET studies using standardised uptake values in multi-centre trials: effects of image reconstruction, resolution and ROI definition parameters. *Eur J Nucl Med Mol Imaging* 2007;34:392–404.
202. Boellaard R, Oyen WJG, Hoekstra CJ, *et al*. The Netherlands protocol for standardisation and quantification of FDG whole body PET studies in multi-centre trials. *Eur J Nucl Med Mol Imaging* 2008;35:2320–2333.
203. Visser EP, Disselhorst JA, Laverman P, *et al*. Contribution of normalization to image noise for the Siemens Inveon small-animal PET scanner. *Nucl Instrum Meth A* 2009;605:433–435.
204. Watson CC. New, faster, image-based scatter correction for 3D PET. *IEEE Trans Nucl Sci* 2000;47:1587–1594.
205. Gleason SS, Austin DW, Beach RS, *et al*. A new highly versatile multimodality small animal imaging platform. *In: IEEE Nucl Sci Symp Conf Rec. IEEE;* 2006. p. 2447–2449.
206. McBride WJ, Sharkey RM, Karacay H, *et al*. A novel method of 18F radiolabeling for PET. *J Nucl Med* 2009;50:991–998.
207. Kemp BJ, Kim C, Williams JJ, *et al*. NEMA NU 2-2001 performance measurements of an LYSO-based PET/CT system in 2D and 3D acquisition modes. *J Nucl Med* 2006;47:1960–1967.
208. Boellaard R. Standards for PET image acquisition and quantitative data analysis. *J Nucl Med* 2009;50 Suppl 1:11S-20S.
209. Erdi YE, Nehmeh SA, Mulnix T, *et al*. PET performance measurements for an LSO-based combined PET/CT scanner using the National Electrical Manufacturers Association NU 2-2001 standard. *J Nucl Med* 2004;45:813–821.
210. Hawkins RA, Phelps ME, and Huang SC. Effects of temporal sampling, glucose metabolic rates, and disruptions of the blood-brain barrier on the FDG model with and without a vascular compartment: studies in human brain tumors with PET. *J Cereb Blood Flow Metab* 1986;6:170–183.
211. Vriens D, de Geus-Oei L-F, Oyen WJG, *et al*. Pharmacokinetic analysis of tumor heterogeneity using FDG-PET. *Society of Nuclear Medicine Annual Meeting Abstracts* 2010;51:113.
212. Li X, Feng D, and Wong K. A general algorithm for optimal sampling schedule design in nuclear medicine imaging. *Comput Methods Programs Biomed* 2001;65:45–59.
213. D`Argenio DZ. Optimal sampling times for pharmacokinetic experiments. *J Pharmacokinet Biopharm* 1981;9:739–756.
214. Lloyd SP. Least squares quantization in PCM. *IEEE Trans Inform Theory* 1982;28:129–137.
215. Max J. Quantizing for minimum distortion. *IEEE Trans Inform Theory* 1960;6:7–12.
216. Wilson DW, Tsui BM, and Barrett HH. Noise properties of the EM algorithm: II. Monte Carlo simulations. *Phys Med Biol* 1994;39:847–871.
217. Moré JJ. The Levenberg-Marquardt algorithm: Implementation and theory. *In: Lect Notes Math.* Watson GA, editor. Berlin: Springer; 1978. p. 105–116.
218. Rajendran JG and Krohn K. PET Imaging for Tumor Hypoxia: Characterizing the Tumor and Guiding Treatment. *In: Positron Emission Tomography.* Valk PE, Delbeke D, et al., editors. London: Springer; 2006. p. 359–374.

219. Barwick T, Bencherif B, Mountz JM, *et al*. Molecular PET and PET/CT imaging of tumour cell proliferation using F-18 fluoro-L-thymidine: a comprehensive evaluation. *Nucl Med Commun* 2009;30:908–917.
220. Hillner BE, Siegel BA, Liu D, *et al*. Impact of positron emission tomography/computed tomography and positron emission tomography (PET) alone on expected management of patients with cancer: initial results from the National Oncologic PET Registry. *J Clin Oncol* 2008;26:2155–2161.
221. de Geus-Oei L-F, Vriens D, van Laarhoven HWM, *et al*. Monitoring and predicting response to therapy with 18F-FDG PET in colorectal cancer: a systematic review. *J Nucl Med* 2009;50 Suppl 1:43S-54S.
222. Ford EC, Herman J, Yorke E, *et al*. 18F-FDG PET/CT for image-guided and intensity-modulated radiotherapy. *J Nucl Med* 2009;50:1655–1665.
223. Hong YT and Fryer TD. Kinetic modelling using basis functions derived from two-tissue compartmental models with a plasma input function: general principle and application to [18F]fluorodeoxyglucose positron emission tomography. *Neuroimage* 2010;51:164–172.
224. Visser EP, Philippens MEP, Kienhorst L, *et al*. Comparison of tumor volumes derived from glucose metabolic rate maps and SUV maps in dynamic 18F-FDG PET. *J Nucl Med* 2008;49:892–898.
225. Wienhard K. Measurement of glucose consumption using [(18)F]fluorodeoxyglucose. *Methods* 2002;27:218–225.
226. Okazumi S, Isono K, Enomoto K, *et al*. Evaluation of liver tumors using fluorine-18-fluorodeoxyglucose PET: characterization of tumor and assessment of effect of treatment. *J Nucl Med* 1992;33:333–339.
227. Liu P, Huang G, Dong S, *et al*. Kinetic analysis of experimental rabbit tumour and inflammation model with 18F-FDG PET/CT. *Nuklearmedizin* 2009;48:153–158.
228. Miles KA and Williams RE. Warburg revisited: imaging tumour blood flow and metabolism. *Cancer Imaging* 2008;8:81–86.
229. Mullani NA, Herbst RS, O`Neil RG, *et al*. Tumor blood flow measured by PET dynamic imaging of first-pass 18F-FDG uptake: a comparison with 15O-labeled water-measured blood flow. *J Nucl Med* 2008;49:517–523.
230. Hoekstra CJ, Stroobants SG, Hoekstra OS, *et al*. Measurement of perfusion in stage IIIA-N2 non-small cell lung cancer using H(2)(15)O and positron emission tomography. *Clin Cancer Res* 2002;8:2109–2115.
231. Warburg O. On the origin of cancer cells. *Science* 1956;123:309–314.
232. Höckel M and Vaupel P. Tumor hypoxia: definitions and current clinical, biologic, and molecular aspects. *J Natl Cancer Inst* 2001;93:266–276.
233. Aerts HJWL, Lambin P, and Ruysscher DD. FDG for dose painting: a rational choice. *Radiother Oncol* 2010;97:163–164.
234. Rajendran JG, Mankoff DA, O'Sullivan F, *et al*. Hypoxia and glucose metabolism in malignant tumors: evaluation by [18F]fluoromisonidazole and [18F]fluorodeoxyglucose positron emission tomography imaging. *Clin Cancer Res* 2004;10:2245–2252.
235. Hamberg LM, Hunter GJ, Alpert NM, *et al*. The dose uptake ratio as an index of glucose metabolism: useful parameter or oversimplification? J Nucl Med 1994;35:1308–1312.
236. Jaccard P. Étude comparative de la distribution florale dans une portion des Alpes et du Jura. *Bull Soc Vaud Sci Nat* 1901;37:547–579.
237. Otsu N. A Threshold Selection Method from Gray-Level Histograms. *IEEE Trans Syst Man Cyb* 1979;9:62–66.
238. Wilcoxon F. Individual Comparisons by Ranking Methods. *Biometrics Bull* 1945;1:80–83.
239. Ruangma A, Bai B, Lewis JS, *et al*. Three-dimensional maximum a posteriori (MAP) imaging with radiopharmaceuticals labeled with three Cu radionuclides. *Nucl Med Biol* 2006;33:217–226.
240. Haberkorn U, Hoffend J, Schmidt K, *et al*. Changes in glucose metabolism and gene expression after transfer of anti-angiogenic genes in rat hepatoma. *Eur J Nucl Med Mol Imaging* 2007;34:2011–2023.

10. Dankwoord

Allereerst wil ik mijn promotoren (prof. Slump en prof. Oyen) en co-promotoren (dr. Visser en dr. De Geus-Oei) bedanken voor het mogelijk maken van mijn promotie.

Ik had het voorrecht om het grootste deel van mijn promotie in het aquarium door te brengen. De goede werksfeer en collega's in het dolfinarium en aquarium (en de "P") hebben zeker bijgedragen aan de totstandkoming van dit proefschrift. Speciale dank hierbij voor prof. Boerman. Otto, bedankt dat ik in het aquarium mocht blijven, en voor het grondig lezen, en van commentaar voorzien van o.a. dit proefschrift. Verder wil ik specifiek één aquariumbewoner bedanken voor alle hulp, raad, javastraat, de vele keren dat ik mocht komen eten, enz. Rafke bedankt!

Ook wil ik alle PET laboranten (met name Peter K.) en artsen (met name Marcel en Lioe-Fee) bedanken voor alle dynamische scans. Antoi voor zijn bijdrage aan vooral het eerste deel van dit proefschrift: met de Inveon en ons gerommel met fantoompjes. Dan Dennis, een van de weinigen op de afdeling die zich bezig houdt met dynamische PET, en de enige arts die kan programmeren. Bedankt voor de goede samenwerking bij een aantal projecten, en goede discussies. Jammer dat er het laatste jaar wat weinig tijd was, maar misschien kunnen we in de toekomst nog wat projectjes starten...? Verder wil ik Sandra H. en Gerben bedanken voor hun bijdrage aan de projecten die helaas dit proefschrift niet gehaald hebben... Daarnaast wil ik alle overige medewerkers bedanken voor alle hulp, en natuurlijk ook voor alles dat buiten werktijd plaats vond, zoals mountainbiken, klimmen, zeilen, filmavonden, laven en munten, enz.

Dan mijn paranimfen, Ard de Zeeuw en Annemarie Eek. Ard, al >20 jaar goede vrienden, bedankt daarvoor! Annemarie, dank voor het organiseren van menig nucmed-evenement, en vele uitnodigingen voor eten e.d., en natuurlijk dat je paranimf bent. Als laatste wil ik mijn ouders en zussen bedanken. Niet altijd was voor iedereen even duidelijk waar ik mee bezig was, maar toch werd ik bijgestaan met steun en raad. Daarbij wil ik speciaal mijn vader, Hans Disselhorst, bedanken, die onmisbaar was bij deze promotie.